Thermal convection experiments in liquid metal flows with and without magnetic field

Dissertation

zur Erlangung des akademischen Grades

Doktoringenieur

(Dr.-Ing.)

vorgelegt der

Fakultät für Maschinenbau der

Technischen Universität Ilmenau

von Herrn

M.Sc. Till Zürner

geboren am 1. Oktober 1990 in Dresden, Deutschland

Abstract

The interaction of electrically conducting fluid flows with magnetic fields appears in numerous natural phenomena and technical applications. Since the relevant fluids – such as liquid metals and plasmas – are generally very hot, the flows are often accompanied or even driven by thermal convection. The study of this so-called magnetoconvection is thus of interest for a number of physical systems. Two aspects are investigated in this thesis. The first concerns the case when an imposed magnetic field does not alter the fluid flow. The second case explores the changes of the flow structure and global transport properties in the presence of strong magnetic fields.

The first point is relevant for inductive measurement techniques, which are required to probe the flow without disturbing it. Here, the size of the fluid volume affected by a localised magnetic field is of major importance. This topic is investigated theoretically by deriving an algorithm to calculate the penetration depth of the magnetic field into the medium. This allows the prediction of a magnetic field strength, above which a flow is significantly disturbed. The theoretical results are verified for the measurement method of local Lorentz force velocimetry which is applied to a vertical convection flow.

The second point is investigated experimentally for a Rayleigh-Bénard convection system that is subject to a homogeneous vertical magnetic field. The set-up consists of a cylindrical cell of aspect ratio one. The large-scale flow structure is monitored using temperature measurements and ultrasound Doppler velocimetry. The evolution of the flow with increasing magnetic field strength is classified into different regimes and compared with theoretical predictions, and numerical simulations. Global transport properties of the flow concerning its momentum, and the heat passing through the fluid are analysed and their behaviour is interpreted in light of the aforementioned flow regimes.

Additionally, a new theoretical model is developed to predict the turbulent heat and momentum transfer in the fluid by extending the Grossmann-Lohse theory for the classical Rayleigh-Bénard convection setting by the effects of a vertical magnetic field. Experimental data of the present study and from literature are used to verify and enhance the model, and to identify relevant physical mechanisms responsible for the observed results.

Zusammenfassung

Die Wechselwirkung zwischen elektrisch leitfähigen Fluiden und Magnetfeldern tritt in zahlreichen natürlichen Phänomenen und technischen Anwendungen auf. Weil die dabei relevanten Medien – meist Flüssigmetalle oder Plasmen – im Allgemeinen sehr heiß sind, werden die Strömungen meist von thermischer Konvektion begleitet oder werden sogar von dieser getrieben. Das Phänomen der sogenannten Magnetokonvektion ist damit von Interesse für eine große Anzahl physikalischer Systeme. Die vorliegende Arbeit untersucht hierbei zwei Aspekte. Zum einen wird der Fall betrachtet, wenn ein aufgeprägtes Magnetfeld das Strömungsfeld nicht verändert. Zum anderen werden die Modifizierungen von Strömungsstruktur und globalen Transporteigenschaften durch starke Magnetfelder untersucht.

Der erste Fall ist wichtig für induktive Messtechniken, welche die Bewegung eines Mediums untersuchen müssen, ohne dieses dabei zu stören. Die Größe des Fluidvolumens, welches von einem örtlich begrenzten Magnetfeld beeinflusst wird, ist hier ein äußerst wichtiger Faktor. Dieses Thema wird untersucht, indem die Eindringtiefe des Magnetfeldes in das Medium theoretisch hergeleitet wird. Das erlaubt die Vorhersage einer Magnetfeldstärke, oberhalb derer eine Strömung maßgeblich gestört wird. Die theoretischen Ergebnisse werden mittels experimenteller Messungen überprüft. Dazu wird die Messmethode der lokalen Lorentzkraft-Anemometrie auf eine vertikale Konvektionsströmung angewandt.

Für den zweiten Fall wird das System der Rayleigh-Bénard Konvektion unter einem homogenen, vertikalen Magnetfeld experimentell untersucht. Der Aufbau besteht aus einer zylindrischen Zelle mit einem Aspektverhältnis von eins. Die großskalige Struktur der Strömung wird mittels Temperaturmessungen und Ultraschall Doppler Anemometrie überwacht. Die Entwicklung der Strömung mit ansteigender Magnetfeldstärke kann in verschiedene Regime kategorisiert und mit theoretischen Vorhersagen sowie numerischen Simulationen verglichen werden. Globale Transporteigenschaften des Systems bezüglich Impuls und übertragener Wärme werden analysiert und ihr Verhalten anhand der zuvor gefundenen Strömungsregime interpretiert.

Zusätzlich wird ein theoretisches Modell entwickelt um den turbulenten Wärme- und Impulstransport vorherzusagen. Dazu wird die Großmann-Lohse Theorie für klassische Rayleigh-Bénard Konvektion durch den Effekt eines vertikalen Magnetfeldes erweitert. Die experimentellen Daten aus der vorliegenden Arbeit und aus der Literatur werden genutzt, um dieses Modell zu verifizieren und zu optimieren. Dabei werden physikalische Prozesse identifiziert, welche maßgeblich zu den beobachteten Ergebnissen beitragen.

Contents

Contents

Nomenclature

Latin characters

Symbol	Unit	Description
A	m^2	Horizontal cell cross-section
a	–	Blasius boundary layer parameter
$\boldsymbol{B}$	T	Magnetic flux density
$\boldsymbol{b}$	T	Induced magnetic flux density
c	m s^{-1}	Speed of sound
c_p	J kg^{-1} K^{-1}	Isobaric heat capacity
D	m	Cell diameter
d	m	Penetration depth of a local Lorentz force velocimeter
$\boldsymbol{E}$	V m^{-1}	Electric field
$\boldsymbol{e}_x, \boldsymbol{e}_y, \boldsymbol{e}_z$	–	Cartesian unit basis vectors
$\boldsymbol{F}$	N	Force
$\boldsymbol{f}$	N m^{-3}	Force density
f	s^{-1}	Frequency
G	–	Green's function
$\boldsymbol{g}$	m s^{-2}	Gravitational acceleration
H	m	Cell height
Ha	–	Hartmann number
Ha$_{\mathrm{c}}$	–	Onset of convection in an infinite fluid layer
Ha$_{\mathrm{Ch}}$	–	Chandrasekhar limit
Ha$_{\mathrm{H}}$	–	Onset of convection in a cylindrical cell of aspect ratio 1
h	m	Vertical position of a permanent magnet above a fluid surface
$\boldsymbol{j}$	A m^{-2}	Electric current density
k	m^{-1}	Wavenumber
L	m	Width of a fluid layer
l	m	Half side length of a cubic permanent magnet
l_{m}	m	Characteristic scale of a magnetic field
$\boldsymbol{M}$	A m^{-1}	Magnetisation
m	kg	Mass
N	–	Interaction parameter
Nu	–	Nusselt number
$\boldsymbol{n}$	–	Unit normal vector on a surface
$\tilde{P}$	–	Relative contribution of a velocity field to the total Lorentz force
Pm	–	Magnetic Prandtl number

Symbol	Unit	Description
Pr	–	Prandtl number
p	$\mathrm{N\,m^{-2}}$	Pressure
Q	–	Chandrasekhar number
$\dot{Q}$	W	Heat flux
R	m	Cell radius
Ra	–	Rayleigh number
$\mathrm{Ra_c}$	–	Onset of convection in an infinite fluid layer
$\mathrm{Ra_{Ch}}$	–	Chandrasekhar limit
$\mathrm{Ra_H}$	–	Onset of convection in a cylindrical cell of aspect ratio 1
Re	–	Reynolds number
Rm	–	Magnetic Reynolds number
$\boldsymbol{r}$	m	Spatial vector
r	m	Radial coordinate
S	$\mathrm{m^2}$	Surface
$\boldsymbol{s}$	m	Spatial vector on a surface
T	$^\circ\mathrm{C}$	Temperature
$\bar{T}$	$^\circ\mathrm{C}$	Average fluid temperature
$\tilde{T}$	–	Normalised temperature
$\mathcal{T}$	–	Pseudo-temperature profile (normalised)
t	s	Time
U	$\mathrm{m\,s^{-1}}$	Characteristic velocity
V	$\mathrm{m^3}$	Volume
$\boldsymbol{v}$	$\mathrm{m\,s^{-1}}$	Velocity
$\boldsymbol{w}$	$\mathrm{N\,s\,m^{-4}}$	Sensitivity function
$\tilde{\boldsymbol{w}}$	$\mathrm{N\,s\,m^{-2}}$	Integrated sensitivity function
x, y, z	m	Cartesian coordinates

Greek characters

Symbol	Unit	Description
α	$\mathrm{K^{-1}}$	Volumetric thermal expansion coefficient
β	–	Reynolds number scaling factor
Γ	–	Aspect ratio
γ	–	Power law exponent
ΔT	K	Cell temperature difference
Δt	s	Correlation time shift
δ	–	Dirac delta distribution
δ_{mn}	–	Kronecker delta for indices m and n
$\delta_v, \delta_T, \delta_B$	m	Viscous / thermal / Hartmann boundary layer thickness
$\epsilon_\kappa, \varepsilon_\kappa$	$\mathrm{K^2\,s^{-1}}$	Local / mean thermal dissipation rate
$\epsilon_\nu, \varepsilon_\nu$	$\mathrm{m^2\,s^{-3}}$	Local / mean kinetic dissipation rate

Symbol	Unit	Description
$\epsilon_\sigma, \varepsilon_\sigma$	$\mathrm{T^2\,s^{-1}}$	Local / mean magnetic dissipation rate
ε_{jkl}	–	Levi-Civita symbol for indices j, k, and l
η	$\mathrm{m^2\,s^{-1}}$	Magnetic diffusivity
θ	°	Flow orientation
κ	$\mathrm{m^2\,s^{-1}}$	Thermal diffusivity
λ	$\mathrm{W\,m^{-1}\,K^{-1}}$	Thermal conductivity
μ	$\mathrm{N\,A^{-2}}$	Magnetic permeability
ν	$\mathrm{m^2\,s^{-1}}$	Kinematic viscosity
ξ	m	Horizontal coordinate parallel to the LSC orientation
π	–	Archimedes' constant, $\pi \approx 3.14159$
ρ	$\mathrm{kg\,m^{-3}}$	Mass density
σ	$\mathrm{S\,m^{-1}}$	Electrical conductivity
τ	s	Time scale
ϕ	°	Azimuthal coordinate
φ	V	Electric scalar potential

Abbreviations

Acronym	Meaning
BL	Boundary layer
CIFT	Contactless inductive flow tomography
DC	Direct current
DR	Dissipation rate
GL	Grossmann-Lohse (theory)
HZDR	Helmholtz-Zentrum Dresden – Rossendorf
IOFS	Interference optical force sensor
LDV	Laser Doppler velocimetry
LFV	Lorentz force velocimetry or velocimeter
LLFV	Local Lorentz force velocimetry or velocimeter
MHD	Magnetohydrodynamics
MULTIMAG	MULTIpurpose MAGnetic system
ODR	Orthogonal distance regression
PDF	Probability density function
PID	Proportional-integral-derivative (controller)
PIV	Particle image velocimetry
PTV	Particle tracking velocimetry
RBC	Rayleigh-Bénard convection
rms	root-mean-square (average)
TC	Thermocouples
UDV	Ultrasound Doppler velocimetry
UVP	Ultrasound velocity profiling

Nomenclature

Acronym	Meaning
VC	Vertical convection

1. Introduction

1.1. Motivation

Thermal convection is an important and ubiquitous mechanism of heat transport. Potentially turbulent flows in liquids and gases driven by buoyancy forces due to temperature inhomogeneities transfer heat much more effectively than pure heat conduction. As such, it appears in many natural processes and is exploited by numerous technical applications.

In nature, it drives flows in the Earth's atmosphere, generating local and global weather phenomena. It contributes to the interconnected currents throughout the world's oceans and is part of the continental drift. In the hot cores of planets and stars it creates flows which are responsible for the planetary and stellar magnetic fields. On smaller scales, it can be seen as air rising from fire or hot surfaces, or as movement of water being heated on a stove.

Technical applications of thermal convection include cooling of equipment which can be very cost effective since it is self-sustained and requires no additional devices such as fans. Air conditioning of rooms and buildings also has to take warm rising air into account. An equally important engineering task is the prevention of convective flows for heat insulation, e.g. in double- or triple-paned windows. In metallurgy, convective flows significantly influence the solidification process of metals and need to be monitored and controlled. Lately, liquid metals are considered as a potential heat transport medium for fusion reactors, where the input of heat by neutron radiation causes convective flows.

The examples of metallurgy, fusion reactors and the flow in planet cores or stars were given, since they share an additional property: Their flows are influenced by magnetic fields. These have their origin in electromagnetic brakes or stirrers for metallurgy, in superconducting coils confining the plasma of fusion reactors and in the dynamo effect, which sustains a self-excited magnetic field from the motion in a planet's liquid metal core or a star's plasma. All these systems display complex dynamics and interactions which are challenging to understand. Progress in uncovering the physics and mechanisms behind these phenomena can nonetheless be achieved by studying simplified models. These generally cover a selected subset of aspects from the full system, concentrating on certain influences only. The present thesis specifically considers the problem of a horizontal fluid layer heated from below, cooled from above and subjected to a vertical magnetic field. This system will be introduced in the following sections 1.2 and 1.3.

A major part of the work presented in this thesis is of experimental nature. For a magnetic field to significantly influence a fluid, the selected medium has to be electrically conducting. In the above examples, liquid metals and plasmas all have a very good electrical conductivity. For laboratory experiments, only the use of liquid metals is feasible. They, however, provide a different challenge. Many flow measurement techniques rely on an optical access to the interior of the fluid, i.e. it needs to be transparent. This is not the case for liquid metals, which are opaque for most forms of radiation. To acquire access to the flow field in the fluid interior,

other measurement methods have to be employed, which are outlined in section 1.4. While restricted by the opaqueness of liquid metals, a number of measurement techniques exploit a different property: the high electrical conductivity. Among the so-called inductive measurement methods, Lorentz force velocimetry is a recently developed technique, which has not been used in thermal convection flows yet. A successful application of this method may provide another option for the limited arsenal of measurement techniques in liquid metal thermal convection. The method will be introduced in section 1.4.1 and the examination of its applicability in thermal convection flows will be another central topic of this work.

The aspects investigated by the present study are thus twofold. Firstly, an extension of the range of applicability of Lorentz force velocimetry is investigated. Secondly, the influence of a vertical magnetic field on thermal convection in liquid metals is examined. The following sections of this chapter will introduce the state of the art knowledge for both topics and outline open problems that are still unsolved. The scientific objectives of this thesis are then outlined at the end of this chapter in section 1.5.

1.2. Thermal convection

The general meaning of convection in fluid mechanics is the transport in a fluid. This covers a wide variety of topics reaching from substances dispersed in liquids, intrinsic properties of the fluid (e.g. temperature) to distortion of magnetic fields by plasma flows. For most cases, this transport can be divided into two mechanisms: diffusion and advection.

The diffusive transport is caused by the random microscopic motion of fluid molecules. It occurs whenever the considered quantity Φ varies spatially and reduces these inhomogeneities until homogeneity is reached. Since the microscopic aspects of a fluid are not considered in the continuum formulation of fluid mechanics, diffusion is characterised by a material constant: According to Fick's first law, the quantity flux $\boldsymbol{F}$ is proportional to the negative gradient of the quantity $\boldsymbol{F} = -D\boldsymbol{\nabla}\Phi$ [1]. The corresponding proportionality constant is called the diffusion constant D, which is specific to the transporting fluid and the transported quantity Φ. It always carries a physical dimension of $\mathrm{m}^2\,\mathrm{s}^{-1}$.

Advection describes the transport by the macroscopic, directed flow of the fluid. It is thus highly dependent on the type of flow in consideration. A broad distinction can be made by the cause of the flow. The first case is called forced convection. It is characterised by an externally applied force, which drives the flow. This includes pumps or propellers, which induce movement via surface forces. External volume forces, such as Lorentz forces in an electromagnetic pump, also belong in this category. The opposing case is called natural or free convection. Here, the cause of fluid movement are internal forces, which are generated by the properties of the fluid itself. Examples are interface forces caused by varying surface tension, or buoyancy forces generated by spatial inhomogeneities in the mass density. The latter, called buoyant convection, requires the presence of a gravitational field. The density differences within the fluid can have a variety of causes, most prominent of which are varying concentrations of diluted substances (solutal convection) or temperature gradients (thermal convection). The latter is of interest in the present work.One major difference between forced and natural convection is the flow speed. For most technical applications, forced convection is one or two orders of magnitude faster than in
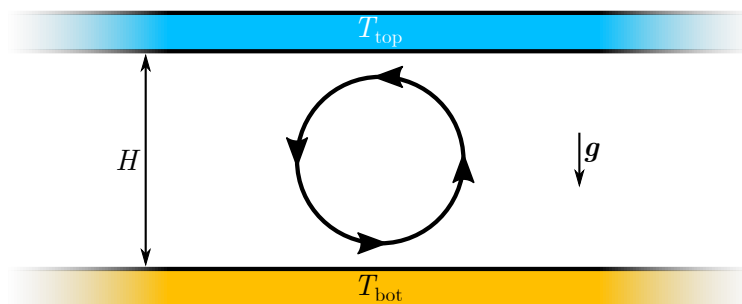
Figure 1.1.: Illustration of a Rayleigh-Bénard convection system, consisting of a horizontal fluid layer of height H with constant top and bottom temperatures, T_{top} and T_{bot}, respectively. The acceleration due to gravity $\boldsymbol{g}$ is parallel to the imposed temperature gradient.

comparable natural convection systems. If only one type on convective system is considered, it is common practice to simply name it "convection". In the present study, the term "convection" generally refers to thermal convection, if not specified otherwise.

An additional transport mechanism in thermal convection is heat radiation. Every object emits heat in form of electromagnetic waves based on its temperature. Whether this effect is relevant for thermal convection depends on the permeability of the fluid for thermal radiation. At low temperatures around room temperature, the radiative heat transport can often be neglected when compared to heat diffusion and advection. Additionally, liquid metals are notoriously hard to penetrate by electromagnetic radiation. The effect of radiation will thus not be considered in the present work.

The first thorough experimental investigation of thermal convection was published by Henri Bénard in 1900 [2]. He described the behaviour of a thin fluid layer heated from below and with a free upper surface. A movement of the fluid was only detectable, once a critical temperature difference was exceeded, called the onset of convection. The resulting flow structures were hexagonal cells with up-welling flow in their centre and down-welling flow at the boundaries between cells. It has been shown, that the flow observed in Bénard's experiments was caused by forces due to inhomogeneous surface tension (called Marangoni convection), rather than buoyancy forces [3]. This was caused by the free surface and the very small thickness of the fluid layer in the order of millimetres. However, the publications of Bénard sparked a number of investigations on the topic by different scientists. The first theoretical explanation was put forth by Lord Rayleigh in 1916 [4]. He calculated the critical temperature difference and structure size for the onset of convective flow in an infinite fluid layer bounded by two horizontal free surfaces, with heating from below and cooling from above. This specific system, depicted in figure 1.1, has been named Rayleigh-Bénard convection (RBC) in honour of these two scientists.

Rayleigh's treatment of the system created the basis for all following theoretical investigations of the topic and is still used today. His formulation of the equations describing thermal convection utilizes the Boussinesq approximation. In general, all material properties of the fluid depend on the temperature T. In the Boussinesq approximation these changes due to temperature variations are neglected, except for the change of mass density ρ in the buoyancy force. Here, the density

is approximated by a linear function of the temperature: $\rho(T) = \rho_0 - \rho_0\alpha(T - T_0)$, where $\rho_0 = \rho(T_0)$ is the density at a reference temperature T_0 and $\alpha = -(1/\rho_0)\partial\rho/\partial T|_p$ is the volumetric thermal expansion coefficient at constant pressure p. In all other aspects, the fluid is considered to be incompressible and the density $\rho = \rho_0$ is constant. These assumptions result in the equations [5]

$$\boldsymbol{\nabla} \cdot \boldsymbol{v} = 0\,, \tag{1.1a}$$

$$\frac{\partial \boldsymbol{v}}{\partial t} + (\boldsymbol{v} \cdot \boldsymbol{\nabla})\boldsymbol{v} = -\frac{1}{\rho_0}\boldsymbol{\nabla}p + \nu\boldsymbol{\nabla}^2\boldsymbol{v} + \boldsymbol{g}\alpha(T - T_0)\,, \tag{1.1b}$$

$$\frac{\partial T}{\partial t} + (\boldsymbol{v} \cdot \boldsymbol{\nabla})T = \kappa\boldsymbol{\nabla}^2 T\,. \tag{1.1c}$$

The velocity $\boldsymbol{v} \equiv \boldsymbol{v}(\boldsymbol{r}, t)$, temperature $T \equiv T(\boldsymbol{r}, t)$, and pressure $p \equiv p(\boldsymbol{r}, t)$ are fields, which can be determined for a given geometry and boundary conditions (BC). Here, p specifically refers to the pressure deviation from the hydrostatic equilibrium in the case $\boldsymbol{v}(\boldsymbol{r}, t) = \boldsymbol{0}$ in the whole fluid. ν is the kinematic viscosity and κ the thermal diffusivity of the fluid. $\boldsymbol{g}$ denotes the acceleration due to gravity, specifying its direction and magnitude g.

Boundary conditions have to be imposed on the temperature and velocity field. In Rayleigh-Bénard convection, the lower and upper boundary are kept at constant temperatures T_{bot} and T_{top}, respectively. For an unstable density stratification to be possible it is required that $T_{\mathrm{bot}} > T_{\mathrm{top}}$. An alternative BC is a prescribed constant heat flux at the top and bottom boundaries $\partial T/\partial z = \mathrm{const}$. For the velocity field the type of boundary is important. A free surface requires the conditions $v_z = 0$ and $\partial v_x/\partial x = \partial v_y/\partial y = 0$ to hold, whereas a rigid wall implies a no-slip condition with $\boldsymbol{v} = \boldsymbol{0}$. The former BC was used by Rayleigh at both boundaries, which allowed an analytical solution of the problem by expanding the quantities in a series of normal modes.

A dimensional analysis of the equations (1.1a) to (1.1c) reveals, that the problem is depends two dimensionless parameters only: the Rayleigh number Ra and the Prandtl number Pr

$$\mathrm{Ra} = \frac{g\alpha\Delta T H^3}{\nu\kappa}\,, \tag{1.2}$$

$$\mathrm{Pr} = \frac{\nu}{\kappa}\,. \tag{1.3}$$

The height H of the fluid layer is used as a characteristic length scale, and the temperature difference $\Delta T = T_{\mathrm{bot}} - T_{\mathrm{top}}$ as a characteristic temperature scale. The Rayleigh number characterises the ratio of the driving buoyancy forces with respect to the damping effects of viscosity and thermal diffusion. The Prandtl number is a material parameter of the fluid, i.e. the ratio of viscous and thermal diffusivities. A characteristic velocity of thermal convection is the free-fall velocity $U_{\mathrm{ff}} = \sqrt{g\alpha\Delta T H}$. It represents the speed a fluid element with a temperature difference ΔT relative to its surrounding reaches after a distance H, if viscosity and thermal diffusion are neglected. The corresponding time scale is the free-fall time

$$\tau_{\mathrm{ff}} = \frac{H}{U_{\mathrm{ff}}} = \sqrt{\frac{H}{g\alpha\Delta T}}\,. \tag{1.4}$$

While Rayleigh did not use the parameters Ra and Pr himself, his calculations revealed that the onset of thermal convection is independent of Pr and occurs at a critical Rayleigh number
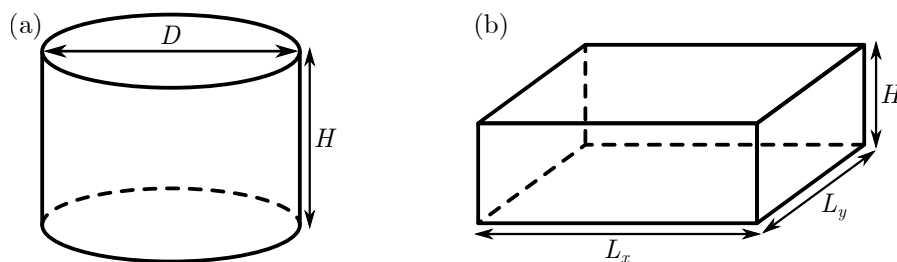
Figure 1.2.: Common RBC cell geometries. (a) Cylindrical cell with height H and diameter D. (b) Rectangular cell with height H, width L_x and depth L_y.

$Ra_c = 27\pi^4/4 \approx 657.5$. This value only holds for two free surfaces of the fluid layer, which is not a realistic condition. The more relevant cases of a lower rigid and upper free surface as well as rigid boundaries at both top and bottom were investigated in 1926 by Jeffreys [6] and by Pellew and Southwell [7] in 1940. In the rigid-free case the critical Rayleigh number becomes $Ra_c = 1100.65$ and for the rigid-rigid case it is $Ra_c = 1707.8$ [7].

These values for the onset of static convection are independent of the Prandtl number, but can be modified if the effect of lateral side walls is introduced. This is especially relevant for experimental studies, since the idealised system of an infinite fluid layer is not feasible in reality. The geometry of a convection system is generally described by the proportion of the lateral extent to the height of the fluid layer, the so-called aspect ratio Γ. In cylindrical cells (figure 1.2(a)) it is given by

$$\Gamma = \frac{D}{H} \tag{1.5}$$

with the diameter D of the cell. Thus, the aspect ratio is a non-dimensionalised lateral size of the considered system. Alternatively, the cell radius $R = D/2$ or the inverse of (1.5) can be used to define Γ instead. For rectangular box-geometries (figure 1.2(b)), two aspect ratios have to be defined for the two independent lateral extends, often denoted by Γ_x and Γ_y (if z is the vertical axis). Alternatively, the geometry is characterised as *width* : *depth* : *height* $= \Gamma_x : \Gamma_y : 1$.

Rigid side walls are known to generally stabilise a flow because they impose no-slip boundary conditions which brake the flow. They have the same effect on the onset of RBC. For large aspect ratios $\Gamma \gg 1$, most of the fluid is far away from the side walls and acts as if in a infinitely extended layer (i.e. $\Gamma \to \infty$). For small aspect ratios $\Gamma \lesssim 10$ to 15 the critical Rayleigh number starts to increase due to the influence of the side walls on the whole fluid layer [8–10]. For a $\Gamma = 1$ cylindrical cell the critical Rayleigh number has increased to $Ra_c \sim 10^4$ [10] and is diverging towards infinity for $\Gamma \to 0$.

The flow at Rayleigh numbers slightly above the onset is generally dominated by convection rolls (figure 1.3(a)). Their shape, orientation and size is also influenced by the geometry for $\Gamma \lesssim 30$ [11]. Alternatively, deviations from the ideal case of the Boussinesq approximation such as significant temperature dependencies of fluid properties can lead to hexagonal cells near the onset (figure 1.3(b)). These initial patterns are quickly superseded by other patterns and instabilities. The rich variety of instabilities in this weakly non-linear regime were studied intensively in the 1960s and 1970s. A comprehensive diagram of the stability boundaries of
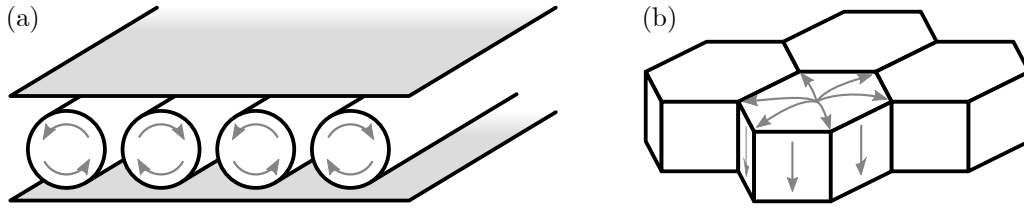
Figure 1.3.: Illustration of flow patterns near the onset of convection. (a) Counter-rotating rolls between two solid plates. (b) Hexagonal cells with rising fluid in their centre. This configuration has a free surface and is thus additionally influenced by surface tension. A down-welling flow in the centre is possible as well.

convection rolls over the $(\mathrm{Ra}, \mathrm{Pr}, k)$ phase space was created by Busse and Clever [12] and was later termed the Busse-balloon [11]. Here, the variable k is the horizontal wavenumber of the convection rolls, describing their lateral size.

These studies describe the transition from laminar convection close to the critical Rayleigh number via time-dependent flows in the weakly non-linear regime to strongly turbulent convection. There, the bulk flow of the fluid is dominated by the inertia of the fluid and is subject to large velocity fluctuations [13, 14]. While turbulence is generally associated with an erratic flow, thermal convection still displays, on average, well ordered structures which are the topic of recent investigations and are termed turbulent superstructures [15–17]. For a $\Gamma = 1$ cell, the flow organises into a single convection roll [13, 14]. Contrary to this seemingly simplistic structure, it displays a variety of dynamic effects which will be investigated in depth in this thesis (see chapter 4).

1.2.1. Predicting heat & momentum transfer

Two of the central questions in thermal convection research are those on the amount of heat transported across the fluid layer and the flow speed, i.e. the momentum transport in the fluid. For a given system finding these quantities would normally involve time-consuming experiments or numerical simulations. Consequently, the development of simplified models which quickly predict the expected properties of a thermal convection system has been of major interest for researchers. Such models can be used for example by engineers in the technical design of machines. A successful model also sheds light on the relevant mechanisms within the fluid which contribute to the transport of heat and momentum, and can further the scientific understanding of thermal convection.

In Rayleigh-Bénard convection, a certain amount of heat per unit time enters the fluid from the bottom, is transported upwards and leaves the system at the top. The heat flux density can vary spatially, but if integrated over any horizontal cross-section at a vertical position z, the resulting total heat flux $\dot{Q}(z)$ is constant for all z. The heat flux $\dot{Q}$ can be divided into two parts. The first is caused by heat diffusion and the second by advection of heat in the flow. The purely diffusive heat flux $\dot{Q}_{\mathrm{diff}}$ in absence of any fluid motion can be calculated by

$$\dot{Q}_{\mathrm{diff}} = \lambda A \frac{\Delta T}{H} \,. \tag{1.6}$$

λ is the thermal conductivity of the fluid and A is the area of the horizontal cross-section. To characterize the heat transport in thermal convection, the Nusselt number Nu is defined as the total heat flux $\dot{Q}$, normalized by the purely diffusive heat flux $\dot{Q}_{\mathrm{diff}}$

$$\mathrm{Nu} = \frac{\dot{Q}}{\dot{Q}_{\mathrm{diff}}}. \tag{1.7}$$

In absence of fluid motion the total heat flux is equal to the diffusive heat flux $\dot{Q} = \dot{Q}_{\mathrm{diff}}$ and thus $\mathrm{Nu} = 1$. Once convective motion starts, the heat transport is enhanced and the Nusselt number increases. Two additional equations to calculate Nu can be derived from the Boussinesq equations (1.1) [14, 18]

$$\mathrm{Nu} = \frac{\langle v_z T \rangle_{A,t} - \kappa \frac{\partial \langle T \rangle_{A,t}}{\partial z}}{\kappa \Delta T / H} \tag{1.8}$$

$$= 1 + \frac{\langle v_z T \rangle_{V,t}}{\kappa \Delta T / H}. \tag{1.9}$$

These definitions are used in theoretical calculations and numerical simulations. The expressions $\langle \cdot \rangle_{A,t}$ and $\langle \cdot \rangle_{V,t}$ are averages over the horizontal cross-section and time, and the whole fluid volume and time, respectively. The three definitions (1.7), (1.8) and (1.9) are equivalent.

The transport of momentum is characterized by the Reynolds number Re. It gives the ratio of inertial and viscous forces within the fluid and is defined by

$$\mathrm{Re} = \frac{UH}{\nu}. \tag{1.10}$$

U is a characteristic velocity of the flow in question. In the absence of a prescribed flow, i.e. no forced convection, this most often is an average or root-mean-square (rms) average of the velocity field $\boldsymbol{v}(\boldsymbol{r}, t)$. Simulations commonly calculate the rms-average of the velocity magnitude $|\boldsymbol{v}|$ over the whole fluid volume V and time t

$$U = \langle |\boldsymbol{v}(\boldsymbol{r}, t)| \rangle_{\mathrm{rms},V,t} \equiv \sqrt{\langle |\boldsymbol{v}(\boldsymbol{r}, t)|^2 \rangle_{V,t}} \tag{1.11}$$

The Reynolds number is meant to capture the general intensity of the flow, but neglects specifics about the flow structure.

For RBC these dimensionless quantities, Nu and Re, depend on the control parameters Rayleigh number Ra, Prandtl number Pr and aspect ratio Γ of the system. The goal is to find general expressions $\mathrm{Nu} = \mathrm{Nu}(\mathrm{Ra}, \mathrm{Pr}, \Gamma)$ and $\mathrm{Re} = \mathrm{Re}(\mathrm{Ra}, \mathrm{Pr}, \Gamma)$. Until numerical simulations became viable in the last quarter of the 20th century, experimental data were used to verify theoretical results for these dependencies. Since a change of the parameters Pr and Γ is accompanied by significant experimental difficulties, because they require replacement of working fluids or the convection cell, the historically most studied dependency of Nu and Re is their change with Ra.

Early results suggested, that the relation Nu(Ra) follows a power law $\mathrm{Nu} \propto \mathrm{Ra}^\gamma$ for wide ranges of Ra [19]. However, the exact reported values for the exponent γ vary considerably, mostly within the range $1/4 < \gamma < 1/3$. The first theoretical model for the scaling exponent
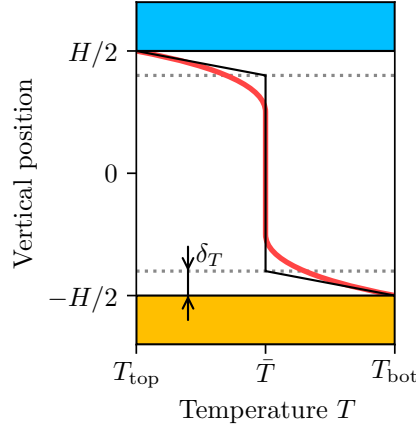
Figure 1.4.: Illustration of the average vertical temperature profile (red line) in turbulent Rayleigh-Bénard convection. The profile is well approximated by a piecewise linear function (black line) with a temperature drop of $\Delta T/2$ across each of the two thermal boundary layers with a thickness δ_T and a perfectly mixed fluid bulk with constant temperature $\bar{T}$.

is based on the bottleneck of the heat transport: the thermal boundary layer (BL). All heat has to pass through the diffusion dominated layer close to the top and bottom walls. Here, advection does not enhance the heat transport due to rigid BC and pure heat conduction imposes an upper limit on the heat flux. Malkus published a theory in 1954 [20], which assumed that the edge of the thermal BL is always marginally stable and found an exponent of $\gamma = 1/3$. This means, a Rayleigh number based on the thermal BL Ra_T is always of the order of the critical Rayleigh number $\mathrm{Ra_c}$. The temperature profile is approximated by a piecewise linear function (see figure 1.4). Half of the temperature difference ΔT occurs across the thickness δ_T of the BL. Outside the BL, the fluid is well mixed by the bulk flow and the temperature is constant. This model gives an approximation of δ_T as [14]

$$\delta_T \simeq \frac{H}{2\mathrm{Nu}} \, . \tag{1.12}$$

$\mathrm{Ra}_T = (\delta_T/H)^3 \mathrm{Ra}/2$ is then calculated with δ_T as its length scale and with $\Delta T/2$ for the temperature drop in the BL. With $\mathrm{Ra}_T \sim \mathrm{Ra_c}$, a scaling of $\mathrm{Nu} \propto \mathrm{Ra}^{1/3}$ follows. This result approximately matches some of the experimental results of the time, but does not explain exponents closer to 1/4, or variations of γ with different working fluids, i.e. with changing Prandtl number [19].

Other theoretical approaches use specific assumptions about the flow. Shraiman and Siggia [21] found scaling laws for Nu and Re when a large-scale wind at the plates is strong enough to create a turbulent boundary layer. They obtain $\gamma = 2/7 \approx 0.286$. Kraichnan [22] derived scaling laws with logarithmic corrections that apply for very large Rayleigh numbers, the ultimate regime of thermal convection. The resulting effective values of γ exceed $1/3$. For very low Prandtl numbers when convective turbulence is dominated by inertia, Busse and Clever [23] predicted an exponent of $\gamma = 1/4$ within an asymptotic model.

Instead of finding pure scaling laws for specific regimes, Grossmann and Lohse [24] developed a theory covering a large range of Ra and Pr with different scaling characteristics. Since this theory will be used as a basis for the theoretical considerations of the present thesis, it is discussed in detail in the following section.

1.2.2. The Grossmann-Lohse theory

Grossmann and Lohse developed a new scaling theory in the early 2000s. Their first publication in 2000 [24] considered the viscous and thermal dissipation rates (DR) in a convective flow. By dividing those into the contributions of characteristic sections of the fluid, namely the bulk and the boundary layers, they were able to give approximative scaling relations. This resulted in pure scaling laws for four different regimes that differ by which of the DR contributions is dominant. In [25], the separate scaling laws were merged into one unified model. This so-called Grossmann-Lohse theory (GL theory) predicts Nusselt and Reynolds numbers over a large range of Rayleigh and Prandtl numbers. Rather than resulting in pure power laws, the GL theory gives a continuous transition between regimes with different scaling behaviours. A central point is, that the model contains five free parameters, which have to be fitted to experimental data. The latest update of the theory in 2013 [26] only used the minimum number of 5 data points to determine the free model parameters and achieved good agreement with most known sets of experimental data, even when extrapolating far from the fitting data. In the following, the basic derivation and arguments of the GL theory are summarised, as given in [24–27].

In a convective flow, energy is dissipated by the viscosity of the fluid and by heat diffusion. The viscous and thermal energy dissipation rates (DR) ϵ_ν and ϵ_κ, respectively, are defined as

$$\epsilon_\nu(\boldsymbol{r}, t) = \frac{\nu}{2} \left(\partial_i u_j + \partial_j u_i \right)^2 , \tag{1.13a}$$

$$\epsilon_\kappa(\boldsymbol{r}, t) = \kappa \left(\partial_i T \right)^2 . \tag{1.13b}$$

The Einstein summation convention applies with $i, j = x, y, z$ and $\partial_i \equiv \partial/\partial x_i$ is the spatial derivative for the i-th coordinate. For the mean dissipation rates – averaged over the whole fluid volume and over time – the following exact relations can be derived in the case of statistically stationary turbulence [28]

$$\varepsilon_\nu \equiv \langle \epsilon_\nu \rangle_{V,t} = \frac{\nu^3}{H^3} \frac{(\mathrm{Nu} - 1)\mathrm{Ra}}{\mathrm{Pr}^2} , \tag{1.14}$$

$$\varepsilon_\kappa \equiv \langle \epsilon_\kappa \rangle_{V,t} = \kappa \frac{(\Delta T)^2}{H^2} \mathrm{Nu} . \tag{1.15}$$

The first step of the GL theory is to separate the mean DR into their contributions from the boundary layer (BL) at the top and bottom surface, and the fluid bulk

$$\varepsilon_\nu = \varepsilon_{\nu,\mathrm{BL}} + \varepsilon_{\nu,\mathrm{Bulk}} , \tag{1.16}$$

$$\varepsilon_\kappa = \kappa \frac{(\Delta T)^2}{H^2} + \varepsilon_{\kappa,\mathrm{BL}} + \varepsilon_{\kappa,\mathrm{Bulk}} . \tag{1.17}$$

The additional term of $\kappa(\Delta T)^2/H^2$ in (1.17) represents the effect of pure thermal diffusion [29]. The contributions $\varepsilon_{\kappa,\mathrm{BL}}$ and $\varepsilon_{\kappa,\mathrm{Bulk}}$ exclusively represent the contribution of fluid motion to the

mean thermal dissipation rate. $\varepsilon_{\kappa,\mathrm{BL}}$ originates from the thermal BL, given by (1.12). On the other hand, $\varepsilon_{\nu,\mathrm{BL}}$ is the contribution of the viscous BL, which, for a laminar BL, is assumed to have a Blasius type flow profile [30]. This implies a BL thickness of

$$\delta_v = a\frac{H}{\sqrt{\mathrm{Re}}} \, . \tag{1.18}$$

The factor a is the first free parameter of the model. It is *a priori* unknown and has to be inferred from measurements of the flow in question.

The separation into two characteristic regions of the flow, enables the approximation of the DR contributions. In the BL, the diffusive transport is assumed to dominate while in the bulk advection is more important. From the DR definitions (1.13) and the Boussinesq equations (1.1) the GL theory estimates the DR contributions to be [25]

$$\varepsilon_{\nu,\mathrm{BL}} \sim \nu\frac{U^2}{\delta_v^2}\frac{\delta_v}{H} \sim \frac{\nu^3}{H^4}\mathrm{Re}^{5/2} \, , \tag{1.19}$$

$$\varepsilon_{\nu,\mathrm{Bulk}} \sim \frac{U^3}{L} \sim \frac{\nu^3}{H^4}\mathrm{Re}^3 \, , \tag{1.20}$$

$$\varepsilon_{\kappa,\mathrm{BL}} \sim \kappa\frac{(\Delta T)^2}{H^2}(\mathrm{PrRe})^{1/2} \, , \tag{1.21}$$

$$\varepsilon_{\kappa,\mathrm{Bulk}} \sim \frac{U(\Delta T)^2}{L} \sim \kappa\frac{(\Delta T)^2}{H^2}\mathrm{PrRe} \, . \tag{1.22}$$

Here, U is the characteristic velocity of the convective wind in the bulk flow. These estimates are also multiplied by the volume fraction of the respective region. For the BL this amounts to a factor of $2\delta_{v,T}/H$, with the constant factor of 2 being omitted. The bulk volume fraction is $(H - 2\delta_{v,T})/H$, which is approximated as ~ 1 for thin BL.

For the estimates of the thermal DR the viscous BL was assumed to be nested within the thermal BL, i.e. $\delta_T > \delta_v$. This implies, that U is the dominant velocity scale for $\varepsilon_{\kappa,\mathrm{Bulk}}$ and $\varepsilon_{\kappa,\mathrm{BL}}$. However, this changes once the thermal BL becomes smaller than the viscous BL. Assuming a linear velocity profile in the viscous BL, the characteristic velocity scale is then $U\delta_T/\delta_v$. To model the crossover between these two regimes, U is replaced by $U f(x_T)$ in (1.21) and (1.22). Here, the transition function $f(x_T) = (1 + x_T^n)^{-1/n}$ is introduced with $n = 4$ and $x_T = \delta_v/\delta_T = 2a\mathrm{Nu}/\sqrt{\mathrm{Re}}$.

A further aspect is that for high Pr the bulk flow becomes laminar due to the strong viscous effects in the fluid. In this case, the viscous BL thickness has a constant value of $\delta_v = H/2$, which is reached in equation (1.18) for a Reynolds number $\mathrm{Re}_H = 4a^2$. This change in scaling is modelled by replacing $\delta_v \to g(x_H)H/2$, using the transition function $g(x_H) = x_H f(x_H)$ with $x_H = \delta_v(\mathrm{Re})/\delta_v(\mathrm{Re}_H) = 2a/\sqrt{\mathrm{Re}}$. This replacement also applies to the argument x_T of the transition above: $x_T \to \mathrm{Nu}\, g(x_H)$.

These additional regime crossovers give the new estimates

$$\varepsilon_{\nu,\mathrm{BL}} \sim \frac{\nu^3}{H^4}\frac{\mathrm{Re}^2}{g\left(2a\mathrm{Re}^{-1/2}\right)} \, , \tag{1.23}$$

$$\varepsilon_{\kappa,\mathrm{BL}} \sim \kappa \frac{(\Delta T)^2}{H^2} \sqrt{\mathrm{PrRe}\, f\Big(\mathrm{Nu}\, g\big(2a\mathrm{Re}^{-1/2}\big)\Big)}\,, \tag{1.24}$$

$$\varepsilon_{\kappa,\mathrm{Bulk}} \sim \kappa \frac{(\Delta T)^2}{H^2} \mathrm{PrRe}\, f\Big(\mathrm{Nu}\, g\big(2a\mathrm{Re}^{-1/2}\big)\Big)\,. \tag{1.25}$$

The approximation of $\varepsilon_{\nu,\mathrm{Bulk}}$ in (1.20) remains unchanged.

In the original article by Grossmann and Lohse [24] pure scaling laws for Nu and Re with Ra and Pr were derived for different regimes. These were distinguished by which of the DR contributions was dominating, and which of the BL thicknesses was larger (the high Pr crossover had not been implemented at the time). This resulted in eight scaling laws for Nu and Re each. However, to calculate the functions $\mathrm{Nu}(\mathrm{Ra}, \mathrm{Pr})$ and $\mathrm{Re}(\mathrm{Ra}, \mathrm{Pr})$ over the whole $(\mathrm{Ra}, \mathrm{Pr})$ space, each estimate was multiplied by a constant prefactor c_i ($i = 1, 2, 3, 4$) and combined with equations (1.14), (1.15), (1.16), and (1.17). This results in a set of two implicit equations for Nu and Re [26]

$$(\mathrm{Nu} - 1)\frac{\mathrm{Ra}}{\mathrm{Pr}^2} = c_1 \frac{\mathrm{Re}^2}{g\big(2a\mathrm{Re}^{-1/2}\big)} + c_2 \mathrm{Re}^3\,, \tag{1.26}$$

$$\mathrm{Nu} - 1 = c_3 \sqrt{\mathrm{PrRe}\, f\Big(\mathrm{Nu}\, g\big(2a\mathrm{Re}^{-1/2}\big)\Big)} + c_4 \mathrm{PrRe}\, f\Big(\mathrm{Nu}\, g\big(2a\mathrm{Re}^{-1/2}\big)\Big)\,. \tag{1.27}$$

These equations display the five free parameters of the model, mentioned above: a, and c_1 to c_4. They are determined by a non-linear fit to measurements of Nu for different values of Ra and Pr. However, the equations are invariant under the transformation $\mathrm{Re} \to \beta\mathrm{Re}$, $a \to \beta^{1/2}a$, $c_1 \to \beta^{-2}c_1$, $c_2 \to \beta^{-3}c_2$, $c_3 \to \beta^{-1/2}c_3$, and $c_4 \to \beta^{-1}c_4$ for any $\beta \in \mathbb{R}$. In order to predict Re correctly as well, at least one measurement Re_β of the Reynolds number has to be known. To calculate the correct model parameters, the procedure is as follows:

1. A set of Nu measurements is used to determine a first set of parameter values by fitting the model equations to the data.
2. These first parameters are used to predict the Reynolds number Re for the values of Ra and Pr, at which the measurement Re_β was taken.
3. The correction factor is calculated as $\beta = \mathrm{Re}_\beta / \mathrm{Re}_p$.
4. The first set of parameter values is now scaled by β using the transformation given above. This results in the correct values of the model parameters.

The rescaling does not affect Nu; it only fixes the correct value of Re. The latest values of the parameters from experiments at $\Gamma = 1$ are [26]: $a = 0.922$, $c_1 = 8.05$, $c_2 = 1.38$, $c_3 = 0.487$, and $c_4 = 0.0252$. The resulting predictions for Nu are in good agreement with experimental data.

1.3. Magnetoconvection

The classical Rayleigh-Bénard convection is often modified by additional effects. Double diffusive convection studies two scalar quantities, that cause buoyancy (e.g. the concentration of a

dispersed material and temperature). Rotating convection places the liquid in a rotating frame of reference. The boundary temperatures can be adjusted so that the fluid experiences a phase transition in the convection cell (e.g. by condensing at the cold plate and evaporating at the hot plate).

An especially interesting case for electrically conducting fluids is the effect of a magnetic field on the flow. The movement of such a fluid through a magnetic field creates Lorentz forces, which may alter the flow structure significantly. In nature, examples of this kind of system are found in geo- and astrophysics. The dynamo effect in planets or stars generates global magnetic fields through a complex interplay of rotating convection flows in the liquid metal core or the plasma, respectively, and said magnetic fields. Future technical applications include the cooling of fusion reactors by liquid metals, which are subjected to the strong magnetic fields used to contain the plasma. The physics of these systems are investigated in the field of magnetohydrodynamics (MHD).

An electrically conducting fluid contains charge carriers that are transported by the flow field $\boldsymbol{v}$. In a static magnetic field $\boldsymbol{B}$ these charges experience a Lorentz force [31]. In MHD, it is generally assumed that the charge relaxation time is much smaller than the timescales of the flow, so that the reaction of the charge distribution on the magnetic field can be considered to be instant. The resulting current density in the fluid is given by Ohm's law for moving conductors

$$\boldsymbol{j}(\boldsymbol{r}) = \sigma\left(\boldsymbol{E}(\boldsymbol{r}) + \boldsymbol{v}(\boldsymbol{r}) \times \boldsymbol{B}(\boldsymbol{r})\right) . \tag{1.28}$$

The crucial material property for the magnitude of the current is the electrical conductivity σ. The electric field $\boldsymbol{E}$ in the fluid is determined by the conservation of charge, which states that

$$\boldsymbol{\nabla} \cdot \boldsymbol{j} = 0 \tag{1.29}$$

inside the fluid volume V. This implies the boundary condition

$$\boldsymbol{n} \cdot \boldsymbol{j} = 0 \tag{1.30}$$

on the volume surface S with the surface normal $\boldsymbol{n}$.

The induced currents in the fluid are called eddy currents. They, once again, interact with the magnetic field. The Lorentz force density $\boldsymbol{f}_{\mathrm{L}}$ acting on a fluid element containing a current density $\boldsymbol{j}$ is

$$\boldsymbol{f}_{\mathrm{L}} = \boldsymbol{j} \times \boldsymbol{B} , \tag{1.31}$$

and has to be included in the Boussinesq equation (1.1b)

$$\frac{\partial \boldsymbol{v}}{\partial t} + (\boldsymbol{v} \cdot \boldsymbol{\nabla})\boldsymbol{v} = -\frac{1}{\rho_0}\boldsymbol{\nabla}p + \nu\boldsymbol{\nabla}^2\boldsymbol{v} - \boldsymbol{g}\alpha(T - T_0) + \frac{1}{\rho_0}\boldsymbol{f}_{\mathrm{L}} . \tag{1.32}$$

Whether the Lorentz force has a significant impact on the flow structure depends on its magnitude compared to the viscous and inertial forces in the fluid. In bulk turbulence, as is the case for most liquid metal flows, inertial and magnetic forces are most relevant. Their ratio is expressed by the interaction parameter

$$\mathrm{N} = \frac{\sigma B^2 l_{\mathrm{m}}}{\rho U} . \tag{1.33}$$

The length scale l_m characterises the penetration depth of the magnetic field into the fluid. If the magnetic field is present within the whole fluid volume, then $l_m \equiv H$. For values $N \ll 1$, the flow is not influenced by the magnetic field. For $N \gtrsim 1$ the flow can be altered by the induced Lorentz forces and is dominated by them for $N \gg 1$. If the magnetic field is not covering the whole fluid volume, the magnetic length scale l_m is not well defined. This topic will be addressed later in section 2.3.

The reverse effect is possible as well: Fast flows can change the magnetic field. In general, the magnetic field $\boldsymbol{B}$ can consist of an applied field $\boldsymbol{B}_0$ and an induced magnetic field $\boldsymbol{b}$ generated by the eddy currents $\boldsymbol{j}$: $\boldsymbol{B} = \boldsymbol{B}_0 + \boldsymbol{b}$. The induced field is seen as a distortion of the full field and can be calculated using the law of Biot-Savart [31]

$$\boldsymbol{b}(\boldsymbol{r}) = \frac{\mu}{4\pi} \int \frac{\boldsymbol{j}(\boldsymbol{r}') \times (\boldsymbol{r} - \boldsymbol{r}')}{|\boldsymbol{r} - \boldsymbol{r}'|^3} \, \mathrm{d}V' \, . \tag{1.34}$$

μ is the magnetic permeability of the fluid. Since $\boldsymbol{j}$ depends on $\boldsymbol{B}$ and thus on $\boldsymbol{b}$, (1.34) is an integral equation. However, if the magnitude of $\boldsymbol{b}$ is much smaller compared to $\boldsymbol{B}_0$, it can be neglected in the calculation of $\boldsymbol{j}$, i.e. $\boldsymbol{B} \approx \boldsymbol{B}_0$ in (1.28). This is called the quasistatic approximation. Under these circumstances, the strength of the induced magnetic field $\boldsymbol{b}$ can be estimated to be

$$b \sim \mu\sigma U l_m B_0 = \mathrm{Rm} B_0 \, . \tag{1.35}$$

Here, Rm is the magnetic Reynolds number

$$\mathrm{Rm} = \frac{U l_m}{\eta} = \mu\sigma U l_m \, , \tag{1.36}$$

with the magnetic diffusivity $\eta = 1/(\mu\sigma)$ of the fluid. Rm relates the effect of advection of $\boldsymbol{B}$ by the flow to the magnetic diffusion. The above estimates are valid if $b \ll B_0$ and thus $\mathrm{Rm} \ll 1$. As a result, if $\mathrm{Rm} \gtrsim 1$, the magnetic field could be altered by the flow and the quasistatic approximation is not valid.

Technically, B can also be significantly distorted for the $\mathrm{Rm} \ll 1$ case by so-called Alfven waves. For liquid metal experiments on laboratory scale these waves are, however, quickly attenuated [32] and have no impact on the flow.

The hydrodynamic Reynolds number Re_m, based on the length l_m, and the magnetic Reynolds number Rm are related by $\mathrm{Rm} = \mathrm{Pm} \mathrm{Re}_m$. The magnetic Prandtl number

$$\mathrm{Pm} = \frac{\nu}{\eta} = \mu\sigma\nu \tag{1.37}$$

compares the viscous and magnetic diffusion of the fluid and is, like the thermodynamic Prandtl number Pr, solely dependent on material properties. Given the small magnetic Prandtl numbers of liquid metals of $\mathrm{Pm} \sim 10^{-6}$ [32], very fast flows with $\mathrm{Re}_m \gtrsim 10^6$ are necessary to invalidate the quasistatic approximation. In the present experiments, the magnetic Reynolds number is always $\mathrm{Rm} \lesssim 0.02$, so the externally imposed magnetic field is considered to be unperturbed by the flow throughout the whole work.

Another consequence of the quasistatic approximation is that the electric field can be expressed as $\boldsymbol{E} = -\boldsymbol{\nabla}\varphi$ with the electric scalar potential φ. Thus, (1.28) becomes

$$\boldsymbol{j}(\boldsymbol{r}) = \sigma\left(-\boldsymbol{\nabla}\varphi(\boldsymbol{r}) + \boldsymbol{v}(\boldsymbol{r}) \times \boldsymbol{B}(\boldsymbol{r})\right) . \tag{1.38}$$

Using (1.38), the conservation of charge (1.29) and its boundary condition (1.30) translate into a Poisson equation for φ with Dirichlet boundary conditions:

$$\boldsymbol{\nabla}^2\varphi = \boldsymbol{\nabla} \cdot (\boldsymbol{v} \times \boldsymbol{B}) \qquad \text{in } V, \tag{1.39}$$

$$\boldsymbol{n} \cdot \boldsymbol{\nabla}\varphi = \boldsymbol{n} \cdot (\boldsymbol{v} \times \boldsymbol{B}) \qquad \text{on } S. \tag{1.40}$$

Some of the first theoretical calculations on magnetoconvection were done in the 1950s by Thompson [33] and Chandrasekhar [34, 35]. They considered the classical RBC system in an horizontally infinitely extended layer. The fluid has an electrical conductivity σ and the whole layer is subjected to a homogeneous, vertical magnetic field $\boldsymbol{B}$. This means, that $\boldsymbol{B}$ is parallel to the buoyancy forces: $\boldsymbol{B} = B\boldsymbol{e}_z$ and $\boldsymbol{g} = g\boldsymbol{e}_z$ with $B, g = \text{const}$. From general considerations of flows in an electrically conducting fluid it is known that magnetic fields suppress vortices whose axes of rotation do not coincide with the direction of the magnetic field [31]. Since buoyancy forces excite vertical flows, a vertical magnetic field is opposing the convective motion. As a result it is found that the critical Rayleigh number Ra_c for the onset of convection increases with the magnetic field. The relevant parameter for the strength of the magnetic field is in this case the Hartmann number Ha

$$\text{Ha} = BH\sqrt{\frac{\sigma}{\rho\nu}} \tag{1.41}$$

or, alternatively, the Chandrasekhar number $\text{Q} = \text{Ha}^2$. Here, the length scale is H, since the magnetic field spans the whole fluid. The value of Ra_c for small Ha depends on the boundary conditions at the horizontal surfaces (rigid walls or free surfaces, figure (1.5)). For $\text{Ha} \gtrsim 100$, all types of boundary conditions approach the same solution [5]

$$\text{Ra}_c \approx \text{Ra}_{\text{Ch}} \equiv \pi^2\text{Ha}^2 \qquad \text{for} \qquad \text{Ha} \gtrsim 100 . \tag{1.42}$$

This value Ra_{Ch} is called the Chandrasekhar limit. Equivalently, the critical Hartmann number for a constant value of Ra is

$$\text{Ha}_c \approx \text{Ha}_{\text{Ch}} \equiv \frac{\sqrt{\text{Ra}}}{\pi} \qquad \text{for} \qquad \text{Ra} \gtrsim 2 \times 10^5 . \tag{1.43}$$

In this thesis, Ra_c and Ha_c always refers to the exact numerical solution for the onset of convection (solid lines in figure 1.5), while Ra_{Ch} and Ha_{Ch} refers to the Chandrasekhar limit (1.42) and (1.43), respectively (dashed line). The procedure of calculating Ra_c and Ha_c for two rigid walls is described in appendix A.

1.4. Flow measurement techniques in liquid metals

A large number of experiments in fluid mechanics are conducted in transparent working fluids such as water, oils, or air. Optical measurement techniques are the standard in visualising the
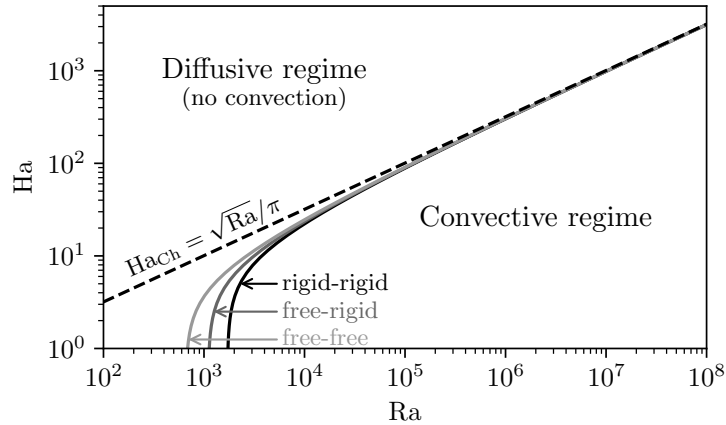
Figure 1.5.: Onset of Rayleigh-Bénard magnetoconvection for a horizontally infinitely extended fluid layer subject to a vertical magnetic field. Shown are the solutions $Ha_c(Ra)$ for three different types of boundary conditions (solid lines) and the asymptotic Chandrasekhar limit Ha_{Ch} (dashed line).

velocity field of a flow. Some of the most common methods are particle image velocimetry (PIV, [36]), laser Doppler velocimetry (LDV, [37]), or particle tracking velocimetry (PTV, [38]). Because of the opaque nature of liquid metals, such optical measurement techniques are not applicable and other ways have to be employed, to map the velocity field in these liquids. This section gives an short overview of methods used to measure velocities in liquid metals and will discuss the ones used in this thesis in more depth. For a more extensive review, the reader is referred to [39].

A broad categorisation of measurement techniques can be done by their invasiveness and whether they are in physical contact with the fluid. Invasive methods alter the flow in some way and it has to be evaluated, if the measured results are still representative of the unperturbed flow. If the flow is not changed by the measurement or the changes are negligible, the technique is called non-invasive. The second aspect covers, whether the measurement device is in direct contact with the fluid. If this is the case, the device has to resist the potentially hot or chemically aggressive liquid. Additionally, if the sensor is protruding into the flow, instead of e.g. being flush with the container walls, it always has to be treated as an invasive technique. Contactless measurement methods in turn have the advantage of being more readily applicable to aggressive fluids and often require less modification of the fluid container.

The most simplistic techniques belong to the invasive, contact-based category and work by mechanical principles. Refractory paddles can be inserted in the melt and are deflected by the flow or experience a torque based on the flow velocity [40]. In steel casting, the flow below a layer of slag is measured by submerging an array of steel rods into the liquid. The liquid steel solidifies around the rods and from the shape of this shell, the flow direction and speed can be deduced [40].

While visible, infrared, or ultraviolet light does not penetrate metals, it is possible to generate transmission images using X-ray radioscopy [41]. The absorption of X-rays along the beam path

is indicative of the local melt density. This method has the advantage of being contactless and non-invasive. The penetration depth is dependent on the attenuation by the liquid metal and the strength of the X-ray source, and can range from as little as 1 mm to 50 mm. A similar technique uses a neutron beam to visualise the flow [42]. This allows a sample thickness of the order of ~ 5 cm, but it can lead to an activation of the experimental set-up, which is then radioactive.

A well established way to determine velocities in opaque fluids is ultrasound Doppler velocimetry (UDV). This technique will be used extensively in this work and is thus introduced in detail in section 1.4.2.

A special property of liquid metals is their high electrical conductivity, which can be exploited for electromagnetic flow measurements. The first application of electromagnetic velocimetry is the attempt by Michael Faraday in 1832 to measure an electrical voltage across the river Thames induced in the flow by the Earth's magnetic field [31]. Though the experiment ultimately failed, the principle is used in modern electromagnetic flow meters [43]. A magnetic field imposed on a pipe or channel induces an potential difference in the flow, which can be measured by electrodes embedded in the side walls. This voltage is proportional to the volume flux through the pipe. For local measurements, this method can be scaled down into a so called potential or Vivès probe [39, 44]. By inserting the electrodes inside the flow, only a small distance apart, the velocity in between the electrodes can be deduced. An extension of this concept to arrays and grids of electrodes at container walls allows the measurement of two-dimensional, two-component velocity field near the wall [45].

The big advantage of inductive techniques is, however, the possibility of contactless measurements. The magnetic field induces eddy currents in the fluid. These in turn generate a secondary magnetic field, which is also present outside the fluid and can be measured there. Eddy current flow meters [46] induce eddy currents via an alternating magnetic field. These currents are then advected by the flow and their secondary magnetic field can be detected by induction coils. Contactless inductive flow tomography (CIFT) measures the secondary magnetic field of the flow-induced eddy currents at many positions around the fluid container and reconstructs the velocity field by solving an inverse problem [47]. One potential drawback of the presence of eddy currents in magnetic fields is the generation of Lorentz forces. Their influence on the flow has to be considered carefully, since they can alter the flow structure significantly.

However, this apparent downside is exploited by another flow measurement method. The same forces in the fluid also act on the external magnet system. This is exploited by Lorentz force velocimetry (LFV). The application of LFV to thermal convection in liquid metals is a central topic of this thesis and is discussed in the next section.

1.4.1. Lorentz force velocimetry

LFV has been developed in the first decade of the 21st century at the Technische Universität Ilmenau [48, 49], though the basic principle was well known beforehand [50]. It utilises the interaction of a magnet system with the flow of an electrically conducting fluid to probe the velocity field.

The fluid flow v is subjected to an external magnetic field B_0. Due to Ohm's law (1.38), eddy currents j are induced and generate a secondary magnetic field b (see figure 1.6). This magnetic field is not only present inside, but also outside of the fluid and can thus interact with the external
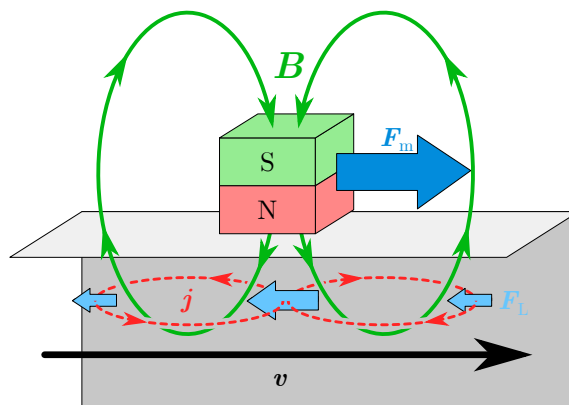
Figure 1.6.: Illustration of the measurement principle of Lorentz force velocimetry. The magnetic field $\boldsymbol{B}$ (solid green line) of a permanent magnet induces eddy currents $\boldsymbol{j}$ (dashed red lines) into the fluid due to the flow field $\boldsymbol{v}$ (black arrow). The interaction of $\boldsymbol{j}$ with $\boldsymbol{B}$ gives rise to Lorentz forces $\boldsymbol{F}_{\mathrm{L}}$ (light blue arrows) on the fluid which in total have the same magnitude as the force $\boldsymbol{F}_{\mathrm{m}}$ (dark blue arrow) on the magnet. Adapted from [Z2].

magnet system. If $\boldsymbol{B}_0$ is generated by a current density $\boldsymbol{j}_0$ in a coil, the induced field exerts a force

$$\boldsymbol{F}_{\mathrm{m}} = \int \boldsymbol{j}_0 \times \boldsymbol{b}\,\mathrm{d}V \qquad (1.44)$$

on the coil [49]. If the magnet system is a permanent magnet with an magnetisation $\boldsymbol{M}$, the fictitious current density $\boldsymbol{j}_0 = \boldsymbol{\nabla} \times \boldsymbol{M}$ can be used instead.

At the same time, the eddy currents in the fluid are interacting with $\boldsymbol{B}_0$, generating Lorentz forces $\boldsymbol{f}_{\mathrm{L}}$ in the flow (1.31). By virtue of Newtons' third law, the sum of all Lorentz forces in the fluid

$$\boldsymbol{F}_{\mathrm{L}} = \int \boldsymbol{f}_{\mathrm{L}}\,\mathrm{d}V = \int \boldsymbol{j} \times \boldsymbol{B}\,\mathrm{d}V \qquad (1.45)$$

is of the same magnitude and opposite sign as the force on the magnet system [49]

$$\boldsymbol{F}_{\mathrm{m}} = -\boldsymbol{F}_{\mathrm{L}}\,. \qquad (1.46)$$

For low magnetic Reynolds numbers $\mathrm{Rm} \ll 1$, the magnitude of $\boldsymbol{F}_{\mathrm{L}}$ can be estimated to be

$$|\boldsymbol{F}_{\mathrm{L}}| \equiv F_{\mathrm{L}} \sim \mu \sigma U B_0^2 l_{\mathrm{m}}^3\,. \qquad (1.47)$$

Here, l_{m} is a typical length scale of the magnetic field in the fluid (see section 1.3) and U is a characteristic flow velocity in the area of the magnetic field.

The scaling (1.47) shows, that F_{L} and consequently the force on the external magnet system is proportional to the flow velocity U. This is the central relationship of LFV: By measuring the
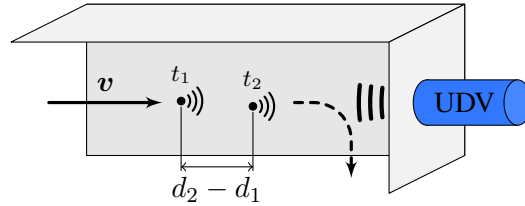
Figure 1.7.: Operating principle of UDV. A particle in a flow v towards a side-wall is at time t_i at a distance d_i from the UDV sensor ($i = 1, 2$). The particle velocity along the measurement line is then $(d_2 - d_1)/(t_2 - t_1)$.

force on the magnet system, the flow velocity in the area penetrated by the external magnet field can be deduced. The linear dependency of the Lorentz force on the velocity field v can also be shown more rigorously by calculating a general analytical solution of F_{L} (see section 2.3 and appendix B).

This measurement principle has been adapted to multiple devices and applications. Lorentz force flow-meters can be implemented as linear LFVs (measuring the force in one or multiple directions [48]) rotary LFVs (measuring the torque on the magnet system [48, 51]) or a combination of both [52]. Such measurement devices were used to detect the volume flux in liquid metal channel flows [53, 54]. An extension of the measurement technique towards low-conducting electrolytes was made possible by highly sensitive force measurement systems to compensate for the decrease in electrical conductivity by about six orders of magnitude [55, 56]. A different application was explored in the field of Lorentz force sigmometry [57], where the electrical conductivity of a fluid is determined from a known flow. Alternatively, the effect of the electrical conductivity can also be completely negated by applying a time-of-flight principle [58, 59]. These techniques all utilise magnet systems that subject the whole cross-section of a channel or pipe to a magnetic field. Local Lorentz force velocimetry (LLFV) instead uses small magnets compared to the fluid volume, to only probe certain parts of the flow [60]. This decrease of the measurement volume (i.e. l_{m}) also decreases the measured forces on the magnet system and requires more sophisticated force measurement equipment. However, it allows the detection of complex flow structures in e.g. channel flow [60], forced convection [61] and continuous casting moulds [62]. The above estimation of the Lorentz force magnitude (1.47) assumed the quasistatic approximation. In case of high velocities (i.e. $\mathrm{Rm} \gtrsim 1$) this does not apply and the linear dependency of the force on the flow speed is invalidated. However, it was shown that LFV can still be applied to such flows if the induced magnetic field is considered accordingly [63]. The opposite case of very low velocities was so far not investigated. Here, a potentially high interaction parameter $\mathrm{N} \gtrsim 1$ implies that the flow might be altered by the magnetic field. Thermal convection flows are especially susceptible to such disturbances, since their flow structures are very sensitive to external influences. This thesis will attend to this matter by developing and verifying theoretical models to predict whether the flow is significantly affected by the LFV measurement device.

1.4.2. Ultrasound Doppler velocimetry

The origin of ultrasound Doppler velocimetry (UDV) or ultrasound velocity profiling (UVP) lies in the medical application of blood flow measurement. The technique was first adapted for experimental fluid mechanics by Takeda [64] in 1986. The initial water experiments were soon followed by first measurements in liquid mercury the following year [65].

A transducer emits an ultrasonic wave with a well-defined f_0 frequency into the fluid using a piezoelectric actuator (see figure 1.7). The signal propagates with the speed of sound c in the fluid and is concentrated along a straight line in front of the sensor, the so called beam-line. Small particles scatter the wave and create echoes which can be recorded by either a second UDV sensor or by the first sensor itself. In so-called pulsed UDV, the transducer emits short ultrasonic pulses and measures the returning echoes during the idle period in between consecutive pulses.

To obtain the flow velocity from the particle echoes, two evaluation methods are available. First, the Doppler shift of the measured echoes can be evaluated. Depending on the particle velocity towards or away from the measuring sensor, frequency f of the reflected signal is shifted from the original emission frequency f_0. The particle velocity v parallel to the measurement line of the UDV sensor is then [64]

$$v = \frac{cf}{2f_0} \, .$$
(1.48)

The name UDV is derived from this evaluation method. The position d of the particle along the measurement line can be calculated from the time difference Δt between the signal emission and the return of the echo

$$d = \frac{c\Delta t}{2} \, .$$
(1.49)

The result is a one-dimensional and one-component velocity profile parallel to the measurement line. The disadvantage of this method is, that it relies on a single measurement and is thus very susceptible to noise.

The second method relies on the movement of particles over multiple successive measurements. If a particle stays within the ultrasonic beam for multiple measurements, the change of its distance d from the sensor gives the particle velocity along the beam-line. This operating principle is illustrated in figure 1.7. In practice this method is implemented by cross-correlation of multiple successive echo profiles. Like the previous evaluation, it results in a velocity profile parallel to the measurement line. The drawback of this method is a decreased time resolution. However, it gives the advantage of a more stable evaluation result. This is especially important for low velocity flows ($\lesssim 10\,\mathrm{mm\,s^{-1}}$), as is the case for thermal convection. In the present study this second evaluation method is used exclusively.

1.5. Scientific objectives of the thesis

The goal of this thesis is to investigate the effect of magnetic fields on thermal convection in liquid metal flows. This topic can be divided into two aspects:

1. An influence of the magnetic field on the velocity field is not desired and should be avoided.

    2. An alteration of the flow by the magnetic field is intended and the resulting effects are investigated and explained.

Both cases will be covered in the present thesis.

Avoiding a change of the flow field by applying a magnetic field is relevant for inductive measurement techniques. Ideally, a measurement device investigates a system without altering its properties. Here, the example system of a local Lorentz force velocimeter measuring the flow speed in a convection experiment will be considered in chapter 2. A major focus will be on the effect of localised magnetic fields, where the size of the affected fluid volume is not clearly defined and requires special consideration. The goal of the investigation is to find the threshold between the affected and unaffected flow regimes theoretically and confirm the findings experimentally. The theoretical calculations should be broadly applicable for numerous other types of set-ups, not just for the present experiment.

The opposite case of a convective system which is altered significantly by a magnetic field is investigated for the case of Rayleigh-Bénard magnetoconvection with an imposed vertical magnetic field. Measuring of the velocity field in liquid metals is notoriously difficult, due to their opaqueness. The present experiments aim to conduct a thorough analysis of the large-scale flow using ultrasound Doppler velocimetry and temperature sensors. The properties of the flow structure without the application of a magnetic field are to be compared with results from water experiments and their differences, and similarities are highlighted (chapter 4). Additionally, the global properties of heat and momentum transport are investigated. These measurements build the basis of the following chapter 5, where a magnetic field is applied to the system. The alterations of the flow structure are recorded and analysed. Here, it is of interest how the turbulence of the flow is suppressed and how the flow patterns adapt to the reduced flow speed. The heat transfer is expected to decrease with the flow intensity, but the exact relation is to be determined. The same dependency should be assessed for the momentum transport.

In addition to the experimental work, a theoretical investigation of the heat and momentum transfer is conducted in chapter 3. Predicting these properties in convective flows is a major research aspect and should be extended to the present case of magnetoconvection. A theoretical model is developed and tested with available experimental and numerical data. After the present experiments have been introduced, the theory will also be validated against these new results (section 5.4). This theory should also be useful to identify the relevant physical mechanisms responsible for the transport of heat and momentum in the fluid.

Finally a summary and a brief outlook are given.

2. Local Lorentz force velocimetry in vertical convection experiments

This chapter investigates the applicability of local Lorentz force velocimetry (LLFV) on thermal convection flows. The challenge of this topic primarily stems from the small characteristic velocities $U \lesssim 10^{-2}\,\mathrm{m\,s^{-1}}$ in such systems. The result of slower flow speeds is also a decrease of the force acting on the magnet system of the LLFV (1.47). Additionally, the interaction parameter $N \propto U^{-1}$ increases for small velocities (see (1.33)). This makes it imperative to ensure that the flow is not significantly altered by the induced Lorentz forces, which can be the case for $N \gtrsim 1$. Thermal convection systems are especially sensitive to external forces, because the dynamics and structure formation in such flows are often based on symmetries of the system, which can be easily broken. To counteract the increase of N, the magnet system can be adjusted. Using a smaller permanent magnet decreases the magnitude B of the magnetic field in the fluid and the volume it is influencing (represented in (1.33) by the length scale l_m). The disadvantage of such changes is an additional decrease of the forces measured by the LLFV.

This predicament of decreasing forces is intrinsic to LFV. As discussed before, the measured forces $\boldsymbol{F}_\mathrm{m}$ on the LFV magnet system have the same magnitude as the Lorentz forces $\boldsymbol{F}_\mathrm{L}$ acting on the fluid (see (1.46)). To not influence the flow, the induced forces have to be smaller than the driving forces of the flow, namely buoyancy forces. This, in extension, means that also the measured forces cannot be stronger than the driving of the flow. For LLFV to be useful in convection flows this upper limit of the forces acting upon the magnet system poses a requirement on the resolution of the force measurement system.

For the experimental test of LLFV on thermal convection, a vertical convection system (VC) is used. As will be discussed in the following section 2.1, this configuration generates a canonical flow structure of one large-scale convection roll. Afterwards, the experimental set-up is presented in section 2.2. The influence of the magnet system on the flow and the resulting LLFV measurements are then discussed in sections 2.5 and 2.4, respectively. Most of the content of this chapter was published in [Z2]. The publication also contains additional information on VC outside of the scope of this thesis, including heat and momentum transfer, details on the large-scale flow structure and velocity fluctuations.

2.1. Vertical convection

Vertical convection (VC) refers to a fluid confined between two opposing vertical walls which are heated or cooled, respectively (figure 2.1). This horizontal temperature gradient results in well defined regions of up- and down-welling flows: At the hot wall the fluid is rising while at the cold wall it is sinking down. In a closed cell, these streams are impinging on the top and bottom plates and are horizontally redirected to the other side of the cell, closing the flow structure into a
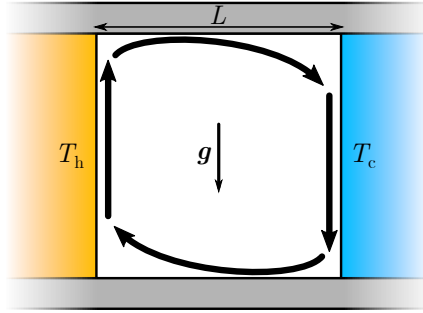
Figure 2.1.: Configuration of a vertical convection system. Opposing vertical side walls at a distance L are heated and cooled to constant temperatures T_h and T_c, respectively. The imposed temperature gradient is thus perpendicular to the acceleration $\boldsymbol{g}$ due to gravity.

single large-scale circulation across the whole cell. The direction of this convection roll is fixed and gives a predictable, canonical flow, which are ideal properties to test LLFV on.

As opposed to Rayleigh-Bénard convection, VC displays convective motion at any temperature difference ΔT between the side walls. The Rayleigh number Ra, here defined using the distance L between the heated/cooled side walls, does not have to exceed a critical value for a flow to set in.

2.2. Experimental set-up

The experiment is conducted in a rectangular cell (figure 2.2). The heated and cooled side walls are at a distance of $L = 150\,\mathrm{mm}$ and are build as copper heat exchangers, each supplied with water by a thermostat. The other cell walls are made of PMMA. The height of the cell is $H = 148\,\mathrm{mm}$ and its thickness is $30\,\mathrm{mm}$. The coordinate system is oriented with z as the vertical axis and x as the wall normal of the copper plates. The whole cell is thermally insulated using insulation wool and Styrofoam.

The working fluid in the cell is gallium-indium-tin (GaInSn). At its eutectic composition of $67\,\mathrm{wt\%}$ gallium, $20.5\,\mathrm{wt\%}$ indium, and $12.5\,\mathrm{wt\%}$ tin, this alloy has a melting temperature of $10.6\,°\mathrm{C}$ [66]. Its material properties are listed in table 2.1. Of importance is the low Prandtl number. Its value ranges from $\mathrm{Pr} = 0.033$ at $20\,°\mathrm{C}$ to $\mathrm{Pr} = 0.026$ at $50\,°\mathrm{C}$.

The plate temperatures are measured using thermocouples of type K. They are positioned at the centre of the copper plates and their tips are in direct contact with the liquid metal. The temperature of the cold and hot plate are denoted by T_c and T_h, respectively. The temperature difference is then $\Delta T = T_h - T_c$ and the mean temperature of the fluid is $\bar{T} = (T_c + T_h)/2$.

The LLFV measurement system is positioned at the top centre of the cell. A cubic permanent magnet of side length $5\,\mathrm{mm}$ is positioned so that its magnetisation is in vertical direction and its centre is at a distance of $h = 7.5\,\mathrm{mm}$ from the upper fluid surface. Thus, the magnetic field is localised at the PMMA lid with electrically insulating boundary condition. The force on this magnet is measured using an interference optical force sensor (IOFS) with a resolution of $15\,\mathrm{nN}$ [60]. Only the force component F_x in x-direction is measured, since the flow is expected
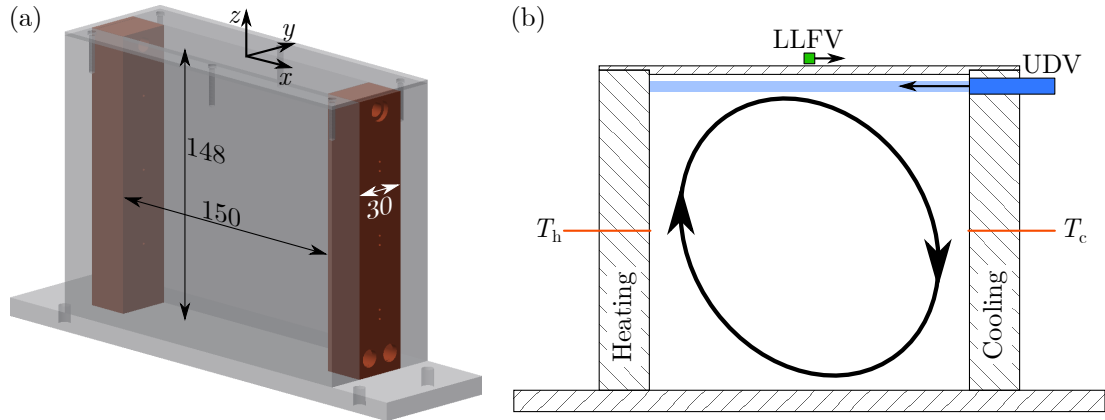
Figure 2.2.: Set-up of the vertical convection experiment. (a) Image of the cell with coordinate system and inner dimensions in mm. (b) Placement of the measurement sensors: The ultrasonic transducer (UDV, blue), thermocouples (T_h and T_c, red) and the 5 mm-magnet (LLFV, green). The beam-line of the UDV-sensor is indicated as a light blue stripe. The convective flow is sketched for heating on the left and cooling on the right side of the cell.

to predominantly move in that direction (see section 2.1). The set-up was mounted on a heavy granite stone to damp vibrations coming from the surrounding.

For comparison, an 8 MHz UDV sensor is used to measure the horizontal velocity near the cell top using a DOP3010 system. The sensor has a piezo-actuator of 5 mm diameter. It is embedded into the copper plate and in direct contact with the liquid. The beam-line centre is 5.5 mm below the upper fluid surface.

2.3. The measurement volume of LLFV

For the measurement of local velocities using LFV, it is important to know the size of the fluid volume, which contributes to the final signal. This quantity is rather ambiguous: (i) There is no natural, well-defined cut-off distance at which the magnetic field is too weak to generate a significant signal. (ii) The correct area of influence requires knowledge of the velocity field, which is often not the case and defeats the purpose of a flow measurement system. Point (i) is a question of convention about how to define a cut-off point. Point (ii) on the other hand is more inconvenient, since any single LLFV system would have to be considered with a number of different flows, to characterise its measurement volume.

Such a characterisation has been done by Heinicke [68] for pipe flow. There, a Poiseuille-type flow profile was assumed and the Lorentz force density was calculated numerically. The measurement volume had been defined as a sphere around the magnet system, that included 95 % of the induced Lorentz forces. The extent of this sphere into the fluid is the penetration depth d of the LLFV. Such an approach gives accurate results for any single application. However, its results are not easily transferable to other flow types.

Mass density	$\rho = 6.34 \times 10^3 \, \mathrm{kg \, m^{-3}}$
Kinematic viscosity	$\nu = 3.15 \times 10^{-7} \, \mathrm{m^2 \, s^{-1}}$
Dynamic viscosity	$\nu\rho = 2.00 \times 10^{-3} \, \mathrm{Pa \, s}$
Thermal conductivity	$\lambda = 24.9 \, \mathrm{W \, m^{-1} \, K^{-1}}$
Isobaric heat capacity	$c_p = 364 \, \mathrm{J \, kg^{-1} \, K^{-1}}$
Thermal diffusivity	$\kappa = 1.08 \times 10^{-5} \, \mathrm{m^2 \, s^{-1}}$
Volumetric expansion coefficient	$\alpha = 1.24 \times 10^{-4} \, \mathrm{K^{-1}}$
Electrical conductivity	$\sigma = 3.20 \times 10^6 \, \mathrm{S \, m^{-1}}$
Magnetic diffusivity	$\eta = 2.49 \times 10^{-1} \, \mathrm{m^2 \, s^{-1}}$
Prandtl number	$\mathrm{Pr} = 0.029$
Magnetic Prandtl number	$\mathrm{Pm} = 1.3 \times 10^{-6}$

Table 2.1.: Material properties of eutectic GaInSn at 35 °C [66, 67].

In this section a velocity-independent solution to point (ii) is developed. The penetration depth of a LLFV system into a flow is calculated for a simplified set-up that is suitable to a wide variety of applications. The influence of the velocity field is decoupled from all other parameters and can thus be excluded from the definition of the penetration depth d. The somewhat lengthy calculations are deferred to appendix B. Here, a short summary is given.

The present set-up is reduced to a cubic permanent magnet over an infinite half-space $z \leq 0$ filled with an electrically conducting fluid. The velocity field in the fluid is assumed to have one horizontal component and to be dependent on the vertical depth only: $\boldsymbol{v}(\boldsymbol{r}) = v_x(z)\boldsymbol{e}_x$. These simplifications are justified, if the LLFV system is small in comparison to the size of the cell dimensions and the size of the flow structures. In the quasistatic approximatio, it can be shown that the accumulative Lorentz force $\boldsymbol{F}_\mathrm{L}$ (see (1.45)) only has one component in direction of the velocity field

$$F_{\mathrm{L},x} = \int_{-\infty}^{0} v_x(z)\tilde{w}(z) \, \mathrm{d}z \,. \tag{2.1}$$

The sensitivity function $\tilde{w}(z)$ (see (B.30b)) characterises the contribution of the flow field in a certain depth towards the total induced Lorentz force. It is independent of the velocity field and can be calculated from the spatial distribution of the magnetic field and the shape of the fluid volume. For the present set-up, using a 5 mm magnet at a distance of $h = 7.5\,\mathrm{mm}$, $\tilde{w}_x(z)$ is plotted in figure 2.3(a). The sensitivity function is used to calculate the relative contribution $\tilde{P}(z)$ of the flow up to a certain depth z towards the total force

$$\tilde{P}(z) = \frac{\int_{z}^{0} \tilde{w}(z') \, \mathrm{d}z'}{\int_{-\infty}^{0} \tilde{w}(z') \, \mathrm{d}z'}, \quad z \leq 0 \,. \tag{2.2}$$

The penetration depth d_{95} is now defined as the position, at which the relative contribution reaches $\tilde{P} = 95\,\%$ (following the convention by Heinicke [68]). For the present set-up a value of $d_{95} = 10.6\,\mathrm{mm}$ is calculated using linear interpolation (see figure 2.3(b)). This value can be applied to any kind of flow, where the flow structures and overall fluid volume are larger than the magnet system and where the quasistatic approximation applies.
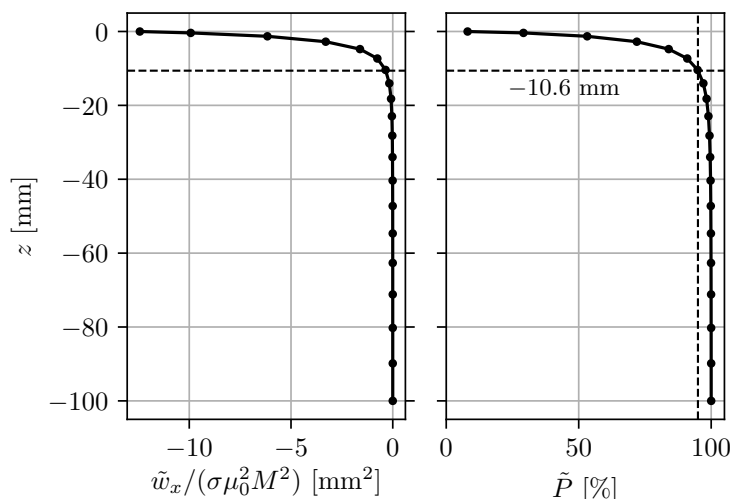
Figure 2.3.: Characteristic quantities of a LLFV with a 5 mm magnet at a distance of 7.5 mm from the fluid. (a) Sensitivity function $\tilde{w}_x(z)$, normalised by the electrical conductivity σ of the fluid and the remanence $\mu_0 M$ of the magnet. (b) Relative contribution $\tilde{P}(z)$ of the flow up to a given depth z towards the total Lorentz force. The dashed lines indicate the penetration depth of the LLFV at $\tilde{P} = 95\,\%$.

The above definition of the penetration depth is equivalent to the one used by Heinicke [68], if a solid body translation would be considered, i.e. $v_x(z) = v_x = \mathrm{const.}$ This is generally not the case in experiments. Often, no-slip conditions apply to the fluid boundaries and the velocities are smallest near the surface. Additionally, the low sensitivity at higher depths might be compensated by faster velocities in these depths. As a consequence, realistic velocity profiles generally result in higher penetration depths. In the case mentioned before, Heinicke [68] found a penetration depth of 38 mm for the present set-up when applied to a Poiseuille flow profile. If a velocity profile should be included in the calculation of the penetration depth, the definition of $\tilde{P}$ can be easily adjusted by replacing $\tilde{w}_x(z) \to v_x(z)\tilde{w}_x(z)$ in (2.2).

2.4. The influence of a magnet on the convective flow

To investigate the interaction of a magnet with the convective flow, a cubic NdFeB magnet with an edge length of 10 mm is placed at different heights h above the centre of the cell. The heating and cooling thermostats are set to constant temperatures of 40 and 15 °C, respectively, to drive a flow. The horizontal velocity profile below the cell lid is measured by the UDV sensor. Figure 2.4(a) shows the time-averaged profiles $v_x(x)$ for different magnet distances h. For large $h \gtrsim 20$ mm, the velocity profile does not change from the unperturbed state: The fluid flows from left to right and the horizontal velocity slowly decreases over the cell width. Once the magnet gets closer to the fluid, the velocity profile is strongly altered: The magnitude of the profile decreases and for the closest position $h = 10$ mm, the velocity starts to rapidly drop at the position of the magnet. This suggests, that the magnet acts as a magnetic obstacle and the horizontal flow along the top
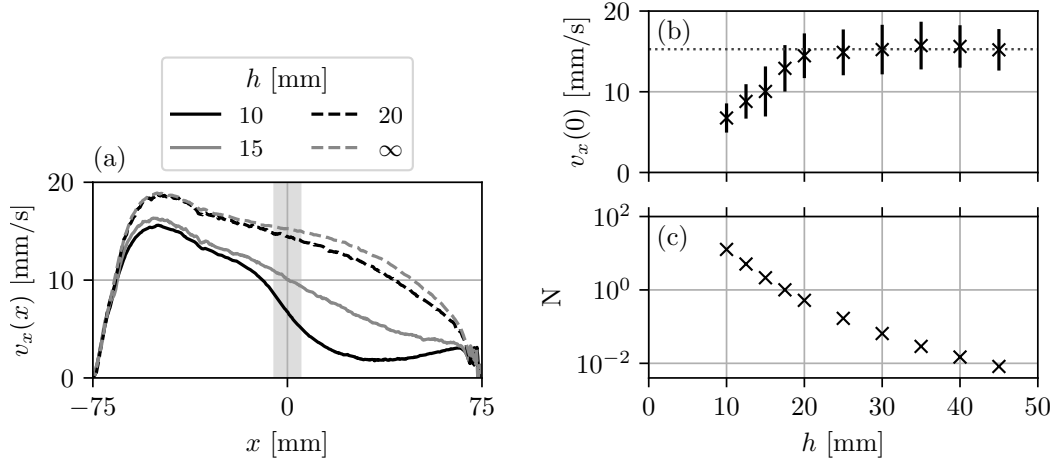
Figure 2.4.: Influence of a 10 mm magnet on the convective flow. (a) Time-averaged horizontal velocity profiles $v_x(x)$ below the cell lid for different magnet distances h. The light grey area indicates the position and size of the magnet. $h = \infty$ means that the magnet had been removed completely. (b) Average velocity $v_x(0)$ directly below the magnet vs. the magnet position. The dotted line gives the value of $v_x(0)$ for $h = \infty$. The error bars give the standard deviation of the measurements. (c) Interaction parameter N vs. the magnet position.

of the cell is redirected downwards.

Figure 2.4(b) shows the average velocity at $x = 0$ in the centre of the cell for different magnet positions h. The diagram shows that the flow is influenced, if the magnet is closer than a critical distance $h \sim 20$ mm. Above this value, the velocities do not deviate from the unperturbed state, indicated by the dotted line.

As discussed in the introduction, whether a flow is altered by an applied magnetic field can be estimated by the interaction parameter. Its definition was

$$N = \frac{\sigma B^2 l_{\mathrm{m}}}{\rho U} \,. \tag{1.33}$$

The material parameters σ and ρ of the fluid are calculated at the mean fluid temperature $\bar{T}$ [66]. The maximum magnetic flux density B in the fluid is measured at the top surface of the cell directly below the magnet. For the velocity scale, the unperturbed horizontal velocity $U = v_x(0)$ is used, i.e. for $h = \infty$ (figure 2.4(b)). Lastly, the magnetic length scale l_{m} is defined as the penetration depth d_{95} of the magnet. It is calculated as described in the previous section 2.3 for the present magnet size of 10 mm and the respective magnet position h (the exact values are listed in table B.1 of appendix B.2). The resulting values of N are plotted as a function of h in figure 2.4(c). The interaction parameter decreases continually, as the magnet moves away from the cell. Between $h = 17.5$ mm and 20 mm, it crosses the N $= 1$ threshold. When compared to the central velocity in figure 2.4(b), this distance is the same value at which the velocity profiles start to deviate from the unperturbed state. Thus, the choices of the characteristic quantities to
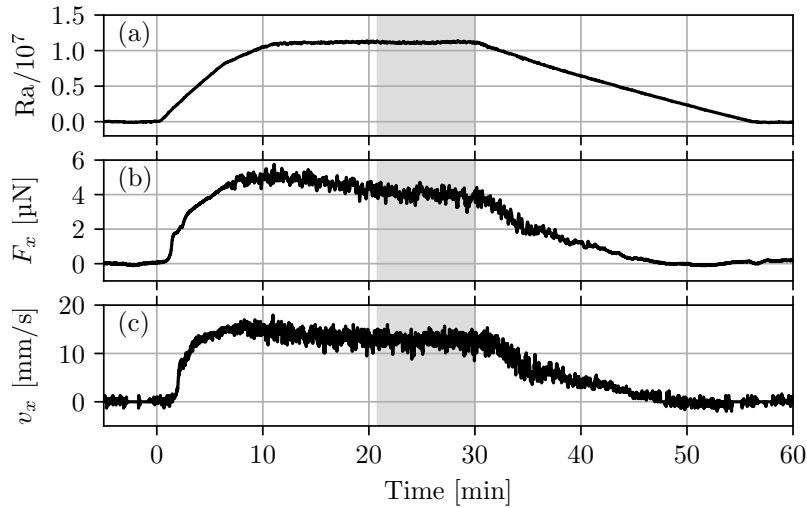
Figure 2.5.: Exemplary time series of multiple quantities in a vertical convection experiment. (a) The Rayleigh number reaches a plateau at $\mathrm{Ra} = 1.1 \times 10^7$. (b) The force F_x on the LLFV, corrected by its initial offset. (c) The horizontal velocity measured by the UDV sensor at the point $x = 0\,\mathrm{mm}$. The light grey area marks the time range used for averaging the quantities.

calculate N – especially $l_\mathrm{m} = d_{95}$ – give a good prediction of the threshold beyond which the flow is altered by the magnetic field.

2.5. Force scaling

Experiments are conducted for constant Rayleigh numbers $3.7 \times 10^5 \leq \mathrm{Ra} \leq 3.2 \times 10^7$. The cooling and heating temperatures T_cold and T_hot, respectively, are set to a constant value of $15\,°\mathrm{C}$. Then T_hot is increased to a fixed target temperature in the range $15\,°\mathrm{C} < T_\mathrm{hot} < 60\,°\mathrm{C}$. Figure 2.5 shows the time-lines of the Rayleigh number, measured force and horizontal velocity for a typical experiment. The measurement starts at $\Delta T = 0$ to record the zero signal of the LLFV force F_x. At $t = 0$, the heating temperature is increased and reaches a constant value of $24.5\,°\mathrm{C}$ ($\mathrm{Ra} = 1.1 \times 10^7$) 10 min later. The convective flow develops and settles at $t \sim 20\,\mathrm{min}$, after which both the force and velocity remain constant. Now, data is collected for 10 min and at $t = 30\,\mathrm{min}$ the heating temperature is decreased again until it reaches its initial value. At the end a second zero signal of the force is recorded and the experiment is finished. For other Ra, the time to reach the constant plateau is different, but the plateau length is kept constant for all measurements.

The force offset at the beginning and end of the experiment is important, because the force measurement is very sensitive to outside perturbations. The force signal often drifted over time. For experiment durations of $\sim 1\,\mathrm{h}$ these drifts were mostly linear and could be corrected. A linear function is fitted to the zero signals at the beginning and the end of the measurement and subtracted from the whole signal. However, for longer durations the drifts could change over
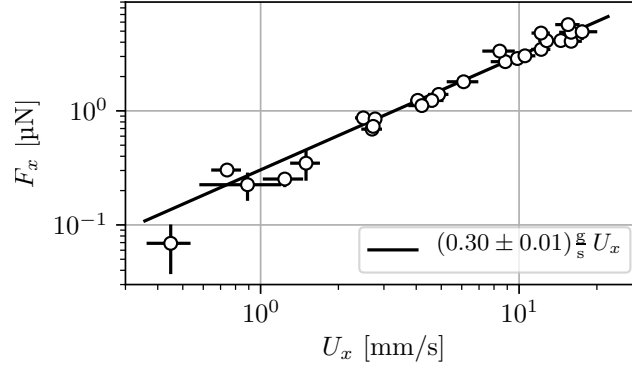
Figure 2.6.: Scaling of the force F_x on the LLFV magnet with the flow velocity U_x measured by the UDV sensor. The errors are the standard deviations of the averaged values.

time and it was not possible to accurately correct the force signal afterwards. These drifts may be caused by various effects, but no definitive culprit could be found. Candidates are the changing surrounding temperature due to the heating plate, electromagnetic signals from the surrounding electrical devices or vibrations from the building. The last part was not fully eliminated by the granite plate the experiment was mounted on, since the force measurement could detect a person walking around in the laboratory. Consequently, the experiments had to be fully automated and were run overnight to avoid disturbances during working days.

For comparison of the measured force, the velocity profile $v_x(x, t)$ measured by the UDV sensor is averaged over time and the interval $-10\,\text{mm} \leq x \leq 10\,\text{mm}$ below the magnet. This gives a characteristic horizontal flow velocity

$$U_x = \left\langle v_x(x, t) \right\rangle_{t, -10\,\text{mm} \leq x \leq 10\,\text{mm}} . \tag{2.3}$$

The interval size is chosen to be of the order $\sim d_{95} = 10.6\,\text{mm}$ as calculated in section 2.3.

Figure 2.6 shows the time averaged force F_x measured by the LLFV plotted against the velocity U_x. A linear fit to the data using orthogonal distance regression shows, that the general relation $F_x \propto U_x$ holds in this convective system. The deviations from the linear fit at low velocities stem from the small force amplitudes $\sim 0.1\,\mu\text{N}$, which approach the sensor resolution of $0.015\,\mu\text{N}$. For larger velocities of $\sim 10\,\text{mm s}^{-1}$ the increased turbulence generates a spreading of the measurement points.

The interaction parameter N of the system is calculated as shown in the previous section 2.4, with U_x as the velocity scale. Values of N over Ra are displayed in figure 2.7(a). It shows that for Ra $\lesssim 10^7$ the interaction parameter is larger than 1. This means, that for most of the measurements the flow may be altered by the magnetic field of the LLFV. To verify this, the experiments are repeated without the presence of the LLFV magnet system. The velocities U_x with and without the influence of the permanent magnet are plotted in figure 2.7(b). The velocities do not show a significant deviation from one another. Consequently, the influence of the magnet is not strong enough to significantly alter the flow in the present case.
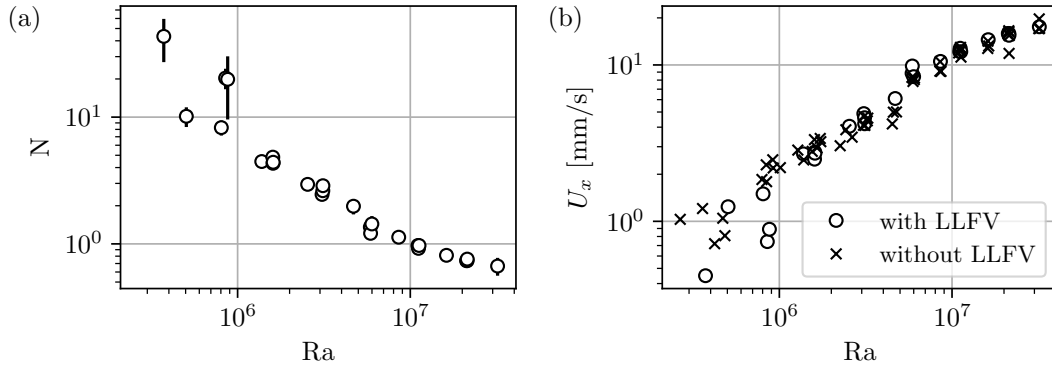
Figure 2.7.: (a) Interaction parameter N over Rayleigh number Ra. (b) Characteristic horizontal velocity U_x over Rayleigh number Ra with and without the influence of the LLFV.

2.6. Concluding remarks

It has been shown, that the linear dependence of the force measured by a LLFV on the fluid velocity applies also to slow convective flows. In these systems, additional care has to be taken to not alter the investigated flow in the high-N regime. In contrast to the high-Rm regime at high velocities [69], these changes cannot be incorporated into the calibration of the measurement system. If it is possible to conduct direct comparison of the flow with and without the LLFV it can be verified, whether the measurement system is altering the flow. However, if this is not feasible the threshold $N = 1$ can be taken as an boundary for the design of measurement systems. The calculation strategy of N given in section 2.4 and appendix B.2 gives a clear threshold, which is applicable to not only LFV systems, but all inductive measurement methods employing localised magnetic fields. In addition, it provides a rigorous theoretical definition of the fluid volume affected by induced Lorentz forces, independently of the specific velocity field. Though if desired, the calculation is easily expandable to arbitrary one-dimensional velocity profiles.

3. Theory of heat and momentum transport in magnetoconvection

As described in section 1.2, the transport of heat and momentum are important global properties of thermal convection systems. Since the presence of a magnetic field can significantly alter the flow structure of an electrically conducting fluid, it also has an effect on Nu and Re. The Grossmann-Lohse theory does not incorporate these effects and has to be adjusted to be relevant in magnetoconvection.

In this chapter the addition of a vertical homogeneous magnetic field to the RBC system is considered. Most of the results of sections 3.1 and 3.2 have been published in [Z1].

3.1. Extension of the Grossmann-Lohse theory by magnetic dissipation

The eddy currents $\boldsymbol{j}$ induced in a flow by an external magnetic field $\boldsymbol{B}_0$ generate heat via Joule dissipation. The power density associated with this process is [31]

$$\frac{\partial P}{\partial V} = \frac{1}{\sigma} \boldsymbol{j}^2 . \tag{3.1}$$

Since the strength of the eddy currents is proportional to the electrical conductivity σ of the fluid (see (1.38)), the Joule dissipation is also expected to increase linearly with σ. The local magnetic dissipation rate (DR) is given by $\epsilon_\sigma = \mu \partial P / \partial V$. With $\mu \boldsymbol{j} = \boldsymbol{\nabla} \times \boldsymbol{b}$ this results in

$$\epsilon_\sigma = \eta \left(\boldsymbol{\nabla} \times \boldsymbol{b} \right)^2 = \eta \left[(\partial_i b_k)^2 - (\partial_i b_k)(\partial_k b_i) \right] . \tag{3.2}$$

Here, $\boldsymbol{b} = b_i \boldsymbol{e}_i$ is the induced magnetic field, generated by the eddy currents $\boldsymbol{j}$. The relevant fluid property is the magnetic diffusivity $\eta = 1/(\mu\sigma)$ with the magnetic permeability μ. For liquid metals, the latter is generally assumed to be equal to the permeability of free space μ_0. The mean magnetic DR in the fluid is then given by

$$\varepsilon_\sigma \equiv \langle \epsilon_\sigma \rangle_{V,t} = \eta \left\langle (\partial_i b_k)^2 \right\rangle_{V,t} , \quad i \neq k . \tag{3.3}$$

The mixed terms $\langle (\partial_i b_k)(\partial_k b_i) \rangle_{V,t}$ vanish for $i \neq k$, since the induced magnetic field $\boldsymbol{b}$ is generated by the isotropic turbulence of the flow and thus different elements of its Jacobian matrix are considered to be uncorrelated. It should be mentioned that the present definitions of ϵ_σ and ε_σ are slightly different from other publications [Z1, 70], which include an additional factor of $1/(\mu\rho)$. The definition used here is motivated by consistent dimensions of the dissipation

rates ϵ_ν, ϵ_κ and ϵ_σ. The viscous DR ϵ_ν is measured in $(m/s)^2 s^{-1}$ and the thermal DR ϵ_κ has the unit $K^2 s^{-1}$. With the present definition the magnetic DR ϵ_σ has the physical dimension $T^2 s^{-1}$.

Introducing $\boldsymbol{B}_0$ into the GL theory does not affect equation (1.15) containing the thermal DR. In equation (1.14), however, the magnetic DR is introduced [70]

$$\varepsilon_\nu + \frac{\varepsilon_\sigma}{\mu\rho} = \frac{\nu^3}{H^4} \frac{(\mathrm{Nu}-1)\mathrm{Ra}}{\mathrm{Pr}^2}\,. \tag{3.4}$$

This shows that, in addition to viscous damping, the dissipation of kinetic energy is enhanced by Joule damping. Estimating the magnitude of these two effects in the quasistatic approximation (using (1.35)) gives

$$|\varepsilon_\nu| \sim \nu \frac{U^2}{H^2}\,, \tag{3.5}$$

$$\left|\frac{\varepsilon_\sigma}{\mu\rho}\right| \sim \frac{\sigma B^2 H^2}{\rho} \frac{U^2}{H^2} = \nu_\sigma \frac{U^2}{H^2}\,. \tag{3.6}$$

Thus, the damping due to Joule dissipation can be considered as an additional "magnetic viscosity" $\nu_\sigma = \sigma B^2 H^2/\rho$ [71]. The ratio $\nu_\sigma/\nu = \mathrm{Ha}^2$ relates the relative size of these effects directly to the Hartmann number. While this estimation is helpful for the physical understanding of the system at hand, it needs to be remembered that Joule damping is anisotropic and acts on all scales of the flow [71]. In this, it differs significantly from the kinematic viscosity.

In 2008, Chakraborty [70] used equation (3.4) and (1.15) to derive pure scaling laws for Nu and Re analogously to the first publication by Grossmann and Lohse [24]. To achieve this, he assumed that $\varepsilon_\nu \sim \varepsilon_\sigma/(\mu\rho)$ and split (3.4) into two equations. The drawback of this approach is, that it employs three equations (for ε_ν, ε_σ and ε_κ) to calculate two quantities (Nu and Re), which is an overdetermined system of equations. In the present derivation, instead of pure scaling laws for different regimes, a unified theory will be developed similarly to the GL theory (see section 1.2.2).

For the first step, the three dissipation rates are, again, split into their respective bulk and boundary layer (BL) contributions. In addition to (1.16) and (1.17) this gives

$$\varepsilon_\sigma = \varepsilon_{\sigma,\mathrm{BL}} + \varepsilon_{\sigma,\mathrm{Bulk}}\,. \tag{3.7}$$

Secondly, approximations of the scalings for the BL and bulk contributions to all three dissipation rates have to be derived. For this, a number of assumptions have to be made.

The Prandtl number is restricted to very small values $\mathrm{Pr} \ll 1$. This eliminates the need for an additional free model parameter, which was introduced into the GL theory for the regime of high $Pr \gg 1$ [25]. Fluids in the low-Prandtl number regime include liquid metals and plasmas.

The quasistatic approximation is used, i.e. the induced eddy currents $\boldsymbol{j}$ are not affected by their own secondary magnetic field $\boldsymbol{b}$ and the time evolution of the magnetic field can be neglected. This requires that $\mathrm{Rm} \ll 1$, which excludes a number of geo- and astrophysical phenomena, e.g. planetary and stellar dynamos.

At high Hartmann numbers $\mathrm{Ha} \gg 1$, alterations to the system have to be considered for the onset of convection and boundary layers (BL). As noted in section 3.1, the onset of convection

reaches the Chandrasekhar limit (1.42) for strong magnetic fields. This scaling of the critical Rayleigh number will be included in the theory.

The viscous BL thickness δ_v is changed by the magnetic field and the Blasius-type BL is no longer applicable. A vertical magnetic field $\boldsymbol{B} \parallel \boldsymbol{g}$ is perpendicular to the horizontal boundaries of the fluid layer. When assuming a flow parallel to the top and bottom plate the BL can be interpreted as a Hartmann layer. In this case, the Lorentz forces decrease the viscous BL thickness which becomes [31]

$$\delta_B = \frac{H}{\text{Ha}} \,. \tag{3.8}$$

In contrast to the Blasius BL δ_v, the Hartmann layer δ_B does not contain a free parameter. The thermal BL thickness δ_T is still given by (1.12). It is affected by the magnetic field only indirectly, since the Nusselt number is now a function of the Hartmann number, as well as the Rayleigh and Prandtl numbers.

Under these assumptions and approximations, the dissipation rate contributions can be estimated as follows: The scaling arguments for the viscous and thermal dissipation rates are the same as for the standard GL theory (1.19) – (1.22). The only difference appears for $\varepsilon_{\nu,\text{BL}}$, where the estimate employs the Hartmann layer thickness δ_B instead of the Blasius layer thickness δ_v The resulting equations are

$$\varepsilon_{\nu,\text{BL}} \sim \nu \frac{U^2}{\delta_B^2} \frac{\delta_B}{H} = \frac{\nu^3}{H^4} \text{Re}^2 \text{Ha} \,, \tag{3.9}$$

$$\varepsilon_{\nu,\text{Bulk}} \sim \frac{U^3}{H} = \frac{\nu^3}{H^4} \text{Re}^3 \,, \tag{3.10}$$

$$\varepsilon_{\kappa,\text{BL}} \sim \kappa \frac{(\Delta T)^2}{H^2} (\text{PrRe})^{1/2} \,, \tag{3.11}$$

$$\varepsilon_{\kappa,\text{Bulk}} \sim \frac{U(\Delta T)^2}{H} = \kappa \frac{(\Delta T)^2}{H^2} \text{PrRe} \,. \tag{3.12}$$

Estimates for the magnetic dissipation rate contributions are based on the definition (3.3). Using (1.35) to estimate the induced field strength and H as the characteristic length scale in the bulk, $\varepsilon_{\sigma,\text{Bulk}}$ scales as

$$\varepsilon_{\sigma,\text{Bulk}} \sim \eta \frac{\text{Rm}^2 B_0^2}{H^2} = \mu \rho \frac{\nu^3}{H^4} \text{Re}^2 \text{Ha}^2 \,. \tag{3.13}$$

Similarly, taking δ_B as typical length scale for the viscous BL and considering the volume fraction δ_B/H gives

$$\varepsilon_{\sigma,\text{BL}} \sim \eta \frac{\text{Rm}^2 B_0^2}{\delta_B^2} \frac{\delta_B}{H} = \mu \rho \frac{\nu^3}{H^4} \text{Re}^2 \text{Ha}^3 \,. \tag{3.14}$$

3.1.1. Regime transitions

Similar to the GL theory, the above estimates need to be altered, if the system transitions into a different flow regime. The first transition considered in the GL theory was the nesting

of viscous and thermal BL (see section 1.2.2). Similarly to the GL theory, the transition is modelled by replacing $U \to U f(x_T^n)$ in the thermal DR contributions (3.11) and (3.12). Here, $f(x_T) = (1 + x_T^n)^{-1/n}$ with $n = 4$ and $x_T = \delta_B/\delta_T$. The only difference with respect to the original GL theory is, that by using the Hartmann layer δ_B instead of a Blasius BL, the crossover variable becomes $x_T = 2\mathrm{Nu}/\mathrm{Ha}$.

While a laminarisation due to high Prandtl numbers is not considered here, a similar effect has to be taken into account for convection close to the onset. The scaling of $\varepsilon_{\nu,\mathrm{Bulk}} \propto \mathrm{Re}^3$ in (3.10) assumes a fully turbulent bulk flow. However, if the flow is laminar, the scaling becomes $\varepsilon_{\nu,\mathrm{Bulk}} \sim \nu U^2/H^2 = (\nu^3/H^4)\mathrm{Re}^2$. This transition between laminar and turbulent convection takes place over a wide range of Re, including non-linear flow in between laminar and turbulent states. Adapting the approach of the large Prandtl number regime (see section 1.2.2), the transition is characterised with a Reynolds number Re^*, which is a new unknown model parameter. The transition is then modelled by multiplying $\varepsilon_{\nu,\mathrm{Bulk}}$ with the function $g(x^*) = 1/f(1/x^*)$, where $x^* = \mathrm{Re}/\mathrm{Re}^*$.

Now, each of the contribution estimates (3.9)–(3.14) including the above regime transitions are each multiplied by a constant pre-factor c_i, $i = 1, \ldots, 6$, and combined to the full mean dissipation rates (1.16), (1.17) and (3.7). Inserting these into the exact scaling relations (3.4) and (1.15) results in

$$\frac{(\mathrm{Nu} - 1)\mathrm{Ra}}{\mathrm{Pr}^2\mathrm{Re}^2} = c_1\mathrm{Re}\, g\!\left(\frac{\mathrm{Re}}{\mathrm{Re}^*}\right) + c_2\mathrm{Ha} + c_3\mathrm{Ha}^2 + c_4\mathrm{Ha}^3 \,, \tag{3.15}$$

$$\mathrm{Nu} - 1 = c_5\mathrm{Re}\mathrm{Pr}\, f\!\left(\frac{2\mathrm{Nu}}{\mathrm{Ha}}\right) + c_6\sqrt{\mathrm{Re}\mathrm{Pr}\, f\!\left(\frac{2\mathrm{Nu}}{\mathrm{Ha}}\right)}\,. \tag{3.16}$$

These model equations cannot be solved analytically for $\mathrm{Nu}(\mathrm{Ra}, \mathrm{Ha}, \mathrm{Pr})$ and $\mathrm{Re}(\mathrm{Ra}, \mathrm{Ha}, \mathrm{Pr})$. However, (3.16) can be solved for a function $\mathrm{Re}(\mathrm{Nu}, \mathrm{Ra}, \mathrm{Ha}, \mathrm{Pr})$

$$\mathrm{Re} = \frac{\left(\sqrt{c_6^2 + 4c_5(\mathrm{Nu} - 1)} - c_6\right)^2}{4c_5^2\mathrm{Pr}\, f\!\left(\frac{2\mathrm{Nu}}{\mathrm{Ha}}\right)}\,. \tag{3.17}$$

Using (3.17), Re can now be eliminated from (3.15). The resulting equation is numerically solvable for $\mathrm{Nu}(\mathrm{Ra}, \mathrm{Ha}, \mathrm{Pr})$

However, one last regime transition has to be considered beforehand. The above equations do not inherently reproduce the onset of convection, i.e. $\mathrm{Nu} = 1$ and $\mathrm{Re} = 0$ for $\mathrm{Ra} < \mathrm{Ra}_c$. For simplicity of the model, the Chandrasekhar limit $\mathrm{Ra}_{\mathrm{Ch}}$ (1.42) is used for the critical Rayleigh number. To implement this transition it is first assumed that a solution $\mathrm{Nu} - 1 = \mathcal{N}(\mathrm{Ra}, \mathrm{Ha}, \mathrm{Pr})$ of equations (3.15) and (3.16) has been found. The onset can then be imposed by multiplying $\mathcal{N}$ with the crossover function $h(x_c) = 1 - f(x_c)$, where $x_c = \mathrm{Ra}/\mathrm{Ra}_{\mathrm{Ch}} = \mathrm{Ra}/(\pi^2\mathrm{Ha}^2)$. From this new solution $\mathrm{Nu} - 1 = h(x_c)\mathcal{N}$ it follows that $(\mathrm{Nu} - 1) \to 0$ for $\mathrm{Ra} < \mathrm{Ra}_{\mathrm{Ch}}$ and $(\mathrm{Nu} - 1) \to \mathcal{N}$ for $\mathrm{Ra} > \mathrm{Ra}_{\mathrm{Ch}}$. Since $\mathcal{N}$ is actually unknown, the above solution can be rearranged to $(\mathrm{Nu} - 1)/h(x_c) = \mathcal{N}$. This means, that if $\mathrm{Nu} - 1$ is replaced by $(\mathrm{Nu} - 1)/h(x_c)$, it has the same effect as multiplying $\mathcal{N}$ with $h(x_c)$. Applying this replacement to (3.15) and (3.16),

and eliminating Re from both equations gives

$$
\left.\begin{aligned}
\frac{(\mathrm{Nu}-1)\mathrm{Ra}}{\mathrm{Pr}^2\mathcal{R}^2\,h\!\left(\mathrm{Ra}/(\pi^2\mathrm{Ha}^2)\right)} &= c_1\mathcal{R}\,g\!\left(\frac{\mathcal{R}}{\mathrm{Re}^*}\right) + c_2\mathrm{Ha} + c_3\mathrm{Ha}^2 + c_4\mathrm{Ha}^3\,,\\[2em]
\mathcal{R} &= \frac{\left(\sqrt{c_6^2 + 4c_5\dfrac{\mathrm{Nu}-1}{h\!\left(\mathrm{Ra}/(\pi^2\mathrm{Ha}^2)\right)}} - c_6\right)^2}{4c_5^2\mathrm{Pr}\,f\!\left(\dfrac{2\mathrm{Nu}}{\mathrm{Ha}}\right)}\,.
\end{aligned}\right\}
\tag{3.18}
$$

Nu in the argument of f has not been modified. Near onset, Ha is generally large and Nu is small. Thus, f is in the limit of small arguments and does not change much from the value $f(0) = 1$.

The final model equations are now given by (3.17) and (3.18). If the model parameters Re^*, and $c_1,\ldots,c_6$ are known, (3.18) can be used to numerically calculate Nu for given values of Ra, Ha and Pr. Subsequently, Re is calculated from (3.17) using this value of Nu. The model is valid for Rayleigh numbers $\mathrm{Ra} \gtrsim 2\times10^5$ and high Hartmann numbers $\mathrm{Ha} \gg 1$ for the assumption of the Chandrasekhar limit and Hartmann layers to hold. Also, once values of $\mathrm{Re} \gtrsim 1/\mathrm{Pm} \sim 10^6$ are reached, the model is no longer applicable: The magnetic Reynolds numbers would be $\mathrm{Rm} \gtrsim 1$, which violates the quasistatic approximation.

The crossover function h is not introduced in (3.17), because $\mathrm{Re} = 0$ is the intrinsic result of that equation for $\mathrm{Nu} = 1$. This means, that once the onset of convection is incorporated into the calculation of Nu, it is applied to Re automatically.

3.1.2. Fitting of the model parameters

The model parameters are *a priori* unknown and have to be determined by fitting the model to experimental or numerical data. Given a set of values $(\mathrm{Nu}, \mathrm{Ra}, \mathrm{Ha}, \mathrm{Pr})$, the model parameters c_1 to c_6, and Re^* can be determined by fitting (3.18) to the dataset. Using these parameter values, (3.18) is now numerically solvable to determine $\mathrm{Nu}(\mathrm{Ra}, \mathrm{Ha}, \mathrm{Pr})$. The Reynolds number could also be evaluated from (3.17) using the fit values of c_5, c_6 and the result for Nu. However, it is important to realise that the fit equation (3.18) is invariant under the following transformations

$$
\begin{aligned}
\mathrm{Re}^* &\to \beta\mathrm{Re}^*, & c_1 &\to \beta^{-3}c_1\,, & c_2 &\to \beta^{-2}c_2\,, & c_3 &\to \beta^{-2}c_3\,,\\
& & c_4 &\to \beta^{-2}c_4\,, & c_5 &\to \beta^{-1}c_5\,, & c_6 &\to \beta^{-1/2}c_6\,,
\end{aligned}
\tag{3.19}
$$

for any $\beta \in \mathbb{R}$. This means, that when (3.18) is fitted to a set of data, the resulting parameters are not uniquely defined. While the Nusselt number is completely unaffected by this, the Reynolds number in (3.17) is rescaled by $\mathrm{Re} \to \beta\mathrm{Re}$.

To resolve this ambiguity of the model, at least one data point $(\mathrm{Re}_\beta, \mathrm{Nu}_\beta, \mathrm{Ra}_\beta, \mathrm{Ha}_\beta, \mathrm{Pr}_\beta)$ including the Reynolds number has to be known. The parameter values resulting from the first fit are then used to calculate $\mathrm{Re}(\mathrm{Ra}_\beta, \mathrm{Ha}_\beta, \mathrm{Pr}_\beta, \mathrm{Nu}_\beta)$ from (3.17). The factor β is then determined

	Reference	Ra_{min}	Ra_{max}	Ha_{min}	Ha_{max}	Pr	Γ
E	Cioni et al. [71]	2×10^7	3×10^9	850	1980	0.025	$1 : 1$
E	Aurnou and Olson [72]	4×10^2	7×10^4	26	35	0.025	$8.3 : 8.3 : 1$
E	Burr and Müller [73]	3×10^3	1×10^5	10	120	0.020	$10 : 20 : 1$
E	King and Aurnou [74]	2×10^6	2×10^8	0	1110	0.024	$1 : 1$
S	Liu et al. [75]	10^7	10^7	0	2000	0.025	$4 : 4 : 1$
S	Yan et al. [76]	2×10^7	1.7×10^8	1414	1414	0.025	various
		1×10^4	8×10^{10}	0	10 000	1	various
S	Lim et al. [77]	5×10^5	1×10^{10}	0	800	8	$1 : 1 : 1$

Table 3.1.: Experiments (E) and simulations (S) on Rayleigh-Bénard convection in a vertical magnetic field. Listed are the minima and maxima of Ra and Ha, as well as the Prandtl number Pr of the working fluid. The cell aspect ratio Γ is given as *diameter* : *height* for cylindrical cells and as *width* : *depth* : *height* for rectangular cells. The simulations by Lim et al. [77] were conducted in rectangular cells of various aspect ratios ranging from 0.76 : 0.76 : 1 to 28.3 : 28.3 : 1.

as the ratio of the real vs. the calculated Reynolds number

$$\beta = \frac{\mathrm{Re}_\beta}{\mathrm{Re}(\mathrm{Ra}_\beta, \mathrm{Ha}_\beta, \mathrm{Pr}_\beta, \mathrm{Nu}_\beta)} \tag{3.20}$$

Using this value of β, the model parameters are rescaled according to (3.19). The resulting values for c_1 to c_6, and Re^* are the final model parameters and can be used to correctly calculate $\mathrm{Nu}(\mathrm{Ra}, \mathrm{Ha}, \mathrm{Pr})$ and $\mathrm{Re}(\mathrm{Ra}, \mathrm{Ha}, \mathrm{Pr})$ from equations (3.18) and (3.17).

3.2. Initial theoretical results

This section aims to illustrate the first results of the model, which were published in 2016 [Z1]. Since then, a number of new publications have been released, reporting data on magnetoconvection. These will be considered later on in section 5.4, together with the experimental data of the present thesis.

Only very few experiments have been conducted for Rayleigh-Bénard convection in a vertical magnetic field. Four relevant publications are listed in table 3.1. Two of these experiments, namely by Cioni et al. [71] and by King and Aurnou [74], were conducted at high $\mathrm{Ha} > 100$ within the convective regime. In this section, the data by Cioni et al. [71] will be used to evaluate the free parameters of the theoretical model.

None of the experimental publications report Reynolds numbers of the flow, which are essential to fix the ambiguity of the theoretical model. In absence of experimental data, the results of simulations have to be used instead. Most numerical studies focus on the onset of convection at low Rayleigh and Hartmann number. Until recently, the only available direct numerical simulations at high Ra, low Pr and $\mathrm{Ha} > 100$ were by Liu et al. [75] (see table 3.1). Two other simulations at higher Prandtl number have since been published. Lim et al. [77] used a Prandtl
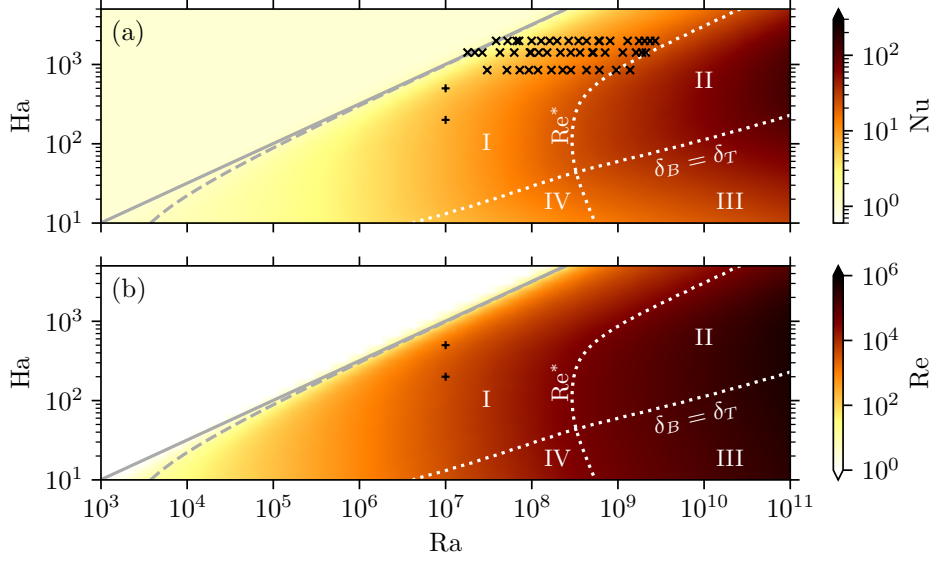
Figure 3.1.: Results of the theoretical model for parameters (3.21) and $Pr = 0.025$. (a) Nusselt number. (b) Reynolds number. Both diagrams show the Chandrasekhar limit Ha_{Ch} (solid line) used in the model and for comparison the real solution for the onset of convection Ha_c (dashed line). The dotted lines mark the regime transitions of the BL nesting ($\delta_B = \delta_T$) and the transition to full turbulence ($Re = Re^*$), dividing the parameter space into four regimes I to IV (see text for details). The data used for fitting the model are marked by crosses (experiments by Cioni et al. [71]) and plusses (simulations by Liu et al. [75]).

number of $Pr = 8$. Yan et al. [76] mainly simulated at $Pr = 1$, but also show some data at $Pr = 0.025$ which would be of interest for this theory. The Reynolds number in these simulations is defined with the rms-average of the velocity magnitude over the whole fluid volume. Here, the numerical data by Liu et al. [75] for $Ha = 200$ and 500 (equivalent to the range $0 < Ha < Ha_c$) is used to evaluate (3.20).

Using the experimental data by Cioni et al. [71] and numerical data by Liu et al. [75], the model parameters are determined to be

$$Re^* = 3.8 \times 10^4 \,, \quad c_1 = 0.17 \,, \qquad\qquad c_2 = -5.3 \,, \qquad c_3 = 0.030 \,,$$
$$c_4 = -5.9 \times 10^{-7} \,, \quad c_5 = 5.6 \times 10^{-3} \,, \quad c_6 = 0.58 \,. \tag{3.21}$$

These parameters can now be used to numerically calculate the Nusselt number from (3.18) for given values (Ra, Ha, Pr). Afterwards, the corresponding Reynolds number results from (3.17).

A colour plot of Nu and Re over the (Ra, Ha) phase space at $Pr = 0.025$ is shown in figure 3.1. The model correctly reproduces the conductive regime $Nu = 1$ and $Re = 0$ above the Chandrasekhar limit $Ra_{Ch} = \pi^2 Ha^2$ (solid line). Since this critical Rayleigh number is an approximation, the proper numerical solution of the onset of convection is plotted for comparison (dashed line). It shows, that the Chandrasekhar limit Ha_{Ch} is a good approximation for $Ra > 2 \times 10^5$, but deviates from the real solution Ha_c for lower Rayleigh numbers. The
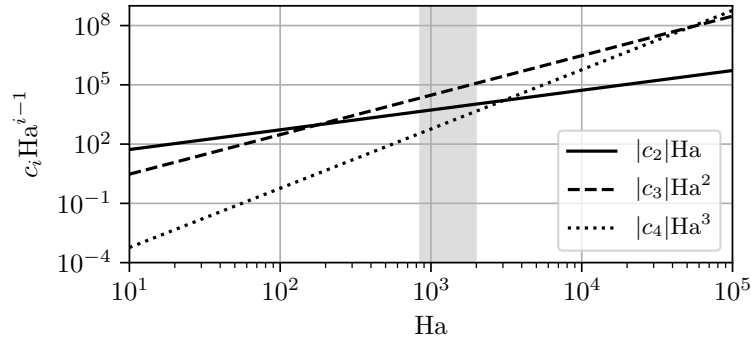
Figure 3.2.: Comparison of the Ha-dependent terms in (3.15). The parameter values c_i are taken from (3.21). The light grey area marks the range of Ha in the experiments by Cioni et al. [71] used for fitting the parameters.

convective regime is divided into four sub-regimes I to IV by the crossover functions introduced in the model. The dotted line $\delta_B = \delta_T$ divides the plot in a regime $\delta_B < \delta_T$ (I and II) and $\delta_B > \delta_T$ (III and IV). The dotted line Re^* marks the transition range from a laminar or non-linear flow (I and IV) to fully turbulent convection (II and III).

The main issue of this initial result is the limited phase space that is covered by the data used to fit the model parameter (crosses and pluses in figure 3.1). They are mainly situated in regime I at high Ha and only a couple of measurements cross the $\mathrm{Re} = \mathrm{Re}^*$ line into regime II. Ideally, the data would cover all regimes. As such, these initial regime boundaries should not be considered as accurate predictions since they are extrapolated from a rather small area in the $(\mathrm{Ra}, \mathrm{Ha}, \mathrm{Pr})$ phase space.

This uncertainty also translates towards the fit parameters (3.21). The values of the c_i factors vary widely in their magnitude. c_2 and c_4 even have a negative value, which is not physically sensible, since they describe positive dissipation rates. The relative fit errors are large for all parameters (close to or even exceeding $100\,\%$). The reason can be illustrated best by considering parameters c_2, c_3, and c_4. Equation 3.15 shows, that the terms containing these parameters scale with different powers of Ha: $c_2\mathrm{Ha}$, $c_3\mathrm{Ha}^2$, and $c_4\mathrm{Ha}^3$. Figure 3.2 shows the magnitude of these three terms. In the range of Ha covered in the experiments by Cioni et al. [71] (light grey area), the quadratic term of c_3 is dominant. This means, that the parameters c_2 and c_4 do not influence the fit result substantially. To get reliable fit values, data in the ranges of Ha, where each of the parameters is dominant, are required. According to the results in figure 3.2, data for Nu at $\mathrm{Ha} \lesssim 10^2$ and $\mathrm{Ha} \gtrsim 5 \times 10^4$ is needed to properly fix c_2 and c_4, respectively. That the model is more insensitive to changes in c_2 and c_4 for the present fitting-data might also be a reason, why both parameters are negative. If large changes in a parameter only result in small variations of the model in the range of the fitting-data, its uncertainty is accordingly high. Thus, more data in a wider range of Ra and Ha would likely improve the fitting procedure and reduce the resulting uncertainty.

This discussion is supposed to present a first look at the results produced by the model. It underlines the importance of the availability of experimental data over a wide range of Ra and Ha for the model to give reasonable results. A more thorough discussion of the results is done

in section 5.4. There, they are compared with the experimental data which is presented in the following chapter.

3.3. Concluding remarks

In this chapter, a model for the heat and momentum transfer in RBC subjected to a vertical magnetic field has been introduced. It is applicable for small Prandtl numbers $\mathrm{Pr} \ll 1$ and, for the quasistatic approximation to be satisfied, requires small magnetic Reynolds numbers $\mathrm{Rm} \ll 1$. Over the $(\mathrm{Ra}, \mathrm{Ha})$ phase space it is valid for $\mathrm{Ra} \gtrsim 2 \times 10^5$ and for $\mathrm{Ha} \gg 1$ to ensure that the Chandrasekhar limit $\mathrm{Ra_{Ch}}$ can be applied and that the viscous BL is a Hartmann layer, respectively. The model parameters were successfully determined from experimental and numerical data. The initial results of the model are shown to illustrate the fitting procedure and to demonstrate that the model reproduces the general features of heat and momentum transfer in magnetoconvection.

The following two chapters chapter 4 and chapter 5 will present new experiments on liquid metal RBC without and with a vertical magnetic field. Using the insights gained from these experiments, the model is revisited in section 5.4. The new data are used in section 5.4.1 to conduct a thorough comparison of the theoretical and experimental results. The conclusions drawn from this comparison will be used to revise the above model equations and fitting procedure. The revised model is then refitted to all currently available experimental data (section 5.4.2), covering a much larger parameter range than the data used in the initial fit. A final review of the model will be given in section 5.4.3, along with an outlook on possible further improvements and extensions of the model.

4. Classical Rayleigh-Bénard convection experiments

This chapter investigates the flow properties of Rayleigh-Bénard convection in liquid metals without the influence of a magnetic field. This is supposed to lay the foundation for the modification of the flow by magnetic fields later in chapter 5. More fundamentally, these experiments are also supposed to find differences and similarities of low and moderate to high Prandtl number convection. Many publications have used water as a working fluid ($Pr \sim 5.4$) to investigate the large-scale flow in $\Gamma = 1$ convection cells utilising optical flow measurement techniques such as PIV. Liquid metals have much more inertia and a higher thermal conductivity than water, which can lead to very different flow structures. Such a case has been recently demonstrated by Vogt et al. [78], who found a deformed large-scale flow in a $\Gamma = 2$ convection cell, which was termed a jump rope vortex.

In the following, the first focus will be on the large-scale flow of the convective turbulence and its dynamical behaviour (section 4.2). Afterwards, global quantities of heat and momentum transport arising from this flow will be characterised in section 4.3. These results are published in [Z3] with some additional considerations on the small scale properties of turbulence in the flow .

4.1. Experimental set-up

The experiments are conducted in a cylindrical convection cell (figure 4.1(a)). Its inner height H and diameter D are 180 mm, giving an aspect ratio of $\Gamma = 1$. The coordinate system is placed at the centre of the cell with z as the vertical axis. Consequently, the upper plate is at $z = +H/2$ and the lower plate at $z = -H/2$. The y- and x-axes span the horizontal plane. In cylindrical coordinates (r, ϕ, z) the side walls are at a radial position of $r = R \equiv D/2 = 90$ mm. The azimuthal coordinate ϕ starts at the x-axis and runs anti-clockwise, when viewed from above ($-z$-direction).

The bottom plate is a solid copper block. It is heated from below by an electrical heating pad made from non-ferromagnetic ceramic. The electrical circuit within the heating pad is arranged in such a way that the magnetic field generated by the current is minimised . The pad is supplied with a DC current by a power supply.

The top plate consists of two parts: The upper part is a copper heat exchanger cooled with water by a thermostat. Two intertwined spiral channels are run through by the cooling water in opposite directions to ensure a homogeneous supply of cooling power and to avoid breaking of the axis symmetry of the system. The lower part is a solid copper plate with holes and cable-channels for two vertical UDV-sensors. Between the two plates a heat conduction paste is applied to ensure a good thermal connection.
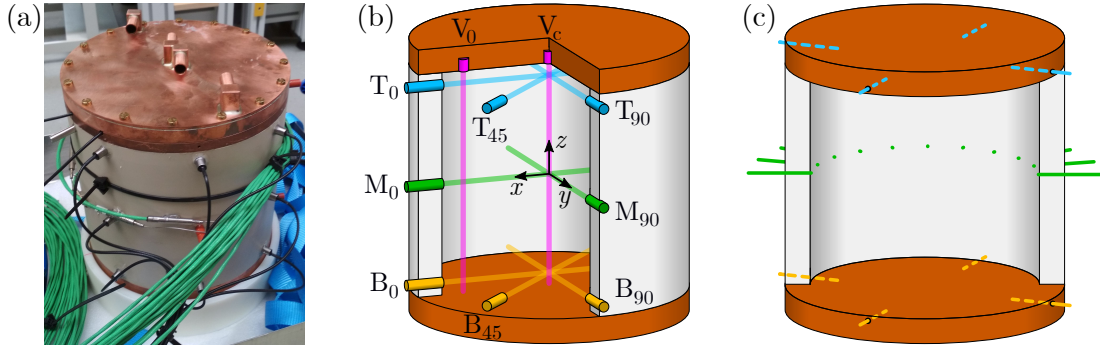
Figure 4.1.: Set-up of the RBC convection cell. (a) Photo of the cell. (b) Positions and labels of the UDV sensors. The label indices refer to the azimuthal position in degree (except for the central sensor V_c). (c) Positions of thermocouples in the cell.

The side walls are made of polyether-ether ketone (PEEK). It is electrically insulating and has a low thermal conductivity of $\lambda_{PEEK} = 0.25\,W\,m^{-1}\,K^{-1}$. The cell sits on a base made of polyamide with a thermal conductivity of $0.23\,W\,m^{-1}\,K^{-1}$. The whole set-up is thermally insulated using insulation wool.

Ten UDV probes are used to investigate the convective flow (figure 4.1(b)). All sensors use an emitting frequency of 8 MHz and are in direct contact with the melt. They have an outer diameter of 8 mm and their piezo-crystal, which generates and measures the ultrasonic signals, has a diameter of 5 mm. The radial velocity component is measured at three heights of the cell: 10 mm below the top plate, at mid-height and 10 mm above the bottom plate. At each layer near the plates, three transducers are placed at the azimuthal positions $\phi = 0°$, 45° and 90°. At mid height, two sensors are positioned at $\phi = 0°$ and 90°. The sensors at 0° and 90° measure the x- and y-components of the velocity, respectively, across the diameter of the cell. In addition to these eight radial sensors, potential measurement positions at $\phi = 45°$ for the mid-height layer and at $\phi = 135°$ for all three layers are prepared, but not used in the present study. The vertical velocity component is measured at two positions in the cell. The first sensor is placed at the centre of the top plate ($r = 0$) measuring along the symmetry axis of the cell. The second sensor is positioned closer to the side-wall at $r = 0.8R = 72\,mm$ and $\phi = 0°$. At the crossing points of the sensor beam-lines two-dimensional and, in case of the centre line, three-dimensional velocity vectors of the flow can be reconstructed.

All UDV sensors are successively scanned through by a multiplexer. The measurement parameters vary depending on the signal quality and the speed of the flow. The sampling time per sensor can vary from 0.2 s to 9 s in extreme cases, but generally stays below 2 s. The velocity is measured at points along each sensor beam-line about 0.25 mm apart. Spatial filters used in the measurement software decrease the effective spatial resolution, ranging from 0.6 mm to 5.5 mm depending on the UDV signal quality.

Temperature measurements are conducted using thermocouples (TC) of type K. 31 TC are multiplexed with a total time resolution of 1.5 s. All TC that are in electrical contact with the liquid metal or the copper plates have their measurement junction electrically insulated from their outer casing to avoid interactions between eddy currents and the thermoelectricity. The TC

positions at the cell are shown in figure 4.1(c). To measure the heating and cooling temperatures, four TC are embedded in each copper plate at 90° intervals. Their tips are placed at a radial position of 75 mm and at a distance of 4 mm from the fluid. The temperature of the top and bottom plate (T_{top} and T_{bot}, respectively) are calculated as the average of the four TC. The temperature difference across the cell is then $\Delta T = T_{\text{bot}} - T_{\text{top}}$. The mean temperature of the fluid $\bar{T} = (T_{\text{top}} + T_{\text{bot}})/2$ was kept at constant 35 °C for all measurements. Only for the highest $\text{Ra} \sim 6 \times 10^7$ did $\bar{T}$ rise to 40 °C due to limited cooling power. This changes the Prandtl number slightly to $\text{Pr} = 0.028$.

Eleven TC are measuring the temperature of the liquid metal near the side wall. They are placed at half-height of the cell and are equally spaced over half the circumference, giving an azimuthal distance of 18° between the sensors. In cylinder coordinates, the first sensor is placed at $\phi = 157.5°$ and the last at $\phi = 337.5° \equiv -22.5°$. Their tips protrude less than 1 mm into the melt.

The cooling water takes in the heat which is transported through the liquid metal and warms up. The cooling power $\dot{Q}_{\text{cool}}$ is thus determined by measuring the in- and outgoing temperatures (T_{in} and T_{out}, respectively) of the cooling water at each of the two in- and outlets of the top copper plate. The heat flux is then

$$\dot{Q}_{\text{cool}} = \tilde{c}_p \tilde{\rho} \dot{V} (T_{\text{out}} - T_{\text{in}}) . \tag{4.1}$$

Here, $\tilde{c}_p$ and $\tilde{\rho}$ are the heat capacity and the mass density of water [79]. The volume flux $\dot{V}$ of the cooling water is measured by a turbine flux-meter. Since the heat flux becomes very small for low Ra or high Ha, the temperature difference $T_{\text{out}} - T_{\text{in}}$ may fall below the measurement accuracy of the TC, which is $\lesssim 0.1$ K. Thus, only measurements where the water temperature difference is larger than 0.2 K are considered in the calculation of $\dot{Q}_{\text{cool}}$.

To estimate the heat loss through the side walls, the radial temperature gradient $\partial_r T$ is measured at mid-height and three azimuthal positions $\phi = 67.5°$, 187.5° and 307.5°. The vertical position is chosen as representative for the whole side wall and the three positions around the circumference are to negate biases due temperature variations induced by the large scale flow. At each position, two TC record the temperature in the side-wall at a distance of 5 mm and 15 mm from the fluid. The radial temperature gradient is the difference between the outer and inner temperature, divided by their radial separation of 10 mm. The average of all three values gives $\partial_r T$. The resulting heat flux is then

$$\dot{Q}_{\text{loss}} = -\lambda_{\text{PEEK}} \pi D H \partial_r T , \tag{4.2}$$

with $\pi D H$ being the surface area of the inner side-wall. Ideally, this heat loss would be the difference between the heating power $\dot{Q}_{\text{heat}}$ input at the bottom and the cooling power at the top of the cell $\dot{Q}_{\text{loss}} = \dot{Q}_{\text{heat}} - \dot{Q}_{\text{cool}}$. The average heat flux $\dot{Q} = (\dot{Q}_{\text{heat}} + \dot{Q}_{\text{cool}})/2$ through the fluid, can then be calculated using

$$\dot{Q} = \dot{Q}_{\text{cool}} + \frac{\dot{Q}_{\text{loss}}}{2} . \tag{4.3}$$

During an experiment, the heating and cooling power are set using PID-controller algorithms to keep the given temperatures T_{top} and T_{bot} at the respective plates constant. At the beginning of

an experiment both temperatures are set to an average temperature of 35 °C, giving a temperature difference of $\Delta T \sim 0$ K. After the flow has settled, the top and bottom temperatures are set to their respective target values. Once the temperatures are reached and the temperature and velocity measurement have settled, the measurement is started. Every measurement is run for at least one hour with the longest measurements being up to ten hours. Once the measurement is finished, the process is repeated to target a different temperature difference.

The results of these measurements are discussed in the following sections.

4.2. Large-scale flow

Water experiments have consistently shown, that turbulent convection in a $\Gamma = 1$ cell organises in a single convection roll, spanning the whole fluid volume [80–85]. This so called large-scale circulation (LSC) is characterised by one up- and one downwelling flow localised near the side walls. These vertical flows transport hot (cold) fluid from the bottom (top) to the top (bottom) of the cell. To close the convection roll, they are connected by horizontal flows near the plate. It is expected that the flows at the plates are, on average, antiparallel to each other. This can be validated using the UDV flow measurements.

Below the top plate ($z = 80$ mm), the UDV sensors T_0 and T_{90} measure radial velocity profiles $v_x(x, t)$ at $y = 0$ and $v_y(y, t)$ at $x = 0$, respectively (see figure 4.2). At the crossing point $(x, y) = (0, 0)$ of these profiles a two-dimensional horizontal velocity vector $\boldsymbol{v}_{\text{top}}$ can be reconstructed. The components of this vector are calculated by averaging the UDV velocity profiles over a central interval of length $D/4$. This gives $\boldsymbol{v}_{\text{top}}(t) = (\bar{v}_x(t), \bar{v}_y(t))$ with

$$\bar{v}_x(t) = \left\langle v_x(x, t) \right\rangle_{-R/4 < x < R/4} , \tag{4.4}$$

$$\bar{v}_y(t) = \left\langle v_y(y, t) \right\rangle_{-R/4 < y < R/4} . \tag{4.5}$$

Here, $\langle \cdot \rangle_x$ denotes the average over the coordinate x and the specified interval. The LSC orientation in the centre of the top plate can now be given as

$$\theta_{\text{top}}(t) = \arctan\left(\frac{\bar{v}_y(t)}{\bar{v}_x(t)}\right) . \tag{4.6}$$

The equivalent flow vector $\boldsymbol{v}_{\text{bot}}$ and the LSC orientation θ_{bot} near the bottom plate are calculated in the same manner using the measurement data from UDV sensors B_0 and B_{90}.

Figure 4.3(a) shows the time series of $\theta_{\text{top}} + 180°$ and θ_{bot} for an experiment at $\mathrm{Ra} = 6 \times 10^7$. The time is shown in free-fall time units τ_{ff} (see (1.4)). Both lines follow each other during the whole experiment, which confirms the expected anti-parallel flow directions of a single coherent convection roll in the cell. A closer look at the time series (figure 4.3(f) and 4.3(h)) reveals that the flow orientations are oscillating around a common mean. The top and bottom orientation angles have the same oscillation period of the order $\tau_{\text{osc}} \sim 10\tau_{\text{ff}}$, but are out of phase to one another. This behaviour is characteristic for the so called torsion mode of the LSC, which was first reported by Funfschilling and Ahlers [86]. Beforehand, the LSC was regarded as a mostly two-dimensional roll in one vertical plane of the convection cell. Oscillations were though to
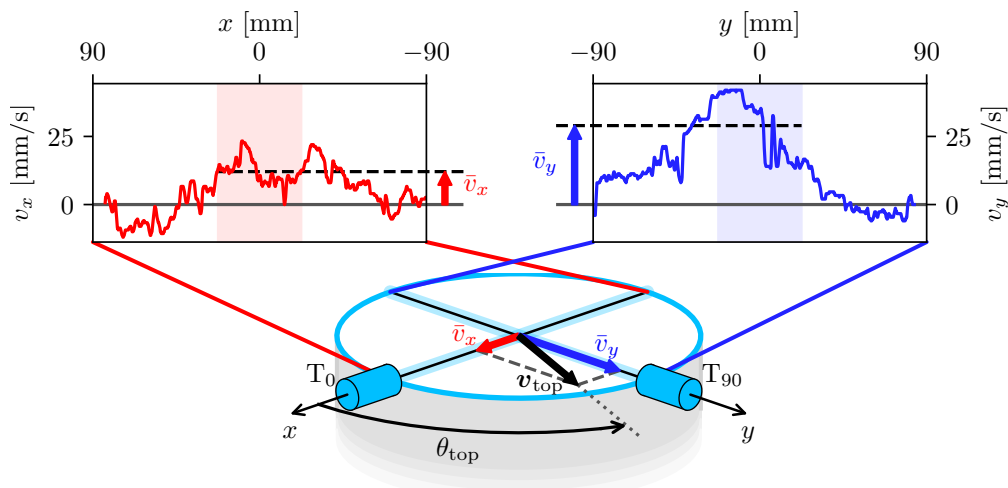
Figure 4.2.: Calculation of the horizontal velocity vector v_{top} and its orientation θ_{top} near the centre of the top plate using the velocity profiles of UDV sensors T_0 (red) and T_{90} (blue). The velocity components $\bar{v}_x$ and $\bar{v}_y$ are averaged over the light red and light blue shaded intervals, respectively.

stem from varying intensities of thermal plume emissions from the plates [80, 81, 87]. It has since been established [84, 86, 88, 89], that the LSC deforms itself periodically by a counter rotation of the top and bottom flow directions termed the twisting or torsion mode (see figure 4.4(a)). This behaviour is confirmed for low-Pr fluids by our results. The frequency of this periodic motion and its dependency on Ra will be investigated in section 4.2.1.

The temperature measurement by the thermocouple array at mid-height of the cell is presented as a colour plot in figure 4.3(b). The time series of each sensor is colour-coded with temperatures above and below the mean fluid temperature $\bar{T}$ in orange and blue, respectively, and arranged by their azimuthal position ϕ. Even with only half of the cell circumference covered, one warm and one cool area can be seen in the plot. These are the imprints of the warm up- and cool down-welling flows of the LSC near the side-walls. To compare their azimuthal position with the previous results near the top and bottom plate, the average LSC orientation $\theta_{\text{LSC}} = (\theta_{\text{top}} + 180° + \theta_{\text{bot}})/2$ is plotted as black dashed line in figure 4.3. The line is additionally smoothed using a running average filter over five consecutive measurements to remove excessive fluctuations due to turbulence. θ_{LSC} perfectly follows the warm imprint (figure 4.3(b)). This confirms the presence of one coherent convection roll covering the whole cell.

Looking, again, at a smaller time scale in figure 4.3(c) and 4.3(e) show periodic oscillations of the warm and cool temperatures. The up- and down-welling flows move along the side wall towards one another, meet at an azimuthal position, and get repelled in opposite directions. The same process then occurs on the other side of the cell and is continually repeated (see figure 4.4(b)). This behaviour at the middle of the cell was first described by Xi et al. [85] and has been termed the sloshing mode of the LSC [84, 88, 90, 91]. This name eludes to the concept, that this temperature pattern could be explained by the transverse displacement of a two-dimensional LSC from a central vertical plane. However, the torsion mode does not fit this
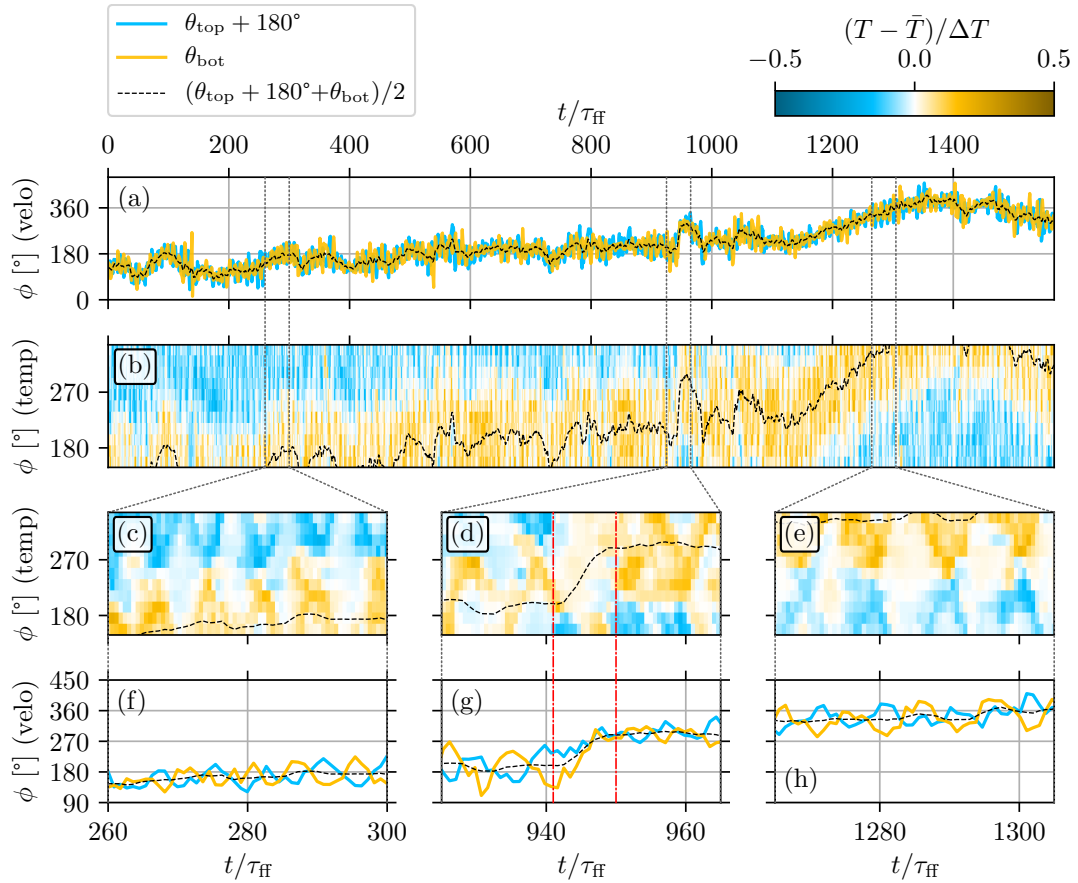
Figure 4.3.: Time series of a RBC experiment at $\mathrm{Ra} = 6 \times 10^7$ ($\tau_{\mathrm{ff}} = 2.3\,\mathrm{s}$). (a) Flow orientations at the top and bottom plate measured by the UDV sensors (velo). The dashed black line is a smoothed average of both orientations. (b) Colour plot of the temperature array at mid height (temp). The dashed black line is replotted from (a). (c)–(e) and (f)–(h) are detailed views of (b) and (a), respectively, and cover a time range of $40\tau_{\mathrm{ff}}$, each. The red dash-dotted lines in (d) and (g) indicate the approximate start and end of a potential cessation event.
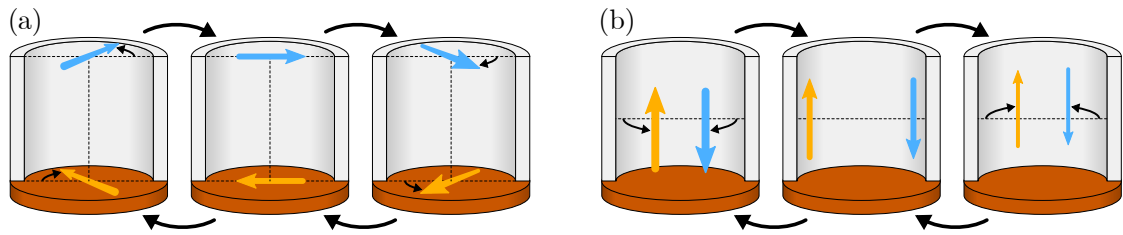
Figure 4.4.: Illustrations of the (a) torsion and (b) sloshing mode of the LSC. Both modes are depicted as three images showing their base state (centre) and the two opposing deflection states (left and right). The black arrows between the states indicate their chronological succession.
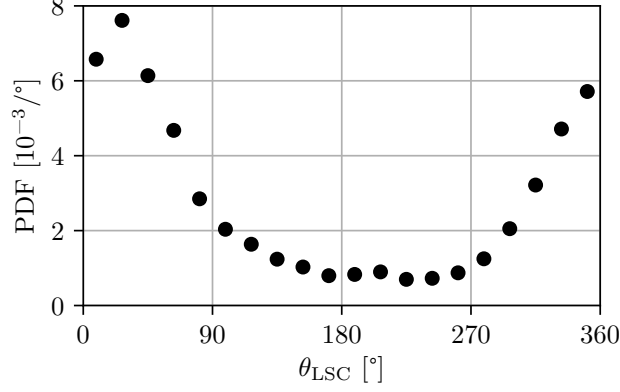
Figure 4.5.: Probability density function of the LSC orientation θ_{LSC} calculated from all RBC measurements $10^6 \leq \text{Ra} \leq 6 \times 10^7$.

idea and implies a three-dimensional structure of the LSC. The exact relation of the sloshing and torsion modes will be investigated later in section 4.2.2.

Superimposed on these short-term oscillations of the order $\sim 10\tau_{\text{ff}}$ is the drift of the mean LSC orientation θ_{LSC} (black dotted line in figure 4.3). The LSC changes its orientation intermittently, sometimes staying at a similar position over multiple hundreds of free fall times and then again rotating continually into one or the other direction for some time. This long-term rotation of the LSC has been shown to be statistically equivalent to a one-dimensional diffusion process of θ_{LSC} [82]. The time scale of this movement can be estimated to scale with the thermal diffusion time $\tau_{\text{drift}} \sim \tau_\kappa = H^2/\kappa$. This estimate can be expressed in free-fall time units via $\tau_\kappa = \sqrt{\text{RaPr}}\tau_{\text{ff}}$. For the present experiments with the values $\text{Pr} = 0.029$ and $10^6 < \text{Ra} < 6 \times 10^7$, this gives $\tau_{\text{drift}} \sim 170$ to $1300\,\tau_{\text{ff}}$.

Due to the axis-symmetry of the system, every value of θ_{LSC} should be equally probable. Figure 4.5 shows the probability density function (PDF) of the LSC orientation calculated from all measurements in the range $10^6 < \text{Ra} < 6 \times 10^7$. A singular peak can be seen at $\theta_{\text{LSC}} \sim 25°$ and a minimum at $\theta_{\text{LSC}} \sim 225°$ that is about one order of magnitude smaller than the maximum. This deviation from a flat PDF indicates, that the set-up is not perfectly levelled. A slight tilt of the cell can break the axis-symmetry and induce a preferred orientation of the LSC [82]. For strong tilting, this can lock the LSC in one orientation, which can be used for easier study of flow properties, since measurement sensors can be aligned with the LSC plane [81, 85]. In the present experiment, θ_{LSC} is not locked, since all orientations are reached at some point during the measurements. This prohibits the exact quantitative statistical investigation of the rotational drift of the LSC in this experiment and only rough qualitative estimates are permissible in that regard. The short-time oscillation and global properties of the convective flow, however, are not significantly affected by this small tilt as has been shown in various experiments [80, 81, 85, 86].

On even longer time scales than τ_{osc} and τ_{drift}, the LSC can experience cessations. An example of such an event is shown in figures 4.3(d) and 4.3(g), indicated by red dash-dotted lines. The distinct temperature imprints by the up- and down-flows in figure 4.3(d) suddenly vanish and only the average fluid temperature $\bar{T}$ is detected. Within less than $10\tau_{\text{ff}}$ the signature of the LSC

reappears at a new orientation with an offset of about 90° to its initial orientation. This suggests a breakdown of the coherent large-scale structure into an incoherent flow state and a subsequent re-establishment of the one-roll structure. This kind of event was studied in detail for long-term water experiments by Brown and Ahlers [82] and Xie et al. [91]. They found that cessations appear at rates of the order of one per day. While the cessation rates for low-Prandtl-number convection will likely be different quantitatively, these results show that measurements have to be run for much longer durations than in the present experiment to collect a statistically sufficient number of cessation events. Consequently, a quantitative analysis is currently not possible.

The properties of the large scale flow presented in figure 4.3 for $\mathrm{Ra} = 6 \times 10^7$ are present for the whole range of Ra investigated in this experiment. This is illustrated in figure 4.6, which shows two additional experimental runs for $\mathrm{Ra} = 10^6$ and 10^7. The top and bottom orientation angles, as well as the temperature profiles confirm the existence of a coherent LSC. The sloshing and torsion mode can be identified in the detailed plots (figure 4.6(c)–(f)). Major differences between the low- and high-Ra cases are changes in the oscillation frequency, which will be covered in detail in the next section, and in the width and strength of the temperature imprint. The temperature maximum and minimum of the vertical flows at the side wall are closer to the values applied to the top and bottom plates for lower Ra. The temperature imprints are also broader than for high Ra, where much of the fluid in between the up- and down-welling flows is close to the average temperature of the cell.

4.2.1. The flow oscillation frequency

This section considers the oscillation frequency $f_{\mathrm{osc}} = 1/\tau_{\mathrm{osc}}$ of the torsion mode and its dependency on the Rayleigh number in detail. Figure 4.7(a) shows the frequency spectra of θ_{top} from the three measurements presented in figures 4.3 and 4.6. Each spectrum shows a peak indicating the oscillation frequency. To extract the values of f_{osc}, the following function is fitted to the spectra

$$A(f) = a \exp\left(-\frac{(f - f_{\mathrm{osc}})^2}{2\Delta f^2}\right) + bf^c . \tag{4.7}$$

This function models the spectrum as an power law background (bf^c) with a Gaussian peak of mean f_{osc} and standard deviation Δf. The fit parameters are a, b, c, f_{osc} and Δf. Examples of this fit are plotted in figure 4.7(a) as dashed lines.

The resulting oscillation frequencies are normalised by the thermal diffusion frequency

$$f_\kappa = \frac{1}{\tau_\kappa} = \frac{\kappa}{H^2} \tag{4.8}$$

and plotted in figure 4.7(b). The error bars correspond to the standard deviation Δf of the Gaussian peak in (4.7). Fitting a power law to the data results in a scaling of

$$f_{\mathrm{osc}}/f_\kappa \simeq (0.10 \pm 0.04)\mathrm{Ra}^{0.40 \pm 0.02} . \tag{4.9}$$

The fit is done via orthogonal distance regression (ODR) and the error estimation of the fit parameters are outlined in appendix C. All following power laws are determined using this
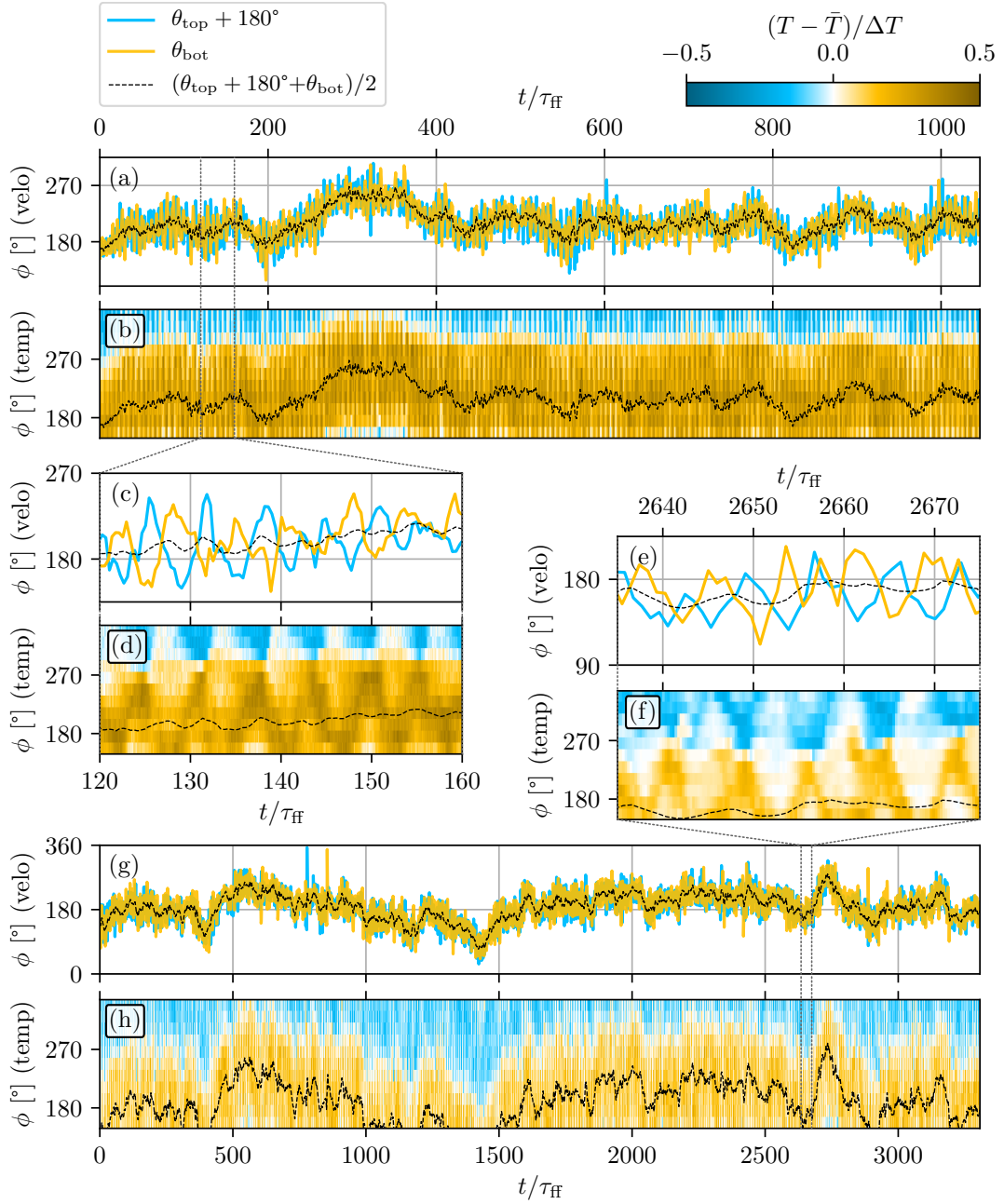
Figure 4.6.: Time series of RBC experiments at $\mathrm{Ra} = 10^6$ ($\tau_{\mathrm{ff}} = 17\,\mathrm{s}$, (a)–(d)) and $\mathrm{Ra} = 10^7$ ($\tau_{\mathrm{ff}} = 5.4\,\mathrm{s}$, (e)–(h)). Quantities and the colour scale are the same as in figure 4.3. (c) and (d) are detailed views of (a) and (b), respectively. (e) and (f) are detailed views of (g) and (h), respectively. The timespan of the detailed views is $40\tau_{\mathrm{ff}}$.
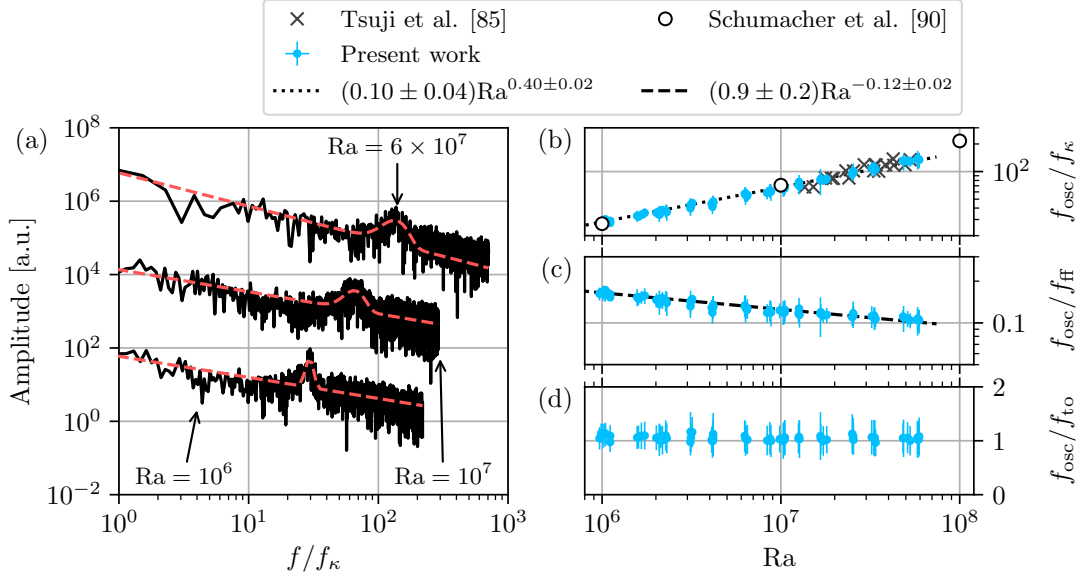
Figure 4.7.: (a) Frequency spectra of θ_{top} from the three measurements in figures 4.3 and 4.6. For better visibility, the spectra for $\text{Ra} = 10^6$ and 6×10^7 are shifted by a factor of 0.01 and 100, respectively. The dotted lines are fits of (4.7) to extract the characteristic oscillation frequency f_{osc}. (b)–(d) Scaling of f_{osc} with Ra when normalised with (b) the thermal diffusion frequency f_κ, (c) the free-fall frequency f_{ff}, or (d) the turnover frequency f_{to}. The frequency error bars result from the standard deviation Δf of the Gaussian peaks fitted in (a)

procedure if not stated otherwise. If the LSC oscillations were to scale with the free-fall time τ_{ff}, a scaling of $f_{\text{osc}} \propto \text{Ra}^{0.5}$ would be expected for constant fluid properties, because the free-fall frequency f_{ff} is given by

$$f_{\text{ff}} = \frac{1}{\tau_{\text{ff}}} = \frac{\sqrt{\nu \kappa \text{Ra}}}{H^2} . \tag{4.10}$$

When normalised by f_{ff}, the oscillations scale as $f_{\text{osc}}/f_{\text{ff}} \simeq (0.9 \pm 0.2)\text{Ra}^{-0.12 \pm 0.02}$ (figure 4.7(c)). This weak dependence on f_{ff} suggests, that the free-fall time is indeed the dominant time scale for the torsion mode of the LSC. The deviation from a pure $f_{\text{osc}} \propto \text{Ra}^{0.5}$ scaling is likely due to the inertial character of the low-Prandtl-number fluid turbulence affecting the momentum transport. The data in figure 4.7(c) are all within the range of $0.1 < f_{\text{osc}}/f_{\text{ff}} < 0.2$ which validates the earlier rough estimate of $\tau_{\text{osc}} \sim 10\tau_{\text{ff}}$.

These results are in agreement with DNS by Schumacher et al. [92] ($\text{Pr} = 0.021$, circles in figure 4.7(b)), who found a scaling of $f_{\text{osc}}/f_\kappa \simeq (0.08 \pm 0.05)\text{Ra}^{0.42 \pm 0.02}$, after correcting their data from radian to units of cycles per diffusive time. Experiments in mercury ($\text{Pr} = 0.024$) by Tsuji et al. [87] also agree very well with our data (crosses in figure 4.7(b)). At a higher aspect ratio of $\Gamma = 2$, Vogt et al. [78] got the same scaling exponent in their liquid gallium experiment ($\text{Pr} = 0.027$) with an overall reduced magnitude: $f_{\text{osc}}/f_\kappa \simeq 0.027\text{Ra}^{0.419 \pm 0.006}$.

Experiments in water (Pr ~ 5.4) generally give a higher scaling exponent and magnitude for f_{osc}/f_κ. Examples for $\Gamma = 1$ cylindrical cells are $f_{\text{osc}}/f_\kappa \simeq 0.2\text{Ra}^{0.46}$ [93], $f_{\text{osc}}/f_\kappa \simeq 0.167\text{Ra}^{0.47}$ [80] and $f_{\text{osc}}/f_\kappa \simeq 0.12\text{Ra}^{0.49}$ [88]. Methanol experiments (Pr $= 6.0$) give similar results as in water: $f_{\text{osc}}/f_\kappa \simeq 0.126\text{Ra}^{0.460\pm0.012}$ [86]. The thermal diffusivity of water is $\kappa = 1.5 \times 10^{-7}\,\text{m}^2\,\text{s}^{-1}$ at $35\,^\circ\text{C}$ [79] compared to $\kappa = 1.1 \times 10^{-5}\,\text{m}^2\,\text{s}^{-1}$ for GaInSn [66]. The absolute oscillation frequencies in GaInSn convection at $\text{Ra} = 10^7$ are thus about 14 times larger than in water, which is a result of the higher inertia of low-Prandtl-number fluids [94–96].

It is known that oscillations in thermal convection correspond to the turnover time of the LSC [84, 87]. In the present experiment, a characteristic speed v_{LSC} of the LSC is calculated as the mean magnitude of the horizontal velocity vectors $\boldsymbol{v}_{\text{top}}$ and $\boldsymbol{v}_{\text{bot}}$ near the plates (see (4.4) and (4.5)), averaged over time

$$v_{\text{LSC}} = \left\langle \frac{|\boldsymbol{v}_{\text{top}}| + |\boldsymbol{v}_{\text{bot}}|}{2} \right\rangle_t . \tag{4.11}$$

The turnover time τ_{to} is then defined as the time a fluid particle with the velocity v_{LSC} takes to travel along a circle of diameter H, and the turnover frequency f_{to} is defined as its inverse

$$\tau_{\text{to}} = \frac{\pi H}{v_{\text{LSC}}} = \frac{1}{f_{\text{to}}} . \tag{4.12}$$

Figure 4.7(d) shows the ratio $f_{\text{osc}}/f_{\text{to}}$ over Ra. For all measurements, the ratio is close to unity, which confirms the scaling of the oscillation period with the LSC turnover time. An alternative definition of f_{to} uses the path along the side-walls and the plates of length $2H + 2D$ instead of an circle inscribed into the cell. This would reduce f_{to} by a constant factor of $\pi/4 \approx 0.79$ but does not affect the $f_{\text{osc}} \propto f_{\text{to}}$ scaling.

4.2.2. Interplay of the torsion and sloshing mode

This section investigates, how the torsion and sloshing modes can be combined into one consistent flow field.

The time-averaged flow orientations $\langle\theta_{\text{top/bot}}\rangle_t$ have an offset of $180°$, as shown before in figures 4.3 and 4.6: $\langle\theta_{\text{bot}}\rangle_t - \langle\theta_{\text{top}}\rangle_t \approx 180°$. The torsion mode then deflects the flow orientation from these average values by an torsion angle $\Delta\theta$: $\theta_{\text{top/bot}} = \langle\theta_{\text{top/bot}}\rangle_t \pm \Delta\theta$. The horizontally flowing fluid near the plates eventually reach the side wall of the cell and are deflected up- or downwards. The azimuthal positions of these vertical flows consequently are the same as the flow orientation at the respective plate, with a time delay accounting for the travel time of the fluid. The azimuthal distance of the up- and down-flow is then

$$\theta_{\text{bot}} - \theta_{\text{top}} \approx 180° - 2\Delta\theta . \tag{4.13}$$

If the torsion angle reaches its maximum, this distance tends to a minimal value, i.e. the up- and down-welling flows approach one another. This is exactly the behaviour seen in the sloshing mode of the temperature imprints at the side-wall. The torsion and sloshing modes are thus a logical continuation of one another, which explains why both modes share the same oscillation frequency.
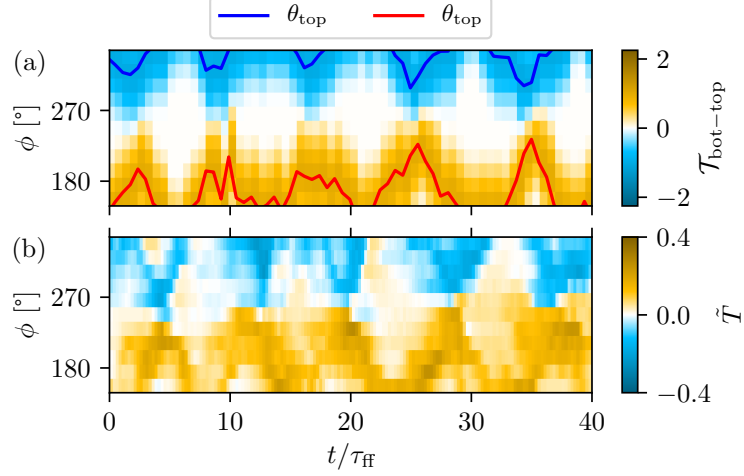
Figure 4.8.: (a) A pseudo-temperature profile $\mathcal{T}_{\text{bot}-\text{top}}(\phi, t) = \mathcal{T}\big(\phi, \theta_{\text{bot}}(t)\big) - \mathcal{T}\big(\phi, \theta_{\text{top}}(t)\big)$. (b) The corresponding real temperature profile $\tilde{T}(\phi, t)$. The measurement is taken at $\text{Ra} = 10^7$ ($\tau_{\text{ff}} = 5.6\,\text{s}$).

To investigate the time delay between the torsion and sloshing modes, the successive correlation of the flow orientations at the top and bottom plate, and temperature imprints of the up- and down-welling flow at the side walls are considered. To separate the signatures of the vertical flows in the temperature field $T(\phi, t)$ at half-height, it is first shifted by the mean fluid temperature $\bar{T}$ and normalised by the temperature difference ΔT across the cell

$$\tilde{T}(\phi, t) = \frac{T(\phi, t) - \bar{T}}{\Delta T}. \tag{4.14}$$

As was displayed in figures 4.3 and 4.6, the cold down-flow is indicated in $\tilde{T}$ by negative values and the hot up-flow by positive values

$$\tilde{T}_{\text{hot}}(\phi, t) = \begin{cases} \tilde{T}(\phi, t) & \text{for } \tilde{T}(\phi, t) \geq 0 \\ 0 & \text{else} \end{cases}, \tag{4.15}$$

$$\tilde{T}_{\text{cold}}(\phi, t) = \begin{cases} \tilde{T}(\phi, t) & \text{for } \tilde{T}(\phi, t) \leq 0 \\ 0 & \text{else} \end{cases}. \tag{4.16}$$

To correlate $\tilde{T}_{\text{hot,cold}}$ with the torsion signature at the "Top" and "Bottom" plate, a pseudo-temperature profile is generated

$$\mathcal{T}(\phi, \theta) = \begin{cases} \cos^2\big(\phi - \theta(t)\big) & \text{for } \theta - 90° < \phi < \theta + 90° \\ 0 & \text{else} \end{cases}. \tag{4.17}$$

This function emulates the temperature profile at half-height if an upwards flow is at the azimuthal position θ. For a downwards flow, $-\mathcal{T}(\phi, \theta)$ is used instead. Figure 4.8 shows an exemplary real
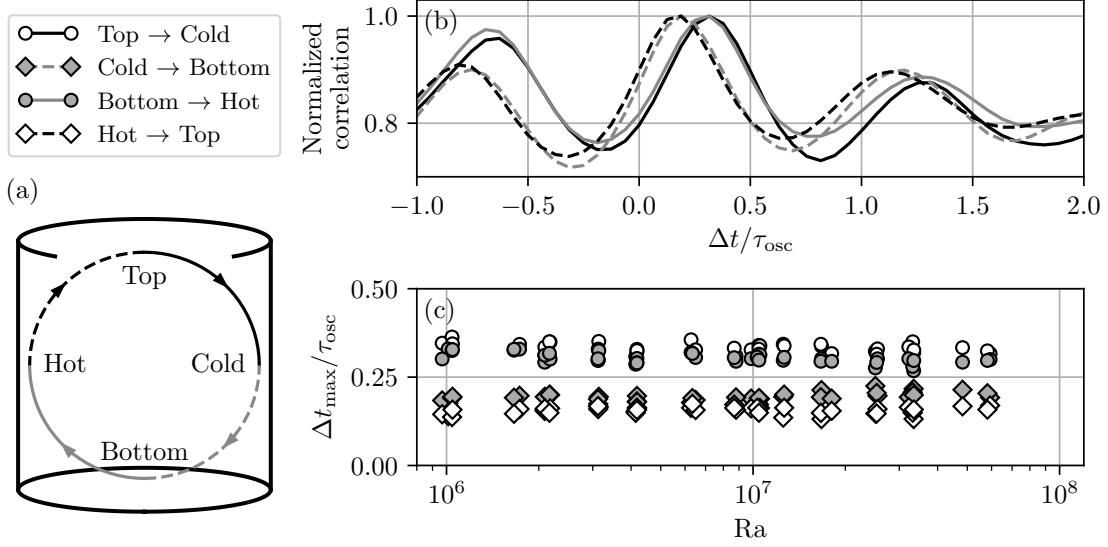
Figure 4.9.: Progression of the flow along the LSC path. (a) Illustration of the correlation combinations. (b) Correlations for the measurement in figure 4.3 at $\mathrm{Ra} = 6 \times 10^7$. (c) Time shifts between the torsion and sloshing signatures over Ra.

temperature profile compared with the pseudo-temperature profile recreated from the top and bottom flow orientations.

The flow progression is from the "Top" plate over the "Cold" down-flow at the side wall to the "Bottom" plate and then via the "Hot" up-flow at the side wall back to the "Top" plate (see figure 4.9(a)). The travel time between these four points can be extracted from the correlations

$$\text{Top} \rightarrow \text{Cold:} \qquad \text{corr}_t\left[-\mathcal{T}\left(\phi, \theta_{\text{top}}(t)\right), \tilde{T}_{\text{cold}}\left(\phi, t\right)\right], \tag{4.18}$$

$$\text{Cold} \rightarrow \text{Bottom:} \qquad \text{corr}_t\left[\tilde{T}_{\text{cold}}\left(\phi, t\right), -\mathcal{T}\left(\phi, \theta_{\text{bot}}(t) + 180°\right)\right], \tag{4.19}$$

$$\text{Bottom} \rightarrow \text{Hot:} \qquad \text{corr}_t\left[\mathcal{T}\left(\phi, \theta_{\text{bot}}(t)\right), \tilde{T}_{\text{hot}}\left(\phi,\right)\right], \tag{4.20}$$

$$\text{Hot} \rightarrow \text{Top:} \qquad \text{corr}_t\left[\tilde{T}_{\text{hot}}\left(\phi, t\right), \mathcal{T}\left(\phi, \theta_{\text{top}}(t) + 180°\right)\right]. \tag{4.21}$$

corr_t refers to a correlation of two functions over the time t and subsequent integration over ϕ. The correlation results for the measurement from figure 4.3 at $\mathrm{Ra} = 6 \times 10^7$ are normalised by their maximum and plotted in figure 4.9(b) over the correlation time shift Δt, normalised by the oscillation period τ_{osc}. All four cases have their maximum correlation at a time shift Δt_{max} near the expected value of $\sim \tau_{\text{osc}}/4$. However, the cases Top $\rightarrow$ Cold and Bottom $\rightarrow$ Hot have a slightly higher value, while for Cold $\rightarrow$ Bottom and Hot $\rightarrow$ Top the time shifts are slightly lower than a quarter oscillation period. This means, that the flow progression from the plates to the side wall at mid-height takes longer than the subsequent progression from the side wall to the opposite plate. In figure 4.9(c), the values of $\Delta t_{\text{max}}/\tau_{\text{osc}}$ are plotted over Ra. The normalised shifts are approximately constant over all measurements, giving average values of $(0.33 \pm 0.01)\tau_{\text{osc}}$ for Top $\rightarrow$ Cold, $(0.19 \pm 0.01)\tau_{\text{osc}}$ for Cold $\rightarrow$ Bottom, $(0.30 \pm 0.01)\tau_{\text{osc}}$ for Bottom $\rightarrow$ Hot,

$(0.16 \pm 0.01)\tau_{\rm osc}$ for Hot $\to$ Top. Adding all time shifts together results in an average value of $(0.98 \pm 0.03)\tau_{\rm osc}$, i.e. the flow takes exactly one oscillation period to progress once around the LSC path. This is the same result as $f_{\rm osc} \approx f_{\rm to}$ which was presented in figure 4.7(d).

While not discussed explicitly, Qiu et al. [80] conducted a similar analysis for their measurements in water. They correlated velocity fluctuations near the centre of the bottom plate with temperature signals at the up-welling flow of the LSC, which corresponds to the case Bottom $\to$ Hot. Their resulting time shift between the signals is close to $\tau_{\rm osc}/4$ though an exact value is not discernible from the plots. Other publications concerning themselves with the time shifts between the sloshing and torsion modes can be sorted into three types of analysis:

1. Correlation between the flow orientation at the top and bottom plates, resulting into the characteristic torsion shift of $\tau_{\rm osc}/2$. This type of analysis has been conducted for experiments in methanol at $\mathrm{Pr} = 6.0$ [86], fluorinert FC-77 electronic liquid at $\mathrm{Pr} = 19.4$ [91], and liquid sodium at $\mathrm{Pr} = 0.0094$ [89].
2. Correlation between the hot and cold temperature imprint of the vertical flows, giving the characteristic sloshing shift of $\tau_{\rm osc}/2$. Such data from water experiments at $\mathrm{Pr} \sim 5.3$ can be found in [85, 93].
3. Correlation of the top or bottom flow orientation with the mean LSC orientation at half-height. This results in a phase shift of $\tau_{\rm osc}/4$ shown, for example, in water at $\mathrm{Pr} = 5.3$ [88].

These three cases are consistent with our results. 1. and 2. is the same as adding two consecutive time shifts from figure 4.9. 3. is equivalent to averaging two consecutive time shifts. Both of these analysis steps cancel out the shift deviations from the ideal value of $\tau_{\rm osc}/4$ and recover the reported time shifts of $\tau_{\rm osc}/2$ for 1. and 2., and $\tau_{\rm osc}/4$ for 3.

As stated before, the different time shifts suggest longer travel times of the fluid from the plates to the mid-height side walls than the subsequent progression to the opposite plate. One explanation for this behaviour could be an asymmetric shape of the LSC, causing the fluid to take paths of different length between the four measurement points. Such an asymmetry can be caused by recirculation zones in the corners of the cell, where the vertical flows impinge on the plates (figure 4.10(a)). These so-called corner vortices can be seen in time-averaged velocity fields of the LSC in water experiments [81]. To examine this conjecture, the horizontal velocity profiles along the LSC orientation near the top and bottom plates will be calculated. To accomplish this, a new horizontal axis ξ is introduced, which is aligned with the LSC orientation. The velocity profile $v_\xi(\xi)$ at the top (bottom) plate is calculated as the average of velocity profiles recorded by the UDV sensors T_0, T_{45} and T_{90} (B_0, B_{45} and B_{90}) whenever the flow orientation $\theta_{\rm top}$ ($\theta_{\rm bot}$) is aligned within $\pm 5°$ of a sensor positions. These average profiles are displayed in figure 4.10 for the measurements shown in figures 4.3 and 4.6 at $\mathrm{Ra} = 10^6$, 10^7 and 6×10^7. Near the top plate (figure 4.10(b)), the velocity is predominantly positive, i.e. it flows to the left, and at the bottom plate (figure 4.10(c)) the profile is mainly negative, thus flowing to the right. An inversion of the flow direction is only visible near the left (right) side of the top (bottom) flow profiles, where the flow impinges on the plate. This is the result of the corner vortices, rotating in the opposite direction of the LSC. It should be noted, that missing or noisy data in the profiles near $\xi \sim 90\,\mathrm{mm}$ is a result of a small zone near the UDV sensors, which is inaccessible due to the ringing of the piezo-crystals in the sensors. The size of the corner vortices can be seen to decrease with increasing Rayleigh number. This suggest, that the LSC becomes more symmetric as the thermal driving increases. In turn, the time shifts should systematically approach the value
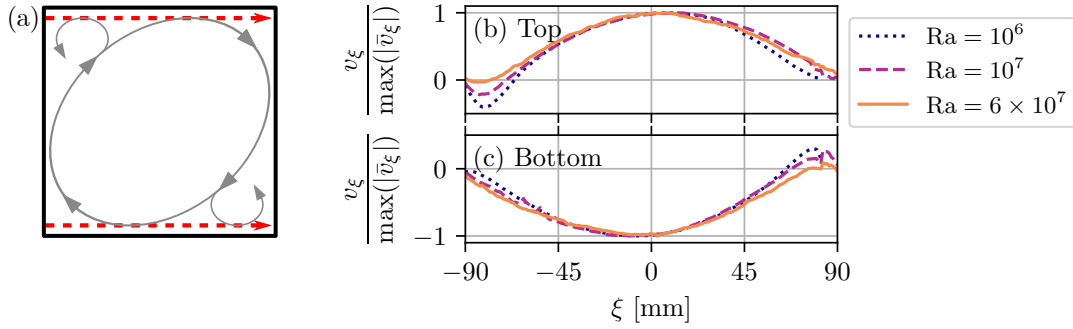
Figure 4.10.: (a) Illustration of the asymmetric LSC shape caused by corner vortices. The red, dashed lines indicate the position of the axes ξ at the top and bottom plate. (b), (c) Average horizontal velocity profiles parallel to the LSC near (b) the top and (c) the bottom plate for different Ra. The profiles are normalised by their maximum value.

of $\tau_{\mathrm{osc}}/4$. Since this is not the case, the shape of the LSC path does not seem to play a significant role in causing the shift deviations.

Another possible reason for the different time shifts are varying velocities along the LSC path. If the fluid is accelerated during its ascend or descend, it would take longer to cover the distance from a plate to the middle plane of the cell, than from the middle plane to the opposite plate. This point, however, has to be left for future studies. It should also be noted, that the above interpretation of the time shifts are based on the assumption that a fluid parcel, that passes by the plates at a certain flow orientation, retains this orientation while crossing the cell. If the flow was to ascend or descend not straight up- or down-wards, but had, on average, an azimuthal velocity component, the above considerations would have to be reviewed.

The above observations allow a deeper understanding of the convective flow in a $\Gamma = 1$ convection cell. The synchronisation of the flow oscillations with the LSC turnover time suggest a large-scale flow composed of independent fluid parcels, each circulating on average in an individual vertical plane. The oscillation modes observed in the experiments could then be the result of phase shifts between the parcels in time and in azimuthal position, giving the impression of the torsion and sloshing motions. This explanation does predict that there are no significant azimuthal velocity components in the flow, which could be used in future experiments to validate the above interpretation.

4.3. Global transport properties

The previous sections considered the structure of the large-scale flow in liquid metal RBC. In this section, the effect of this flow on the global properties of heat and momentum transfer will be investigated.
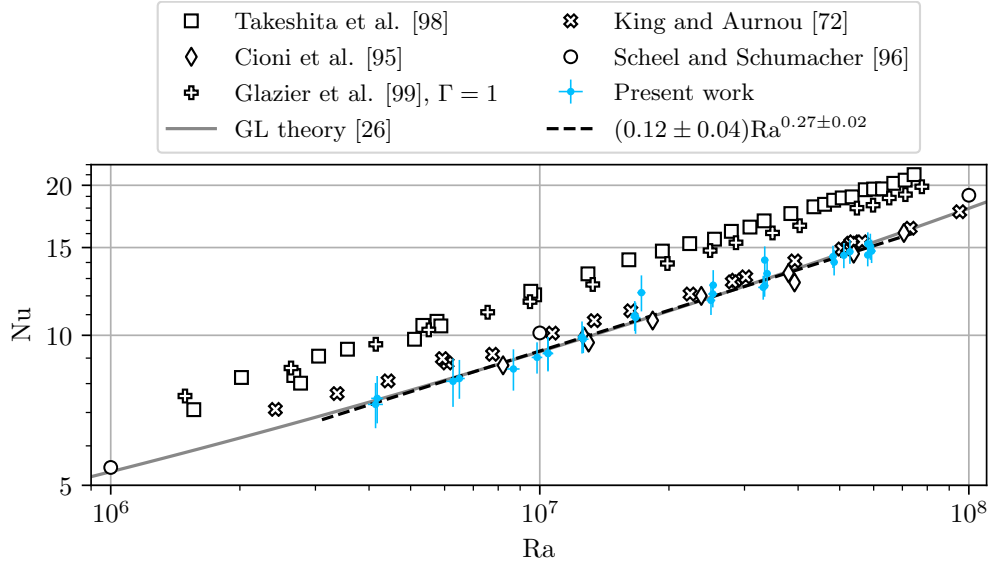
Figure 4.11.: Heat transfer Nu of turbulent liquid metal convection over the thermal driving Ra. The present experimental data is compared to DNS (circles), four experimental results and the GL theory for $\mathrm{Pr} = 0.029$.

4.3.1. Heat transfer

The heat flux transported by the fluid through the cell is characterised by the Nusselt number Nu. In the present experiment it is determined from the cooling power at the top plate (see (1.7), (1.1c) and (4.3)). Figure 4.11 shows the resulting values of Nu over the Rayleigh number Ra. A power law fit to the data gives a scaling of $\mathrm{Nu} \simeq (0.12 \pm 0.04)\mathrm{Ra}^{0.27 \pm 0.02}$.

For comparison, a number of other experimental and numerical results for cylindrical cells with $\Gamma = 1$ are shown in figure 4.11. Experiments by Cioni et al. [97] in mercury ($\mathrm{Pr} = 0.025$) agree excellently with the present data. Numerical simulations by Scheel and Schumacher [98] give the scaling $\mathrm{Nu} \simeq (0.13 \pm 0.04)\mathrm{Ra}^{0.27 \pm 0.01}$, which also is in very good agreement with the present data, deviating only by a small shift in its magnitude. Similar results are also found by King and Aurnou [74, 99] for experiments in liquid gallium at $\mathrm{Pr} \sim 0.025$, though their scaling exponent is somewhat smaller $\mathrm{Nu} \simeq (0.19 \pm 0.01)\mathrm{Ra}^{0.249 \pm 0.004}$. Results of experiments in mercury ($\mathrm{Pr} = 0.024$) by Takeshita et al. [100] give the same scaling exponent, but deviate more strongly in their magnitude towards higher values $\mathrm{Nu} \simeq 0.155\,\mathrm{Ra}^{0.27 \pm 0.02}$. Experiments by Glazier et al. [101] in mercury at $\mathrm{Pr} \sim 0.025$ at $\Gamma = 1$ agree more closely with those by Takeshita et al. [100], but a least-squares power law fit reveals a smaller exponent $\mathrm{Nu} \propto Ra^{0.242 \pm 0.002}$. Glazier et al. [101] also conducted experiments at other aspect ratios $\Gamma = 0.5$ and 2. All their data give a joint scaling of $\mathrm{Nu} \propto \mathrm{Ra}^{0.29 \pm 0.01}$ over a large range of $10^5 < \mathrm{Ra} < 10^{11}$. They attribute the deviation of the values at $\Gamma = 1$ to a strong bulk circulation in the cell.

The Nusselt number predicted by the GL theory [26] is plotted in figure 4.11 as well. It agrees very well with the data of the present experiment and from Cioni et al. [97]. It, however, does not displays a pure power law behaviour. Rather, the scaling exponent is predicted to increase for
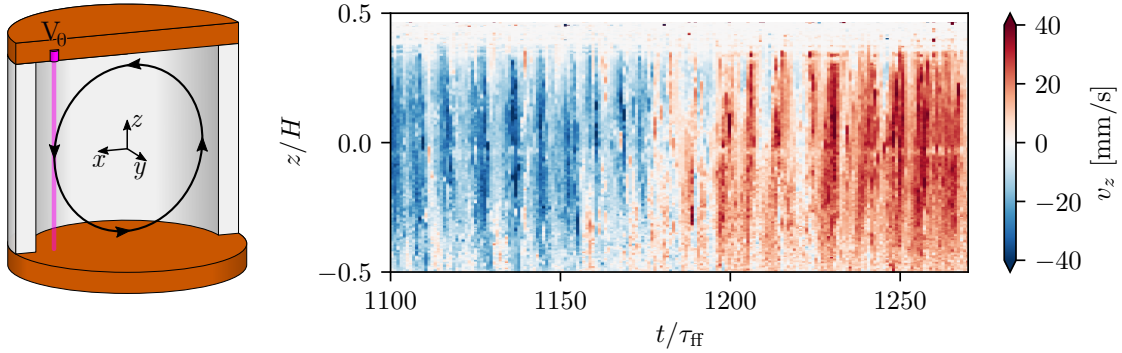
Figure 4.12.: Vertical velocity field $v_z(z,t)$ near the side wall measured by the UDV sensor V_0. The data is taken from the measurement in figure 4.3 ($Ra = 6 \times 10^7$, $\tau_{ff} = 2.3\,s$). The left illustration shows the position of the UDV sensor and the approximate mean orientation of the LSC at the beginning of the time series.

higher Ra. At Rayleigh numbers below 5×10^5, smaller scaling exponents are found: Rossby [19] reported $Nu \simeq 0.147\,Ra^{0.257\pm0.004}$ from experiments in $\Gamma \approx 22$ and 7.4 cells, filled with mercury ($Pr = 0.025$). Liquid sodium experiments at $Pr = 0.006$ and $\Gamma \approx 11$ by Kek and Müller [102] give a scaling of $Nu \simeq 0.20\,Ra^{0.20}$.

4.3.2. Momentum transfer

The momentum transport is quantified by the Reynolds number, which is based on a characteristic velocity of the flow. This velocity, however, is not uniquely defined and can be based on different distinct regions or characteristics of the flow. From the velocity profiles recorded by the ten UDV sensors, three distinct velocities are chosen.

1. The horizontal velocity of the LSC at the plates,
2. the vertical velocity of the LSC at the side walls, and
3. the turbulent velocity fluctuations in the cell centre.

This multitude of different Reynolds number definitions allows an investigation of how sensitive the momentum transfer scaling is to different measurement positions.

The average horizontal velocity v_{LSC} of the LSC near the plates has already been defined in (4.11). The resulting Reynolds number is

$$Re_{LSC} = \frac{v_{LSC}H}{\nu}\,. \tag{4.22}$$

The vertical velocity near the side wall is measured by the UDV sensor V_0 at its radial position of $r/R = 0.8$. A typical velocity field $v_z(z,t)$ measured by the sensor is shown as a colour-plot in figure 4.12. A distinct feature of the flow are regular oscillations of the velocity magnitude over time. These are caused by the sloshing mode of the LSC which regularly wanders in and out of the measurement volume of the sensor. On top of these fluctuations, the slow azimuthal drift of the LSC orientation is visible from the change of the flow direction: First, the down-flow of the LSC (blue) is present at the sensor position. Then, the LSC slowly turns until the upwards-flow

(red) enters the measurement line of the sensor. For the calculation of the vertical LSC velocity, only the strong down- and up-flows are of interest. Here, this characteristic velocity is determined by first calculating the average of the velocity field over time and the central interval of length $H/4$, similarly to how the horizontal velocity vectors at the plates were calculated (see (4.4) and (4.5)). To account for the fluctuations of the velocity due to the sloshing mode, the standard deviation std of the velocity magnitude over time and the same interval are added to the average. The resulting vertical LSC velocity is

$$v_{\mathrm{vert}} = \langle |v_z(z,t)| \rangle_{z,t} + \mathrm{std}_{z,t}(|v_z(z,t)|) \quad \text{over } -H/8 < z < H/8 \,. \tag{4.23}$$

The accompanying Reynolds number is given by

$$\mathrm{Re}_{\mathrm{vert}} = \frac{v_{\mathrm{vert}} H}{\nu} \,. \tag{4.24}$$

In the centre of the cell, the measurement lines of three UDV sensors are crossing one another: M_0, M_{90} and V_{c} measure the velocity profiles $v_x(x,t)$, $v_y(y,t)$ and $v_z(z,t)$, respectively. This allows the calculation of a three-dimensional velocity vector $\boldsymbol{v}_{\mathrm{centre}}$. The vector components are determined by, again, averaging the velocity profiles over the central interval of length $D/4$ or $H/4$, respectively

$$v_{\mathrm{centre},x}(t) = \big\langle v_x(x,t) \big\rangle_{-R/4 < x < R/4} \,, \tag{4.25}$$

$$v_{\mathrm{centre},y}(t) = \big\langle v_y(y,t) \big\rangle_{-R/4 < x < R/4} \,, \tag{4.26}$$

$$v_{\mathrm{centre},z}(t) = \big\langle v_z(z,t) \big\rangle_{-H/8 < x < H/8} \,. \tag{4.27}$$

To determine a characteristic magnitude of the velocity fluctuations, the rms-average of the vector magnitude is calculated

$$v_{\mathrm{centre}} = \sqrt{\big\langle |\boldsymbol{v}_{\mathrm{centre}}(t)|^2 \big\rangle_t} \,. \tag{4.28}$$

This gives a fluctuation Reynolds number

$$\mathrm{Re}_{\mathrm{centre}} = \frac{v_{\mathrm{centre}} H}{\nu} \,. \tag{4.29}$$

The resulting values for $\mathrm{Re}_{\mathrm{LSC}}$, $\mathrm{Re}_{\mathrm{vert}}$ and $\mathrm{Re}_{\mathrm{centre}}$ are displayed in figure 4.13. The two Reynolds numbers based on the LSC velocity give similar results. Power law fits result in scalings of $\mathrm{Re}_{\mathrm{LSC}} \simeq (9.7 \pm 4.4)\mathrm{Ra}^{0.41 \pm 0.03}$ and $\mathrm{Re}_{\mathrm{vert}} \simeq (9.3 \pm 9.5)\mathrm{Ra}^{0.42 \pm 0.04}$. The velocities in the cell centre are somewhat smaller, giving a scaling of $\mathrm{Re}_{\mathrm{centre}} \simeq (2.9 \pm 3.1)\mathrm{Ra}^{0.46 \pm 0.04}$. This shows, that the turbulent fluctuations grow faster, than the overall speed of the large-scale flow. In DNS by Scheel and Schumacher [98], the Reynolds number of the flow was calculated as a rms-average of the velocity magnitude over the whole fluid volume (circles in figure 4.13), giving a scaling of $\mathrm{Re} \simeq (6.5 \pm 0.6)\mathrm{Ra}^{0.45 \pm 0.01}$. These results match $\mathrm{Re}_{\mathrm{LSC}}$ and $\mathrm{Re}_{\mathrm{vert}}$ in magnitude, since the volume average includes the high-speed regions of the LSC. The scaling exponent, however, is more similar to $\mathrm{Re}_{\mathrm{centre}}$.
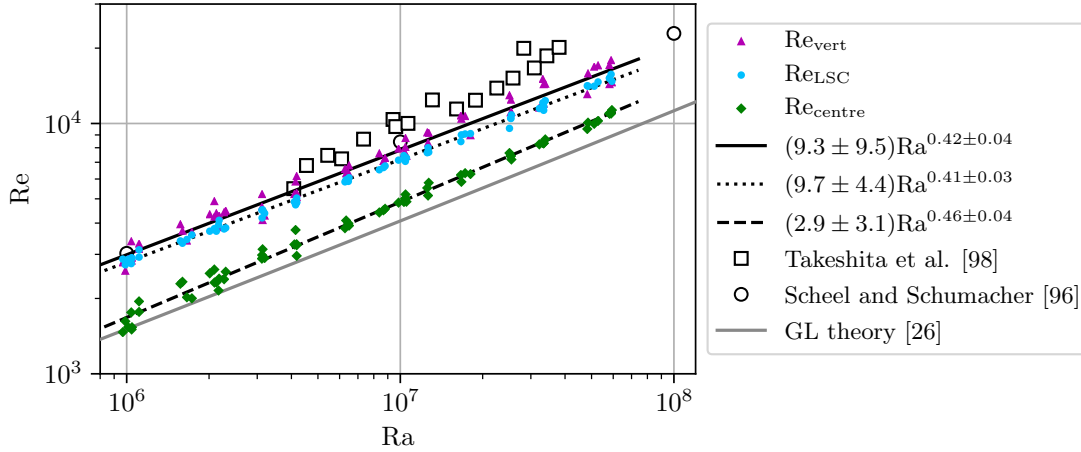
Figure 4.13.: Turbulent momentum transport Re in liquid metal convection over the thermal driving Ra. Uncertainties of the present experimental data are not shown for better visibility. They are about 20 to 30 % due to the turbulent fluctuations. The data is compared to numerical (circles), experimental (squares) and theoretical results (grey line).

Experiments reporting Reynolds numbers in liquid metal convection are rather scarce due to the difficulty of measuring the flow field in an opaque liquid. Takeshita et al. [100] measured the vertical velocity near the side wall using the correlation of two temperature probes at $r/R = 0.8$. The resulting Reynolds number (squares in figure 4.13) is close to Re_{vert} in magnitude but with a stronger scaling exponent $Re \simeq 6.24Ra^{0.46 \pm 0.02}$. In another experiment in liquid gallium and a $\Gamma = 2$ cell, Vogt et al. [78] calculated the Reynolds number from the horizontal velocity at the cell centre. This gave an increased scaling exponent $Re \simeq 5.662Ra^{0.483}$. All these different results underline, that the momentum transport is strongly dependent on the measurement technique, position and calculation procedure used to determine the characteristic velocity from the complex three-dimensional flow structure. This can also be considered to be the reason for Re_{LSC} and Re_{vert} having smaller scaling exponents than other comparable results from experiments or DNS. Interestingly, the scaling exponent of the global Re from the DNS by Scheel and Schumacher [98] is most closely matched by the velocity fluctuations Re_{centre} in the cell centre.

Additionally, the results of the GL theory for $Pr = 0.029$ are shown in figure 4.13. It under-predicts the Reynolds number compared to the LSC-based experimental and numerical values by up to a factor of 2. The scaling exponent of the GL data, however, is within the uncertainty of the present experiments results: A least-squares power law fit to the grey line in figure 4.13 gives $Re \propto Ra^{0.44}$.

4.4. Concluding remarks

This chapter investigated the properties of turbulent liquid metal Rayleigh-Bénard convection in a $\Gamma = 1$ cylindrical cell. It confirmed the presence of a large-scale circulation, well known

from other experiments. The dynamics of the LSC were investigated in depth by identifying the torsion and sloshing modes of the flow at the plates and at half-height, respectively. The frequency of these oscillations and their interplay to form a single coherent flow structure were studied. The amplitude and frequency of the oscillation modes was found to be more intense for liquid metals than in water experiments. The phase shifts between the modes revealed an asymmetry in the flow propagation, not reported in previous studies.

Heat transport measurements gave good agreement with other experiments, numerical simulations and theoretical predictions. A full consensus of all data could not be reached, which suggests a dependence of the Nusselt number on the exact execution of the experiments and the specific nature of the flow state.

The global momentum transport was found to be highly dependent on the chosen characteristic velocity. Depending on the area of the flow which is considered, significant differences in magnitude and scaling can be achieved. Especially for experiments, which generally only probe a limited area of the flow, it is thus important to take this into consideration.

In the following chapter 5, the effect of a vertical magnetic field on the experiment is investigated. The above results are used as the base state of the convective system which is then altered by an increasingly stronger magnetic field.

5. Rayleigh-Bénard magnetoconvection experiments

After the previous chapter characterised the classical Rayleigh-Bénard system, this chapter investigates the modification of the convective flow by a vertical magnetic field. Figure 5.1 gives an overview of the region of the $(\mathrm{Ra}, \mathrm{Ha})$ phase space covered by the experiment. The parameter space of $10^6 \leq \mathrm{Ra} \leq 6 \times 10^7$ from the previous chapter is extended by Hartmann numbers up to $\mathrm{Ha} \sim 1000$. It is known that a vertical magnetic field can suppress three-dimensional turbulent fluctuations and lower the overall flow strength [5, 31]. The present experiments are meant to catalogue the flow regimes occurring with increasingly stronger magnetic fields and how they influence the heat and momentum transport. For Rayleigh numbers of $\mathrm{Ra} \leq 10^7$ the critical Hartmann number $\mathrm{Ha_c}$ can be reached. Recent numerical simulations [75] have shown that due to side wall effects a convective flow can prevail even for $\mathrm{Ha} > \mathrm{Ha_c}$. This is to be verified by the measurements at low Ra and high Ha.

The first section 5.2 of this chapter will give details on the magnet system used to generate the magnetic field. Afterwards, the large-scale flow will be characterised in section 5.2 using temperature and velocity measurements. The behaviour of momentum and heat transfer is considered in section 5.3. Using that knowledge, the GL theory for magnetoconvection is revisited and revised in section 5.4.
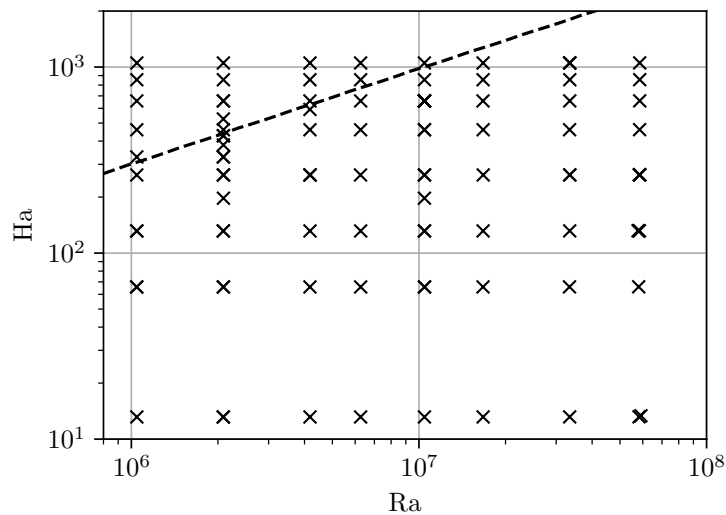

Figure 5.1.: Parameters of the series of the conducted magnetoconvection experiments at $\mathrm{Ha} > 0$. The dashed line indicates the onset of convection for an infinite fluid layer $\mathrm{Ha_c(Ra)}$.
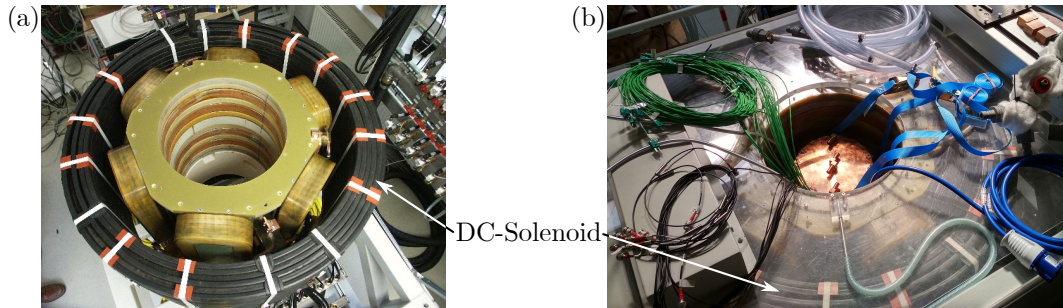
Figure 5.2.: The MULTIMAG facility at the HZDR. (a) Coil arrangement. The outer black
solenoid is used to produce the vertical magnetic field in the central bore. (b) The
convection cell inside the MULTIMAG, without heat insulation or cooling water
supply.

5.1. Experimental set-up

The cell for the magnetoconvection experiments is the same as for the classical Rayleigh-Bénard
experiments of the previous chapter. For more details on the set-up, see section 4.1. The cell
is now placed in a vertical magnetic field which is generated by the MULTIMAG facility [103]
at the Helmholtz-Zentrum Dresden – Rossendorf (HZDR). The outer DC solenoid, shown in
figure 5.2(a), is supplied with a constant current by an external power supply. The magnetic field
strength is measured in the centre of the bore hole and calibrated with respect to the applied
electric current. At a current of 800 A, a maximal magnetic field of 140 mT can be reached. The
cell is then placed in the centre of the bore hole (figure 5.2(b)).

In a measurement, the Rayleigh number is first set like in the $\mathrm{Ha} = 0$ case (section 4.1). Once
the flow has stabilised, the desired magnetic field is switched on. Depending on the field strength,
the heating and cooling power has to be adjusted by the PID-controllers of the heating pad and
the thermostat, respectively. Once the temperatures are constant again and the convective flow
has settled, the measurement data are recorded for at least one hour. The longest measurement
takes ten hours.

5.2. Evolution of the large-scale flow

In the following, the effect of the vertical magnetic field on the large-scale flow structure is
investigated. This section first gives an overview of the general evolution of the flow for
increasing field strength using the side wall temperature profile to identify distinct flow regimes.
These are then studied in detail within their own sub-section.

The large scale flow is monitored by UDV velocity measurements and the thermocouple array
at half height of the cell (see figure 4.1). Figure 5.3 displays the evolution of the side wall
temperature profile for increasing Ha at $\mathrm{Ra} = 2.1 \times 10^6$. The initial temperature profile at
$\mathrm{Ha} = 0$ shows the characteristic sloshing motion of the LSC as discussed in the previous chapter
(section 4.2). When a weak vertical magnetic field is applied, the temperature profile does not
change much. At $\mathrm{Ha} = 66$, the imprint of the vertical flow is broader and more washed out ,
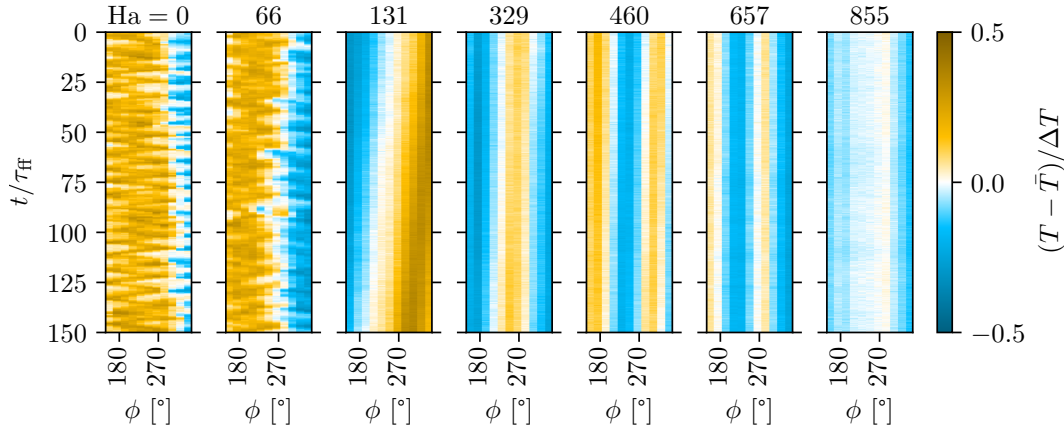
Figure 5.3.: Colour-plots of the side wall temperature profiles at mid-height for different Ha at $\mathrm{Ra} = 2.1 \times 10^6$ ($\tau_{\mathrm{ff}} = 12.1\,\mathrm{s}$). The Hartmann number is given above the respective plot. The onset of convection is $\mathrm{Ha_c} = 443$.

but the sloshing motion of the up- and down flow is still visible. This changes for $\mathrm{Ha} = 131$. While the LSC structure is still present with one up- and one down-flow, the oscillations of the sloshing mode are completely suppressed by the magnetic field. In addition, fluctuations in the temperature magnitude are reduced as well, indicating a decrease in the flow turbulence. The one-roll flow structure of the LSC is a characteristic feature of turbulent convection in cells with aspect ratio close to unity. The suppression of the turbulent character by the vertical magnetic field finally leads to the breakdown of the LSC. The temperature profile at $\mathrm{Ha} = 329$ shows one cold down- and one warm up-flow over half the cell circumference. If the temperature profile was continued over the whole circumference, two up- and two down-flows can be expected to be present near the cell side walls. Such a result is not compatible with the picture of a single convection roll, but suggests the existence of a more complex flow structure consisting of multiple convection rolls or cells, akin to weakly non-linear or laminar convection [11, 104]. This state of the flow continues to exist for increasing magnetic fields. While at $\mathrm{Ha} = 460$ the number of vertical flows does not change, at $\mathrm{Ha} = 657$ one and a half up- and down-flows are visible over half the circumference, suggesting three up- and down-flows along the whole side wall. The clear presence of a convective flow at $\mathrm{Ha} = 460$ and 657 is significant, because the onset of convection for an infinite fluid layer at this Rayleigh number is $\mathrm{Ha_c} = 443$. This shows, that the ideal case of magnetoconvection without side walls is not immediately applicable for a cell with non-conducting side walls. This point will be explored in detail in section 5.2.3. Finally, at one of the highest magnetic fields $\mathrm{Ha} = 855$, no distinct structure is discernible from the temperature measurements. The variations of the colour in figure 5.3 at these Ha is within the measurement accuracy of 0.1 K. This vanishing flow regime is not yet a clear indication of the full suppression of any convective motion in the cell. It is still possible that a flow exists which is simply too weak to produce a detectable temperature imprint at the side walls.

This sequence of temperature profiles gives a clear progression of the flow structure for increasing magnetic field strengths:

1. Turbulent fluctuations and regular oscillations of the torsion and sloshing modes are
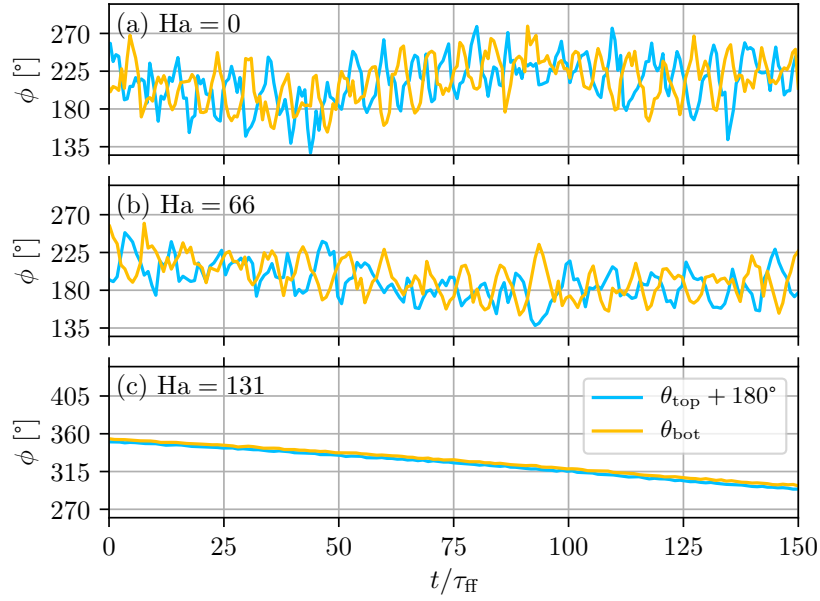
Figure 5.4.: Top and bottom flow orientation θ_{top} and θ_{bot} for low Ha at Ra $= 2.1 \times 10^6$ ($\tau_{\text{ff}} = 1.2\,\text{s}$). All three plots have the same scale. The measurements correspond to the ones shown in figure 5.3 with the same Ha.

suppressed. The specifics of this process are investigated in section 5.2.1

2. Breakdown of the LSC into a complex flow structure consisting of multiple rolls or cells. This type of flow structure is discussed in section 5.2.2.

3. Existence of a flow beyond the classic onset of magnetoconvection in an infinite fluid layer. A deeper analysis is presented in section 5.2.3.

After the different flow regimes are discussed in detail, a regime map is presented in section 5.2.4 along with the investigation of the transition boundaries between the regimes. The flow intensity is expected to continuously decrease with increasing magnetic field strength [5]. This topic is considered briefly in section 5.2.3 and more extensively in section 5.3, which investigates the momentum and heat transport in the flow.

5.2.1. Weak magnetic fields: Modification of the LSC

For small Hartmann numbers, the flow still has an intensity high enough to retain the LSC structure of the Ha = 0 case. This was shown for Ra $= 2.1 \times 10^6$ by the side wall temperature profiles in figure 5.3 for Ha ≤ 131 and is also confirmed by the top and bottom flow orientation $\theta_{\text{top/bot}}$. Figure 5.4 shows $\theta_{\text{top}} + 180°$ and θ_{bot} for the measurements in figure 5.3 at Ra $= 2.1 \times 10^6$ and Hartmann numbers Ha = 0, 66, and 131. In all three cases, the average offset of 180° is retained, i.e. the flows at top and bottom are anti-parallel. The oscillations of the torsion mode, however, are changing significantly. While at Ha = 66 the anti-phase oscillations of θ_{top} and θ_{bot} are still visible, they are completely suppressed at Ha = 131. There, the flow orientations drift in unison with an average offset of $\langle \theta_{\text{top}} - \theta_{\text{bot}} \rangle_t = 176.7° \pm 0.7°$. Together with the stable
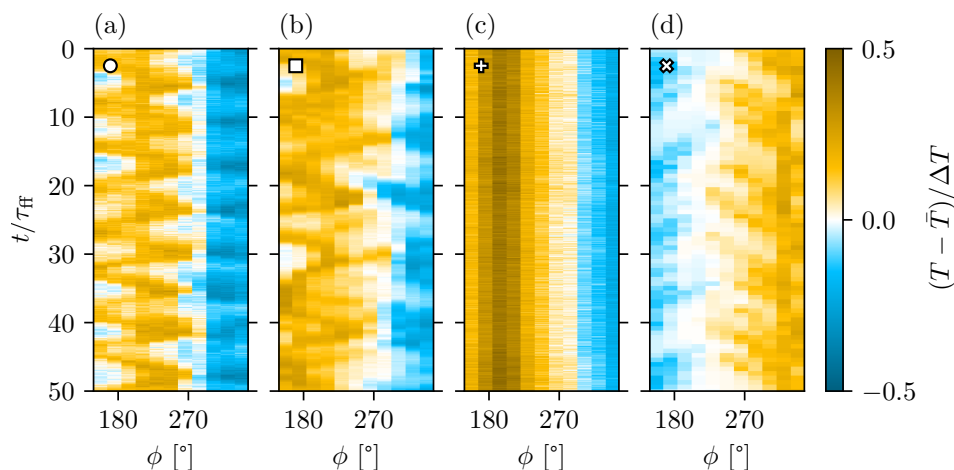
Figure 5.5.: Oscillation patterns of the temperature profile at the side wall. (a) Coherent sloshing ($Ra = 10^6$, $Ha = 13$). (b) Incoherent sloshing ($Ra = 4 \times 10^6$, $Ha = 66$). (c) No oscillation ($Ra = 10^6$, $Ha = 131$). (d) Plume entrainment ($Ra = 6 \times 10^7$, $Ha = 263$). The symbols in the top left corner of each diagram correspond to the markers in figure 5.6 and 5.7.

up- and down-flow from the temperature in figure 5.3 this indicates that the LSC has become quasi-two-dimensional.

The examples shown so far were all recorded at one Rayleigh number. Over the whole range $10^6 \leq Ra \leq 6 \times 10^6$, four different flow patterns can be identified in the LSC regime (figure 5.5). Three patterns have already been introduced above and are repeated only briefly. The first is known from the $Ha = 0$ case and displays a mostly coherent and regular sloshing of the up- and down-welling flows (figure 5.5(a)). The second pattern features an incoherent sloshing and torsion motion at slightly increased magnetic fields (figure 5.5(b)): The back-and-forth motion of the hot and cold temperature imprints become less regular and are more washed out. This regime is not well defined, as there is a continuous transition and the incoherent pattern can appear intermittently within an otherwise coherent sloshing motion. The third pattern is the complete suppression of the regular oscillations of the LSC (figure 5.5(c)). Only small and irregular fluctuations of the temperature are visible, which do not indicate any significant deviation of the flow from the shape of a single convection roll. This regime was only found in experiments for small Rayleigh numbers $Ra \lesssim 3 \times 10^6$. For higher Ra a fourth flow pattern was found instead, which can be seen in figure 5.5(d). While the hot and cold imprints of the LSC are still visible at $\phi \sim 315°$ and $\phi \sim 135°$, respectively, they do not display the typical sloshing motion any more. In the space between the extrema, the temperature is close to the mean value $\bar{T}$. However, ever so often isolated hot or cold spots appear at $\phi \sim 225°$ in between the up- and down-welling flows of the LSC. These temperature imprints indicate thermal plumes which detached from the plates and try to cross the cell at a different position than the ones prescribed by the LSC. Over time the localised hot or cold signals wander towards the up- or down-welling part of the LSC, respectively. This is a first indication of the breakdown of the LSC: Plumes start to detach from the LSC and try to establish new areas of vertical flows, independent of the one-roll structure.
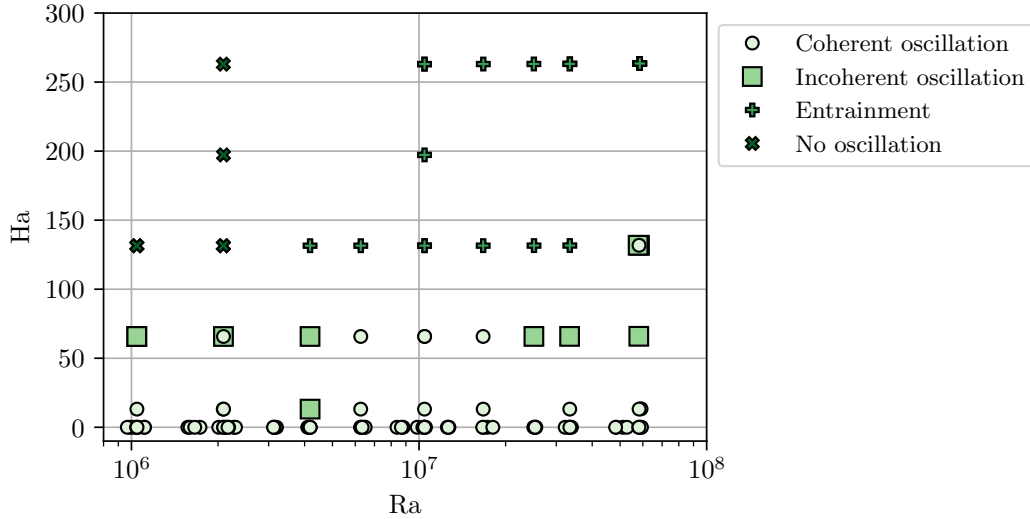
Figure 5.6.: Map of the flow patterns in the LSC regime over the $(\mathrm{Ra}, \mathrm{Ha})$ phase space.

The LSC is, however, still strong enough to persist and after a short time the plumes are again entrained into the main flow. This entrainment regime was not found for $\mathrm{Ra} < 3 \times 10^6$, which can be a sign that the detachment of plumes from the LSC requires a certain strength of the thermal driving. In that case, the LSC pattern without oscillations would essentially be the same as the entrainment pattern, with the difference being that for $\mathrm{Ra} < 3 \times 10^6$ the thermal driving is not strong enough to generate the localised plumes seen in the entrainment pattern. Alternatively, the sampling of the $(\mathrm{Ra}, \mathrm{Ha})$ phase space may have not been dense enough to find both patterns at the respective Rayleigh numbers. Just like for the coherence of the sloshing motion, the transition to the entrainment pattern is not well defined. Similar patterns of the plume entrainment can occasionally be seen in the incoherent oscillation pattern (e.g. at $t/\tau_{\mathrm{ff}} \sim 30$ in figure 5.5(b)).

Figure 5.6 shows all measurements which displayed a dominant LSC structure over the $(\mathrm{Ra}, \mathrm{Ha})$ phase space. The four different patterns are indicated for each measurement by the marker shapes shown in figure 5.5. The coherent and incoherent oscillation patterns are very similar and can coexist for the same parameters. A clearer division appears between the oscillation, entrainment and no oscillation patterns. The sloshing and torsion modes disappear at around $\mathrm{Ha} \sim 100$. Only for the highest $\mathrm{Ra} = 6 \times 10^7$ do the oscillations persist up to $\mathrm{Ha} = 131$. The aforementioned division of the no oscillation and the entrainment patterns is also visible at $\mathrm{Ra} \sim 3 \times 10^6$.

The frequency spectra of θ_{top} at $\mathrm{Ha} = 0$ displayed a peak at the torsion frequency f_{osc} (figure 4.7(a)). When such peaks are present for the $\mathrm{Ha} > 0$ measurements they can be extracted using the same procedure as in section 4.2.1. The results are normalised using the oscillation frequency without magnetic field $f_{\mathrm{osc},0}(\mathrm{Ra}) \equiv f_{\mathrm{osc}}(\mathrm{Ra}, \mathrm{Ha} = 0)$, which is calculated from the scaling (4.9), derived in the previous chapter. Figure 5.7 shows $f_{\mathrm{osc}}/f_{\mathrm{osc},0}$ over the Hartmann number Ha normalised by the critical Hartmann number $\mathrm{Ha_c}$ for the respective Rayleigh numbers Ra. The frequencies of nearly all measurements collapse onto one curve.
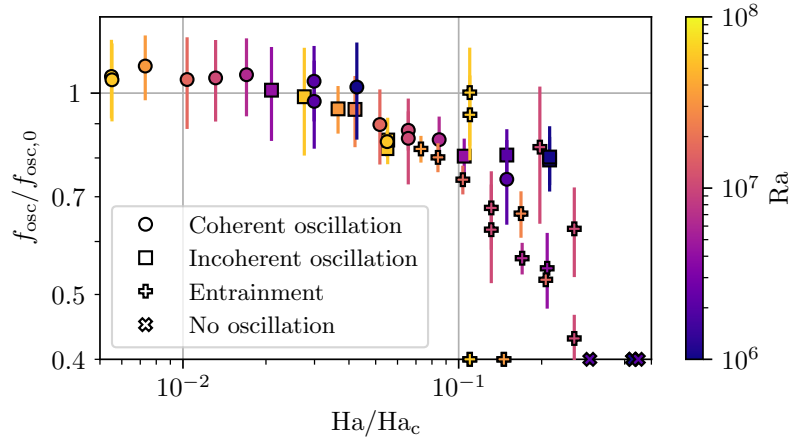
Figure 5.7.: Oscillation frequency f_{osc} of θ_{top} normalised by its value $f_{osc,0}$ at $Ha = 0$. It is plotted over the Hartmann number Ha normalised by the critical Hartmann number Ha_c at the respective Rayleigh number. Points on the bottom abscissa indicate measurements without identifiable frequency peak in their θ_{top} spectrum (i.e. $f_{osc} = 0$). The markers indicate the oscillation pattern of the side wall temperature profile (see figure 5.5).

Up to a Hartmann number of $\mathrm{Ha}/\mathrm{Ha_c} \sim 0.04$ the oscillations are not affected by the magnetic field. After this point, the frequency continually decreases until the oscillations are completely suppressed. Some of the frequencies in the incoherent oscillations and entrainment regime are deviating strongly from this general curve. This shows that the magnetic field disturbs the oscillation patterns of the turbulent flow. Still, it is remarkable that many of the measurements in the entrainment regime continue the trend set by the LSC regime. While the oscillations of the sloshing mode are not visible in the temperature profile, the frequency of the θ_{top} spectra seems to be a remnant of the torsion mode, which might even be related to the appearance of the entrained plumes at mid height. This may be a topic for future investigations.

For the oscillation patterns where the torsion and sloshing modes are still present, the time shifts Δt_{max} between the mode signatures at the plates and the side wall can be calculated analogously to the $\mathrm{Ha} = 0$ case in section 4.2.2. This is not sensible for the entrainment and no oscillation patterns of the LSC, since this analysis assumes the presence of the characteristic motion of the torsion and sloshing modes. Figure 5.8 shows the time shifts Δt_{max} extracted from measurements displaying the coherent and incoherent oscillation patterns. The horizontal lines indicate the average time shift at $\mathrm{Ha} = 0$ from section 4.2.2. It is clearly visible, that the time shifts do not change significantly with respect to the oscillation period $\tau_{osc} = 1/f_{osc}$ for increasing magnetic fields. While the magnetic field decreases f_{osc} as shown in figure 5.7, the flow structure stays the same. The deviation of the shifts from a value $\tau_{osc}/4$ is still present and does not show any clear trend with increasing Ha.

In summary, the LSC regime at weak magnetic fields can be subdivided in two main subregimes:

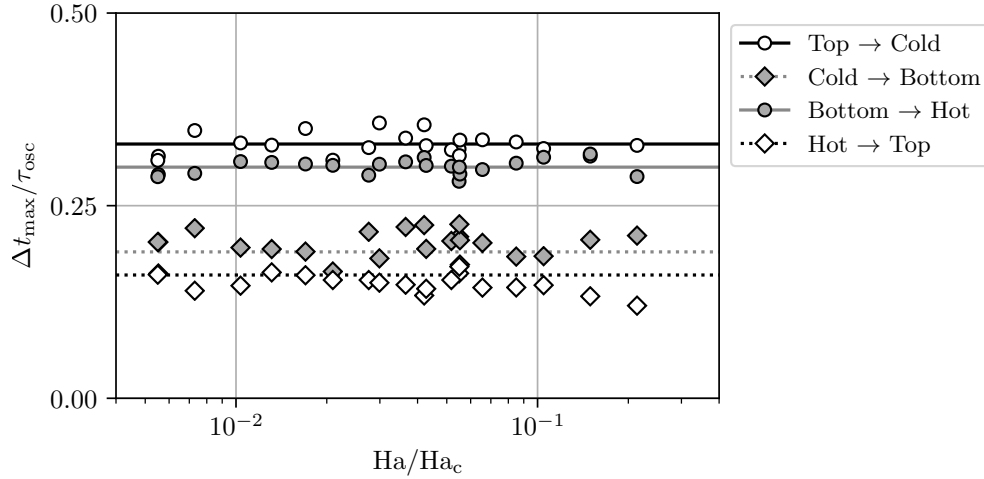1. Sloshing and torsion modes are present. Starting from $\mathrm{Ha} = 0$, the coherent oscillations

Figure 5.8.: Correlation shifts Δt_{max} between the top and bottom plates and the Hot up- and cold down-welling signatures (analogous to figure 4.9) normalised by the oscillation period $\tau_{\text{osc}} = 1/f_{\text{osc}}$ with increasing magnetic field strength $\text{Ha}/\text{Ha}_{\text{c}}$. The horizontal lines indicate the respective average shifts at $\text{Ha} = 0$ (see section 4.2.2). Only measurements displaying coherent or incoherent oscillations are shown.

caused by the turbulence in the flow are counteracted by the increasingly stabilising effect of the magnetic field. Due to these two opposing mechanisms, incoherent oscillation patterns emerge.

2. Sloshing and torsion modes are absent. Once the magnetic field has completely suppressed the torsion and sloshing modes, no oscillations are visible in the temperature and flow orientation measurements of the LSC at low thermal driving $\text{Ra} < 3 \times 10^6$. For $\text{Ra} > 3 \times 10^6$ the oscillation modes are suppressed as well, but thermal plumes are appearing outside the general LSC path and are entrained into the LSC after some time. These plumes are the first sign of the breakdown of the LSC.

5.2.2. Intermediate magnetic fields: Cellular flow structure

As the magnetic field suppresses the intensity and turbulence of the convective flow, the single roll of the LSC can not be sustained. Like in laminar convection, the flow structure becomes dominated by multiple up- and down-flows. These organise into convection cells and rolls [11, 104]. The information on the flow in the experiment is rather limited, but applying some simplifying assumptions, the measurements of the ten UDV sensors and the thermocouple array are sufficient to derive the large scale flow structure. In this section it is assumed, that azimuthal flows are negligible over the turnover time scales due to the symmetry of the set-up, similar to how the drift time scale τ_{drift} of the LSC was much larger than the torsion period τ_{osc} for $\text{Ha} = 0$. Additionally, the flow is assumed to be mostly homogeneous along the z-axis and horizontal flows are concentrated near the heating and cooling plate. This is motivated by the known magnetohydrodynamic effect, that a magnetic field tends to homogenise the flow field along its direction [5, 31].
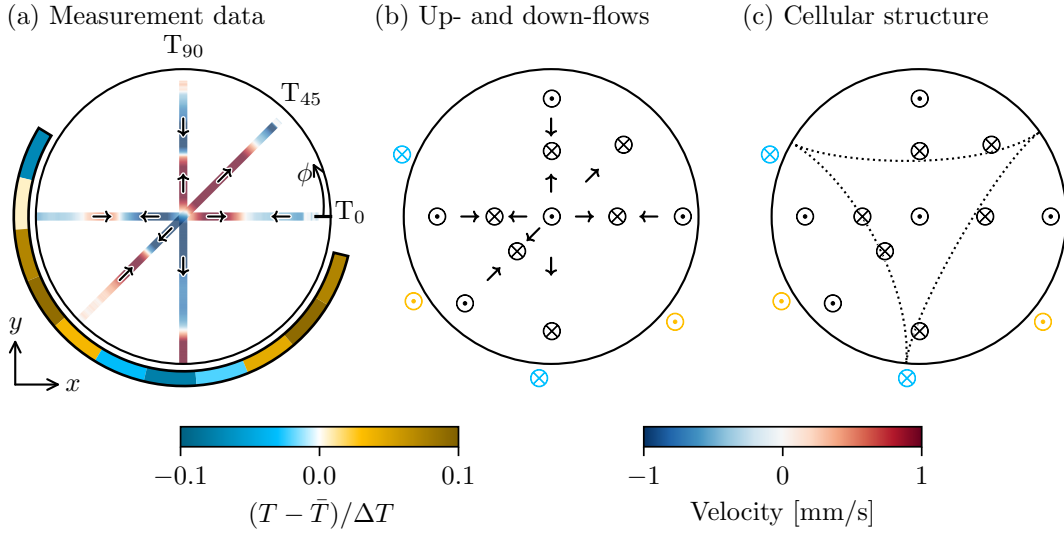
(a) Measurement data   (b) Up- and down-flows   (c) Cellular structure

$$(T - \bar{T})/\Delta T$$

Velocity [mm/s]

Figure 5.9.: Identification steps of the cellular flow structure at the top plate for a measurement at $\mathrm{Ra} = 3.3 \times 10^7$ and $\mathrm{Ha} = 1050$. Shown is the top view of the cell near the top plate. (a) Measurement data averaged over $100\tau_{\mathrm{ff}}$. The temperature data at half-height is shown around the circumference of the cell. The velocity data of sensors T_0, T_{45} and T_{90} are shown along their respective measurement line. The velocity directions are indicated by arrows. (b) Identification of the position of up- and down flows ($\odot$ and $\otimes$, respectively) from diverging or converging flows (black symbols) and from the temperature extrema (orange and blue symbols). (b) Connection of the down-flow positions (dotted line) to a coherent cellular flow structure of four up-flowing areas, separated by a triangular down-flowing boundary.

Figure 5.9 shows an example of how the flow structure is identified from the temperature data at mid-height, and the velocity data measured the sensors by T_0, T_{45}, and T_{90} near the top plate. The measurements were taken at $\mathrm{Ra} = 3.3 \times 10^7$ and $\mathrm{Ha} = 1050$ and their time averages over $100\tau_{\mathrm{ff}}$ are displayed in figure 5.9(a). It shows a top view of the horizontal cross section near the top plate with a black circle indicating the side walls. The temperature at mid-height is plotted around the circumference of the cell and the velocity data is plotted along the beam-lines of the respective UDV sensor across the diameter of the cell. The direction of the flow is indicated by arrows on top of the velocity data. These show multiple points along the measurement lines, where the flow is converging or diverging. Especially in the centre of the cell a diverging flow is shown by all UDV sensors, implying uprising fluid that impinges on the top plate and spreads radially outwards. At the side walls, the temperature extrema give the positions of warm up- and cold down-flows. For example, the hot imprint at $\phi \sim 225°$ indicates up-welling fluid, which hits the top plate and flows radially inward as measured by T_{45}. This flow is then converging with the outward flow from the centre and suggests the presence of a vertical down-flow. Similarly, the low temperature imprint at $\phi \sim 270°$ gives an down-welling flow, which is fed by the outwards streaming fluid measured by T_{90}. Close to the wall, T_{90} records a small interval with inward flowing fluid. This seems to be a small recirculation vortex in the corner of the cell, since
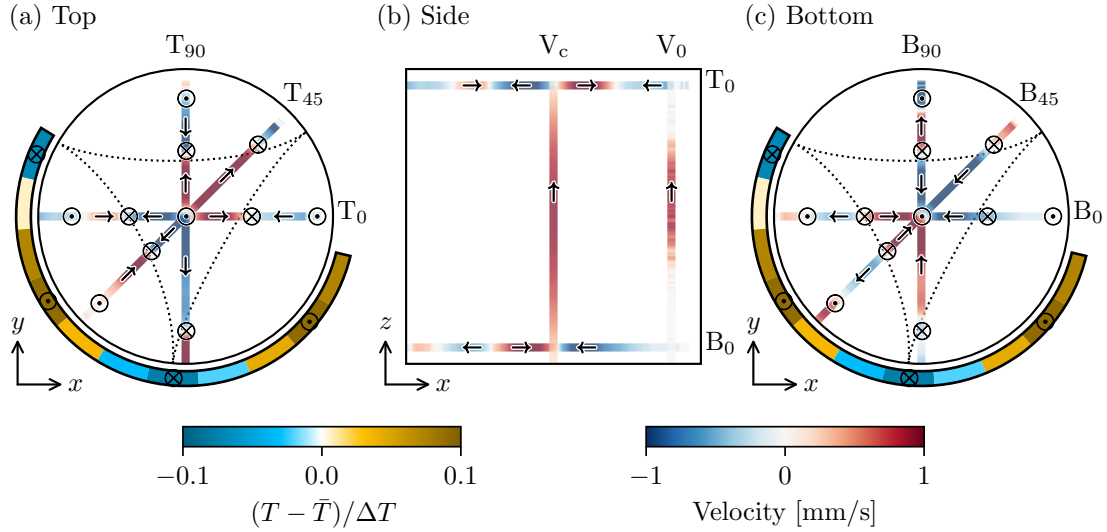
Figure 5.10.: Cellular flow structure for a measurement at $\mathrm{Ra} = 3.3 \times 10^7$ and $\mathrm{Ha} = 1050$. See figure 5.9 for details on the quantities shown. (a) Top view of cell near the top plate. (b) Side view of cell in the x-z plane. The velocities measured by V_c are scaled by a factor of 0.1. (c) Top view of cell near the bottom plate. The positions of the up- and down-flows are replotted from (a).

the outward and downward flowing fluid at that azimuthal position coincide very well with one another. In figure 5.9(b), all positions of up- and down-flows identified in the measurement data are marked with $\odot$ and $\otimes$, respectively. The markers derived from the temperature data are coloured in orange and light blue, respectively. Along the side wall of the cell, down- and up-welling flows alternate three times, giving an three-fold azimuthal symmetry. Additionally, all three up-welling flows at the side wall are separated from the central up-flowing region by down-flows. Connecting the positions of the down-welling flows in figure 5.9(c) gives the final picture of the large-scale structure: Four disjoint regions of up-flowing fluid are separated by a contiguous boundary of down-welling fluid in a triangular shape. Due to the four individual up-flows, this structure is termed the 4 cells pattern.

Of course, this identification of the flow regime at the top plate has to be consistent with the data of the remaining UDV sensors. The same analysis as depicted in figure 5.9 can also be applied to the UDV sensors B_0, B_{45} and B_{90} near the bottom plate. This is shown in figure 5.10(c), with the identification steps from figure 5.9 joint into one diagram. The up- and down-flow positions are replotted from figure 5.9. For comparison, the results from the top plate are also shown in figure 5.10(a) in the same manner. At the bottom plate, converging and diverging flows suggest rising and sinking fluid, respectively. The velocity data confirms the position of the vertical flows from the top plate, with a converging flow in the centre and a threefold azimuthal symmetry around the circumference. This supports the previous assumption that the flow is mostly homogeneous along the z-axis except near the plates. The only major inconsistency can be found at $\phi = 0$, where a radial outward flow would be expected at the wall, but a very weak inward flow is measured by B_0. At this azimuthal position, V_0 determines the vertical velocity
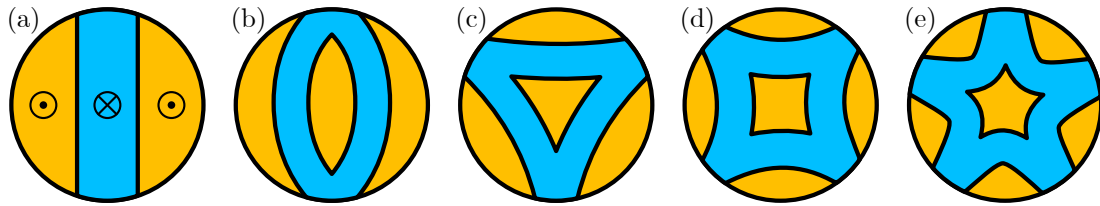
Figure 5.11.: Flow patterns of the cellular convection regime. (a) to (e): Schematic top view of the experiment with 2 to 6 convection cells. Blue areas indicate cold down-flow and orange areas indicate warm up-flow (marked in (a) by $\otimes$ and $\odot$, respectively). Each pattern may also appear with inverted flow directions.
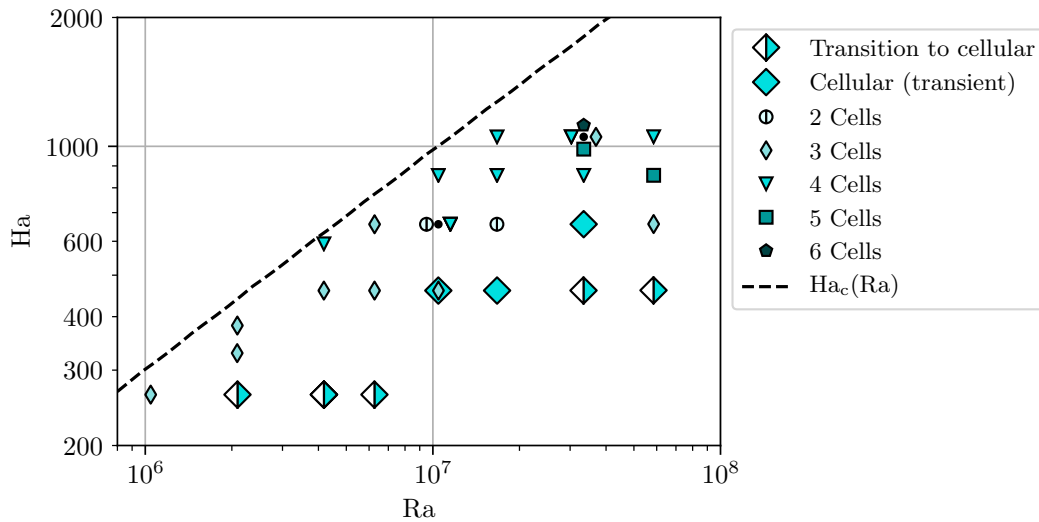

Figure 5.12.: Map of the cellular flow regime over the $(\mathrm{Ra}, \mathrm{Ha})$ phase space. If multiple flow structures are identified at the same $(\mathrm{Ra}, \mathrm{Ha})$, the markers are clustered around a black dot, which marks the measurement point.

at $r/R = 0.8$ (figure 5.10(b)). It shows a vertical up-flow around mid-height of the cell which confirms the result from the measurement at the top. The vertical velocity data by $\mathrm{V_c}$ along the central axis is also plotted in figure 5.10(b). Like the converging and diverging flows at the bottom and top plate, respectively, it confirms the existence of up-welling fluid in the cell centre.

The flow pattern can be reconstructed as shown in figure 5.10 for most measurements in the cellular regime. Figure 5.11 illustrates the five different patterns that could be identified. Each pattern is named after the number of cells it contains. The n cells pattern consists of one up-flow in the centre, and $n-1$ up-flows along the side wall. These are separated by a continuous boundary of down flowing fluid. The pattern thus has an $n-1$ azimuthal symmetry. Only the 2 cells pattern (figure 5.11(a)) does not have a central up-welling cell and displays a twofold symmetry like the 3 cells pattern. Each pattern can also appear with inverted velocities, i.e. with a central down-flow and up-flows as the cell boundaries.

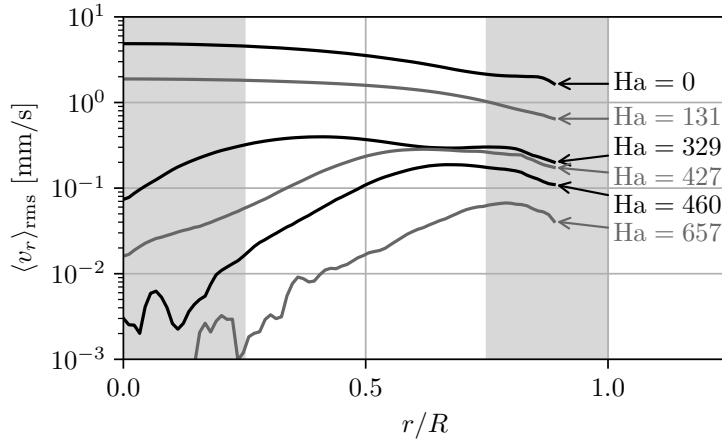Figure 5.12 shows the distribution of the flow patterns in the cellular regime over the $(\mathrm{Ra}, \mathrm{Ha})$

Figure 5.13.: Radial velocity intensity profiles $\langle v_r \rangle_{\mathrm{rms}}(r)$ for different Ha at $\mathrm{Ra} = 2.1 \times 10^6$ ($\mathrm{Ha_c} = 443$). The rms-average is taken over time and all horizontal UDV sensors. A median filter was applied to the velocity data to eliminate noise. The measurements correspond to the ones shown in figure 5.3. The light grey areas mark the radial ranges of the profile used to calculate v_{inner} (left) and v_{outer} (right).

phase space. In addition to the cell patterns from figure 5.11, two more types of flows appear at the lower Ha-boundary of the regime. The first marks a transitional pattern from the LSC regime to a cellular structure. This either means, that the measurement shows an LSC pattern, which intermittently switches to a cellular pattern and back, or the flow starts with a cellular pattern and switches back to a LSC structure. The second new pattern indicates a highly transient flow, which is clearly cellular, but cannot be assigned to any of the n cells patterns. Multiple measurements at the same point $(\mathrm{Ra}, \mathrm{Ha})$ can also result in different patterns or they may switch during the measurement. However, the number of cells generally increases with the Rayleigh number.

5.2.3. Strong magnetic fields: Magnetic wall modes

As shown before in figure 5.3, the Hartmann number can be increased above the onset of convection $\mathrm{Ha_c}$ and a flow is still detectable by the thermocouple array at mid-height. This flow can also be measured by the UDV sensors. Figure 5.13 displays the radial velocity profile $\langle v_r \rangle_{\mathrm{rms}}$ from measurements at $\mathrm{Ra} = 2.1 \times 10^6$ previously shown in figure 5.3. To calculate $\langle v_r \rangle_{\mathrm{rms}}$, the velocity profiles of the UDV sensors are filtered using a median filter with a kernel size of 5 measurements in time and 5 mm along the measurement line of the sensors. This removes artefacts and noise from the measurements which are present especially for slow flows below $1\,\mathrm{mm\,s^{-1}}$. The rms-average is then taken over time and over the data of all horizontal UDV sensors ($\mathrm{T_0}$, $\mathrm{T_{45}}$, $\mathrm{T_{90}}$, $\mathrm{M_0}$, $\mathrm{M_{90}}$, $\mathrm{B_0}$, $\mathrm{B_{45}}$, and $\mathrm{B_{90}}$). $\langle v_r \rangle_{\mathrm{rms}}$ represents the average flow intensity at a given radius of the cell. First, it can be seen in figure 5.13 that the maximum velocity magnitude continually decreases with increasing Ha from $\sim 5\,\mathrm{mm\,s^{-1}}$ at $\mathrm{Ha} = 0$ to $\sim 0.07\,\mathrm{mm\,s^{-1}}$ at $\mathrm{Ha} = 657$. Secondly, the shape of the profiles change in accordance to the large-scale flow
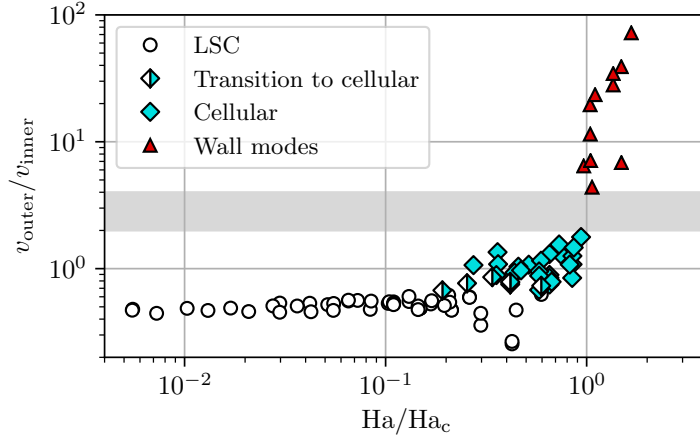
Figure 5.14.: Ratio of the outer and inner flow intensity (5.1) over the Hartmann number Ha normalised by the critical Hartmann number $\mathrm{Ha_c}$. Flow regimes are indicated by the marker shape and colour. The light grey area marks a gap in the data between the cellular and wall mode regime.

regime. For the lowest $\mathrm{Ha} = 0$ and 131, the flow is in the LSC regime (see figure 5.6). The profile is dominated by the strong horizontal flow near the plates, which gives a maximum at the centre of the cell ($r/R = 0$). For the profile at $\mathrm{Ha} = 329$, the flow is in the cellular regime (this specific measurement shows a pattern of 3 cells, see figure 5.12). The velocity magnitude is uniformly distributed over a large portion of the radius. Only in the centre it shows a pronounced minimum due to the strong vertical flow at that position (see figure 5.11(b)). For the Rayleigh number of these measurements $\mathrm{Ra} = 2.1 \times 10^6$, the onset of convection for $\Gamma \to \infty$ is at $\mathrm{Ha_c} = 443$. The profiles at $\mathrm{Ha} > \mathrm{Ha_c}$ still show velocities of a magnitude $\sim 1\,\mathrm{mm\,s^{-1}}$. Their maximum is shifted closer to the side wall and the velocity rapidly decreases towards the cell centre by one order of magnitude. This is in stark contrast to the cellular regime, which had convection cells and rolls distributed within the whole volume of the fluid. Since the flow is predominantly located at the side walls, this flow regime is denoted as the wall mode regime.

In order to distinguish the wall mode and cellular regime, the flow strength in the centre of the cell and near the side walls are compared. They are defined as the average velocity over the inner and outer 25 %, respectively, of the radial flow profiles $\langle v_r \rangle_{\mathrm{rms}}$. These ranges are marked in figure 5.13 by a light grey background. The characteristic inner and outer flow intensity are denoted by

$$v_{\mathrm{inner}} = \left\langle \langle v_r \rangle_{\mathrm{rms}}(r) \right\rangle_{0 \leq r \leq 0.25R} \qquad \text{and} \qquad v_{\mathrm{outer}} = \left\langle \langle v_r \rangle_{\mathrm{rms}}(r) \right\rangle_{0.75R \leq r \leq R}, \qquad (5.1)$$

respectively. These quantities are only calculated for measurements with $\mathrm{Ha/Ha_c} < 2$. For higher $\mathrm{Ha/Ha_c}$ the overall radial velocities become too small to be reliably measured by the UDV sensors. The ratio $v_{\mathrm{outer}}/v_{\mathrm{inner}}$ is displayed in figure 5.14 over $\mathrm{Ha/Ha_c}$. The measurements in the LSC regime show ratios of ~ 0.5, since the flow profiles are strongest in the cell centre. In the cellular regime the ratio increases up to ~ 2 due to the more uniform distribution of the flow intensity over the radius. When approaching the critical Hartmann number $\mathrm{Ha/Ha_c} = 1$,
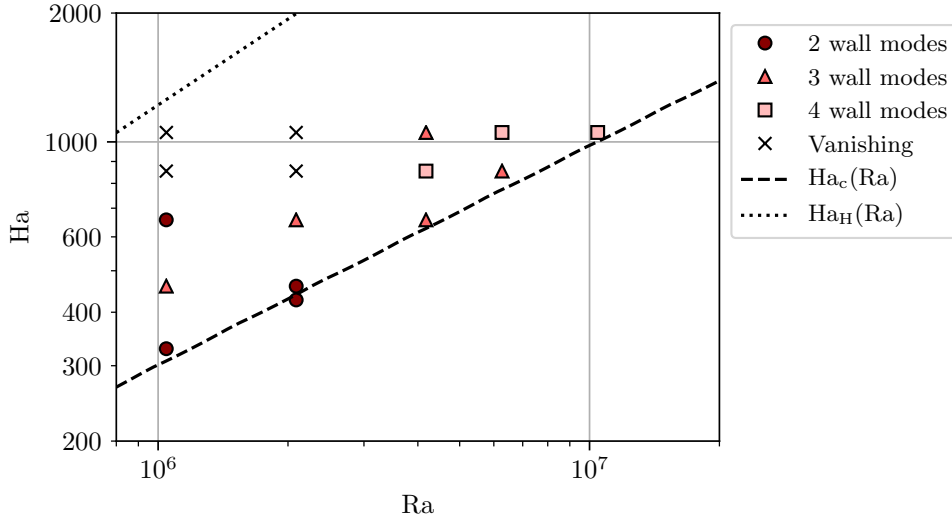
Figure 5.15.: Map of the wall mode regime over the $(\mathrm{Ra}, \mathrm{Ha})$ phase-space. The number of wall modes are determined from the number of up-and down flows in the temperature profile at half height. The vanishing regime indicates measurements without measurable flow.

the data record shows a gap between $2 < v_{\mathrm{outer}}/v_{\mathrm{inner}} < 4$ (marked by a light grey area). All measurements above this gap are considered to be part of the wall mode regime, displaying significantly higher velocities at the side wall than in the centre of the cell. The transition to wall modes perfectly coincides with the critical Hartmann number $\mathrm{Ha_c}$. Only one measurement is below this threshold at $\mathrm{Ra} = 2.1 \times 10^6$ and $\mathrm{Ha} = 427$, giving $\mathrm{Ha}/\mathrm{Ha_c} = 0.97$. The $\langle v_r \rangle_{\mathrm{rms}}$ profile of this measurement is shown in figure 5.13. It has the same trend as the profiles at higher Ha with a strong decrease towards the cell centre. The transition to the wall mode regime might thus not lie exactly on the $\mathrm{Ha} = \mathrm{Ha_c}$ curve, but at slightly lower Ha. The measurement with the highest $\mathrm{Ha}/\mathrm{Ha_c}$ ratio in the cellular regime has a value of $\mathrm{Ha}/\mathrm{Ha_c} = 0.94$ (at $\mathrm{Ra} = 4.2 \times 10^6$).

Figure 5.15 shows the $(\mathrm{Ra}, \mathrm{Ha})$ phase space of the wall mode regime. The transition to wall modes at $\mathrm{Ha} \sim \mathrm{Ha_c}$ was also found in numerical simulations by Liu et al. [75] within a rectangular geometry of width-to-height aspect ratio 4. In the central region of the cell the influence of the side walls is negligible and the fluid acts like in an horizontally infinitely extended layer. This means that for $\mathrm{Ha} > \mathrm{Ha_c}$, the convection in the centre of the cell should be completely suppressed. The velocities measured in the centre (see figure 5.13) are due to the remaining influence of the side walls. The importance of cell walls on the onset of magnetoconvection has been investigated by Houchens et al. [105] theoretically. The electrical boundary conditions are of major relevance. Electrically conducting side walls do not change the onset of convection significantly. However, electrically insulating side walls require the induced eddy currents to close within the fluid in a layer near the wall called the Shercliff layer [105, 106]. This decreases the magnitude of the eddy currents in comparison to the case of conducting side walls and in turn weakens the Lorentz forces acting on the fluid. The suppression of the convective flow is

thus smaller in the vicinity of the non-conducting side walls than in the centre of the cell. The resulting new onset of convection in a $\Gamma = 1$ cylindrical cell is, according to Houchens et al. [105], given by

$$\mathrm{Ha_H} = \left(\frac{\mathrm{Ra}}{23.48183}\right)^{2/3} \qquad \text{for Ra} \gtrsim 9.3 \times 10^4\,, \qquad (5.2)$$

$$\mathrm{Ra_H} = 23.48183 \times \mathrm{Ha}^{3/2} \qquad \text{for Ha} \gtrsim 250\,. \qquad (5.3)$$

The value of $\mathrm{Ha_H}$ is larger and increases faster than the Chandrasekhar limit $\mathrm{Ha_{Ch}} \propto \mathrm{Ra}^{1/2}$. This onset of convection for $\Gamma = 1$ is plotted in figure 5.15 as a dotted line. The present experiments do not reach past this boundary. However, even before reaching $\mathrm{Ha_H}$ the velocity and temperature measurements cannot detect a distinct flow any more. These data points are denoted as the vanishing regime (crosses in figure 5.15). It is unclear, whether this contradicts the theoretical value of $\mathrm{Ha_H}$. A very slow flow close to the side wall may not be detectable by the UDV sensors and the temperature imprint of this flow may be below the thermocouple accuracy.

The wall modes exhibit an azimuthal periodicity, which can be seen in the mid-height temperature profile (see Ha $= 460$ and 657 in figure 5.3). Similar to the evaluation of the cellular regime, the number of wall modes along the whole circumference can be estimated by counting the up- and down-flows visible in the temperature profile over half the circumference, assuming an even distribution along the whole side wall. One wall mode comprises one up- and one down-flow. In figure 5.15, the number of wall modes is indicated by the shape and colour of the markers. The measurements show that the mode number tends to increase with the Rayleigh number. A more rigorous investigation on this observation would benefit from temperature measurements around the whole cell circumference and a more densely sampled phase space.

The existence of wall modes in magnetoconvection can be compared to the behaviour of rotating convection. These two convection systems have mathematical similarities [5] and display a number of equivalent properties. For example, the rotation of a convection cell stabilises the flow and pushes the onset of convection to higher Ra, just like the vertical magnetic field does in magnetoconvection. It is a long known feature of rotating convection, that the side walls of a cell induce an instability, which lets a flow set in at temperature difference which are lower than the critical temperature difference for an horizontally infinite fluid layer without side walls [107]. These sub-critical flow modes are concentrated close to the side walls and exhibit an azimuthal periodicity of different numbers of up and down moving flows, just like in the present case. The mode number was also seen to depend on the execution of the experiment, e.g. approaching the target temperatures with different speeds can lead to different mode numbers. This challenges the above observation, that the number of wall modes in magnetoconvection shows a trend to higher values for increasing Ra and repeated measurements with different experimental executions should be considered in future investigations on this topic.

5.2.4. Flow regime map and transitions

The distribution of the main flow regimes over the $(\mathrm{Ra}, \mathrm{Ha})$ phase space are displayed in figure 5.16. As mentioned before, the most distinct transition is between the cellular and the wall mode regime, which lies along Ha $= \mathrm{Ha_c}$. The transition between the LSC and the cellular
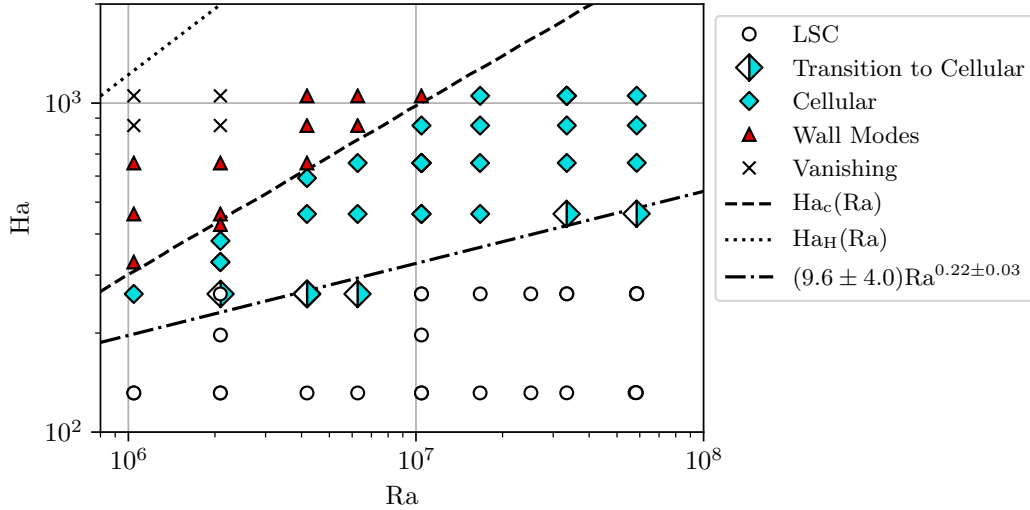
Figure 5.16.: Flow regime map over the $(\mathrm{Ra}, \mathrm{Ha})$ phase-space for measurements with $\mathrm{Ha} > 100$. Experiments for $\mathrm{Ha} < 100$ are in the LSC regime and still display the torsion and sloshing modes (see figure 5.6). The dash-dotted line is a least-squares power law fit to the measurements in the transition to cellular regime.

regime is more ambiguous. At multiple points a clear association of the flow structure with either regime was not possible. Here, a more dense sampling of the phase space could give a more clear picture of the transition. Nonetheless, in order to estimate a position of the transition, a power law is fitted to the points of the transition to cellular regime. The resulting function is $\mathrm{Ha} \simeq (9.4 \pm 4.0) \pm \mathrm{Ra}^{0.22 \pm 0.03}$ and is indicated by the dash-dotted line in figure 5.16. This is only a rough local estimate of the transition position, since an extension of this power law would lead to an intersection with the Chandrasekhar limit at $\mathrm{Ra} \sim 2 \times 10^5$.

Recent numerical simulations of RBC in a vertical magnetic field at $\mathrm{Pr} = 1$ by Yan et al. [76] also detected a cellular and turbulent regime. In between, an additional regime of columnar convection was discovered, which was also present for simulations at $\mathrm{Pr} = 0.025$ and $\mathrm{Ha} = 1414$. This regime is characterised by thin up-and down-welling flow columns distributed over the whole cell. Such a flow was not detected in the present experiment. This may have a number of reasons. First, the low-Pr simulations use stress-free boundary conditions and a box geometry with a width-over-height aspect ratio $\Gamma \sim 1.5$ and 3. Geometry effects might be more dominant with the no-slip boundary conditions of the present experiment. Secondly, their data suggests that the size of the columnar regime in the $(\mathrm{Ra}, \mathrm{Ha})$ phase space shrinks with decreasing Pr and Ha, though it is unclear, whether it might vanish completely at some point.

In conclusion, the regime map in figure 5.16 and the preceding sections give a broad overview of the flow structures in magnetoconvection and their transitions. These findings show the successive suppression of turbulence by the magnetic field, which causes the flow to transition into a laminar state and ultimately suppresses convection in the cell centre, leaving only a very weak flow in the vicinity of the side walls. These findings can serve as a guide to plan future experiments and localise regions of interest which merit further investigation.
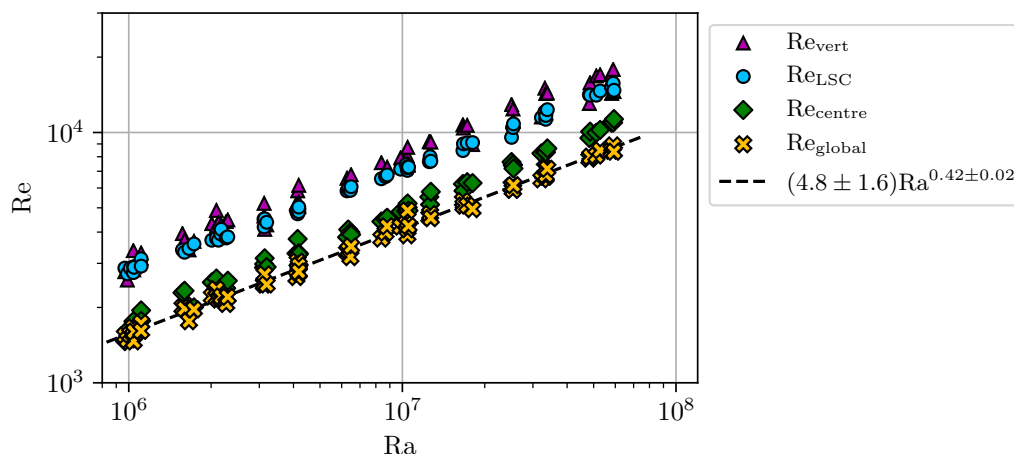
Figure 5.17.: Global Reynolds number $\mathrm{Re}_{\mathrm{global}}$ over Ra at $\mathrm{Ha} = 0$ (relative uncertainties are $\sim 11\,\%$). For comparison, the Reynolds numbers $\mathrm{Re}_{\mathrm{LSC}}$, $\mathrm{Re}_{\mathrm{vert}}$, and $\mathrm{Re}_{\mathrm{centre}}$ have been replotted from figure 4.13.

5.3. Global transport properties

As the large-scale flow structure of the magnetoconvection system changes, the transported heat and momentum are influenced as well. This section deals with the changes of the Nusselt and Reynolds number with increasing magnetic fields. Their values at $\mathrm{Ha} = 0$ from section 4.3 will in the following be identified with a subscript "0": $\mathrm{Nu}_0(\mathrm{Ra}) \equiv \mathrm{Nu}(\mathrm{Ra}, \mathrm{Ha} = 0)$ and $\mathrm{Re}_0(\mathrm{Ra}) \equiv \mathrm{Re}(\mathrm{Ra}, \mathrm{Ha} = 0)$. The Nusselt number in magnetoconvection is determined the same way as previously in section 4.3.1.

The Reynolds number has to be treated somewhat differently. The definitions of $\mathrm{Re}_{\mathrm{LSC}}$, $\mathrm{Re}_{\mathrm{vert}}$ and $\mathrm{Re}_{\mathrm{centre}}$ calculated in section 4.3.2 are motivated by the LSC structure of the flow and cannot be readily adopted in the cellular or wall mode regime. Since the highly complex and diverse flow patterns at large Ha are only sparsely sampled by the UDV sensors, any similar definition of a Reynolds number in these regimes would have to be adjusted for nearly each individual measurement. This could potentially inject a subjective factor into the calculation. Instead, a singular Reynolds number definition is used for all regimes. The characteristic velocity is determined by taking all measured UDV velocity profiles and calculating the rms-average over all sensors, along their beam-lines, and time. This mimics the approach taken by many numerical simulations which determine the characteristic velocity of the flow from the rms-average of the velocity magnitude over the whole cell volume, and time [75, 98]. With this in mind, the resulting velocity is denoted as v_{global} and the corresponding global Reynolds number is

$$\mathrm{Re}_{\mathrm{global}} = \frac{v_{\mathrm{global}} H}{\nu} \,. \tag{5.4}$$

The values of $\mathrm{Re}_{\mathrm{global}}$ for $\mathrm{Ha} = 0$ are plotted in figure 5.17. It has a very small magnitude, even lower than $\mathrm{Re}_{\mathrm{centre}}$ calculated from the fluctuations in the cell centre. Its power law scaling of $\mathrm{Re}_{\mathrm{global},0} \simeq (4.8 \pm 1.6)\mathrm{Ra}^{0.42 \pm 0.02}$ displays the same exponent as $\mathrm{Re}_{\mathrm{LSC}}$ and $\mathrm{Re}_{\mathrm{vert}}$ (see

figure 4.13). This shows, that $\mathrm{Re_{global}}$ is still dominated by the fastest velocities of the flow but its overall magnitude is decreased due to the many low speed regions probed by the UDV sensors.

It should be noted, that this definition of $\mathrm{Re_{global}}$ displays some biases. The radial velocities at top and bottom plate are over-represented with six sensors compared to two radial sensors at mid-height and two vertical sensors. Also, the wall modes are strongest close to the wall, which is an area not covered well by the sensors. Still, this definition of the Reynolds number is not based on any specific flow structure and can thus be applied to all flow regimes equally.

The data of $\mathrm{Nu(Ra, Ha)}$ and $\mathrm{Re_{global}(Ra, Ha)}$ can be described well by

$$\frac{\mathrm{Nu} - 1}{\mathrm{Nu_0} - 1} \simeq \frac{1}{1 + C_1 \left(\frac{\mathrm{Ha}}{\mathrm{Ra}^{\beta_1}}\right)^{\gamma_1}}, \tag{5.5}$$

$$\frac{\mathrm{Re_{global}}}{\mathrm{Re_{global,0}}} \simeq \frac{1}{1 + C_2 \left(\frac{\mathrm{Ha}}{\mathrm{Ra}^{\beta_2}}\right)^{\gamma_2}} \tag{5.6}$$

This empirical representation is similar to a model used by Cioni et al. [71]. Nu and $\mathrm{Re_{global}}$ are normalised by their values without magnetic field (an average over all measurements at $\mathrm{Ha} = 0$ and the same Ra). For the Nusselt number its convective part $\mathrm{Nu} - 1$ is considered. An ODR fit of (5.5) and (5.6) to the data gives the parameter values

$$C_1 = 20 \pm 11, \qquad \beta_1 = 0.46 \pm 0.02, \qquad \gamma_1 = 2.12 \pm 0.07, \tag{5.7}$$
$$C_2 = 0.10 \pm 0.05, \qquad \beta_2 = 0.24 \pm 0.02, \qquad \gamma_2 = 1.74 \pm 0.05. \tag{5.8}$$

The exponents β_1 and β_2 of Ra are very close to $1/2$ and $1/4$, respectively. This is a motivation to relate the Ra dependency with the Chandrasekhar limit: $\mathrm{Ra}^{0.46} \sim \sqrt{\mathrm{Ra}} = \pi \mathrm{Ha_{Ch}} \approx \pi \mathrm{Ha_c}$ and $\mathrm{Ra}^{0.24} \sim \sqrt[4]{\mathrm{Ra}} = \sqrt{\pi \mathrm{Ha_{Ch}}} \approx \sqrt{\pi \mathrm{Ha_c}}$. Plotting the normalised Nusselt number over $\mathrm{Ha/Ha_c}$ in figure 5.18 and the normalised global Reynolds number against $\mathrm{Ha}/\sqrt{\mathrm{Ha_c}}$ in figure 5.19 shows that all data over the whole Rayleigh number range collapse onto one curve. At low Ha, the Nusselt and Reynolds number stay at their respective value without magnetic field. With increasing Ha, the values start to drop and continually decrease towards higher magnetic fields. The scaling of the heat transport as a function of $\mathrm{Ha/Ha_c}$ is already widely known [71–73, 75]. The Reynolds number is less well studied and a collapse over $\mathrm{Ha}/\sqrt{\mathrm{Ha_c}}$ has, to the author's knowledge, not been reported yet.

Figure 5.18 and 5.19 also display the flow regimes of each measurement. The normalised Nusselt number stays at its initial value for nearly the whole LSC regime and drops to values of $\sim 80\%$ only shortly before the transition to the cellular regime. In contrast, $\mathrm{Re_{global}/Re_{global,0}}$ starts to drop much earlier over the whole LSC regime, reaching values of $\sim 30\%$ before the transition towards the cellular regime sets in. The heat transport is thus not directly related to the overall intensity of the flow. While the magnetic field decreases the flow speed, it also suppresses the turbulent fluctuations and oscillations. This can improve the heat advection by increasing the coherence of the flow, which is a well known effect in a number of different convection systems [77, 108]. A recent numerical study by Lim et al. [77] on RBC in a vertical magnetic field at $\mathrm{Pr} = 8$ even found an increase of the Nusselt number at an optimal Ha. For $\mathrm{Ra} = 10^7$ they found an increase of $\mathrm{Nu/Nu_0} \sim 1.02$ at $\mathrm{Ha} \sim 20$. Such an effect is not observed in the
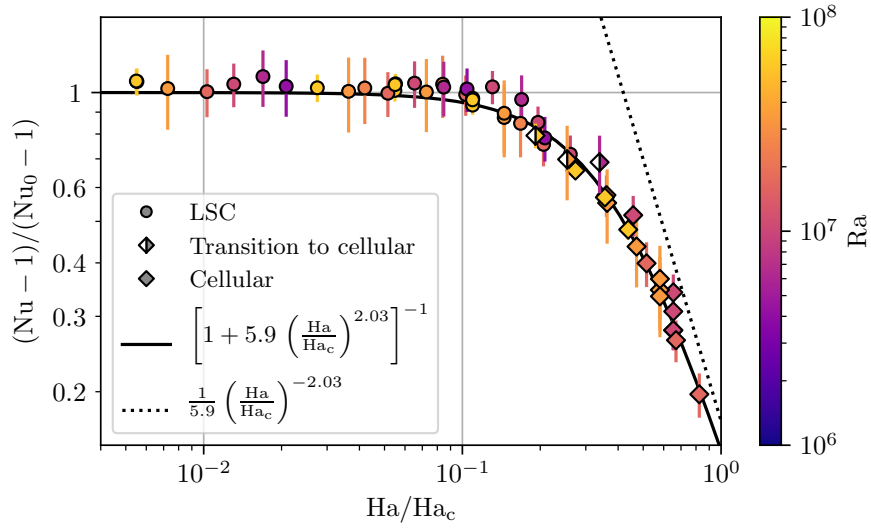
Figure 5.18.: Heat transport scaling with magnetic field strength. The normalised Nusselt number $(\text{Nu} - 1)/(\text{Nu}_0 - 1)$ is plotted versus the normalised Hartmann number Ha/Ha_c. The Rayleigh number Ra and flow regime of the measurements are indicated by colour and shape, respectively, of the markers. The dotted line gives the asymptotic behaviour for the fit function (5.9) (solid line) for $\text{Ha} \to \infty$.
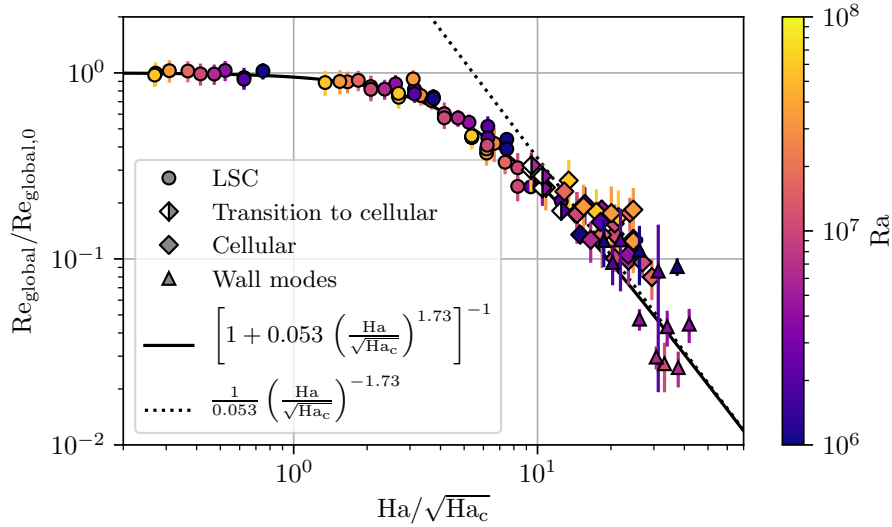

Figure 5.19.: Momentum transport scaling with magnetic field strength. The normalised global Reynolds number $\text{Re}_{\text{global}}/\text{Re}_{\text{global},0}$ is plotted versus the normalised Hartmann number $\text{Ha}/\sqrt{\text{Ha}_c}$. The Rayleigh number Ra and flow regime of the measurements are indicated by colour and shape, respectively, of the markers. The dotted line gives the asymptotic behaviour for the fit function (5.10) (solid line) for $\text{Ha} \to \infty$.

present data because (i) such a low Ha range was sampled very sparsely, (ii) the measurement accuracy cannot resolve such low variations in Nu, or (iii) this effect might not be present in low-Pr magnetoconvection. Still, Nu remaining at its initial value Nu_0, while $\mathrm{Re_{global}}$ shrinks, shows that the heat transport is improved by the decrease of turbulent fluctuations.

Once the cellular regime is reached, the Nusselt number continually decreases until it cannot be detected any more by the present experiment, i.e. when the temperature difference of the in- and out-flowing cooling water falls below 0.2 K. The Reynolds number displays a less coherent behaviour. As mentioned before, the flow in the cellular regime is more diverse than in the LSC regime and as a result, the values of $\mathrm{Re_{global}}$ scatter more than at lower Ha. They also have a tendency towards higher values than in the LSC regime, since more UDV sensors are subjected to high velocities for cellular structures. The downwards trend of the flow intensity, however, continues consistently and finally transitions into the wall mode regime. Here, the Reynolds numbers are also scattered over a large range. Nonetheless, $\mathrm{Re_{global}}$ displays a consistent behaviour over all regimes, verifying its suitability to describe the momentum transport over the whole phase space.

Replacing $\mathrm{Ra}^{\beta_1} \to \mathrm{Ha_c}$ and $\mathrm{Ra}^{\beta_2} \to \sqrt{\mathrm{Ha_c}}$ in (5.5) and (5.6) leads to new representation the Nu and $\mathrm{Re_{global}}$ measurements

$$\frac{\mathrm{Nu}-1}{\mathrm{Nu}_0-1} \simeq \frac{1}{1+\tilde{C}_1\left(\frac{\mathrm{Ha}}{\mathrm{Ha_c}}\right)^{\tilde{\gamma}_1}}\,, \tag{5.9}$$

$$\frac{\mathrm{Re_{global}}}{\mathrm{Re_{global,0}}} \simeq \frac{1}{1+\tilde{C}_2\left(\frac{\mathrm{Ha}}{\sqrt{\mathrm{Ha_c}}}\right)^{\tilde{\gamma}_2}}\,. \tag{5.10}$$

A new ODR fit to the experimental data results in the parameters

$$\tilde{C}_1 = 5.9 \pm 0.3\,, \qquad\qquad \tilde{\gamma}_1 = 2.03 \pm 0.06\,, \tag{5.11}$$

$$\tilde{C}_2 = 0.053 \pm 0.007\,, \qquad\qquad \tilde{\gamma}_2 = 1.73 \pm 0.05\,. \tag{5.12}$$

The functions are plotted in figures 5.18 and 5.19 and match the data very well. At large Ha, (5.9) and (5.10) approach the power laws $\tilde{C}_1^{-1}(\mathrm{Ha}/\mathrm{Ha_c})^{-\tilde{\gamma}_1}$ and $\tilde{C}_2^{-1}(\mathrm{Ha}/\sqrt{\mathrm{Ha_c}})^{-\tilde{\gamma}_2}$, respectively (shown as dotted lines). Since these power laws apply to the normalised Nusselt and Reynolds numbers, the Ra dependences of Nu_0 and $\mathrm{Re_{global,0}}$ have to be taken into account. Using the scaling $\mathrm{Re_{global,0}} \simeq 4.8\,\mathrm{Ra}^{0.42}$ presented in figure 5.17 and $\mathrm{Ha_c} \approx \mathrm{Ha_{Ch}}$, the global Reynolds number is given by

$$\mathrm{Re_{global}} \simeq 34\,\mathrm{Ra}^{0.85}\mathrm{Ha}^{-1.73} \qquad \text{for large Ha.} \tag{5.13}$$

The exponents of Ra and Ha are close to $7/8 = 0.875$ and $7/4 = 1.75$, respectively. The Reynolds number scaling is thus close to

$$\mathrm{Re_{global}} \propto \left(\frac{\mathrm{Ra}}{\mathrm{Ha}^2}\right)^{7/8} \qquad \text{for large Ha.} \tag{5.14}$$
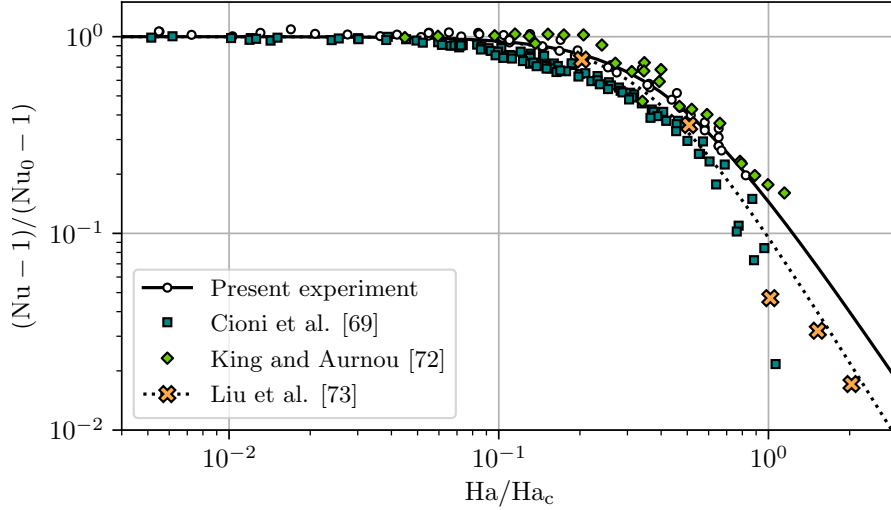
Figure 5.20.: Comparison of the present results for the Nusselt number with other experiments and simulations at low Pr (see also table 3.1). The lines represent fits of (5.9) to the respective data with parameters (5.11) (solid line) and (5.16) (dotted line).

The ratio $\mathrm{Ra}/\mathrm{Ha}^2$ can be interpreted as a magnetic Rayleigh number for which the viscosity ν is replaced with the magnetic viscosity $\nu_\sigma = \sigma B^2 H^2/\rho$ which quantifies the Joule dissipation (see (3.6)). This result suggests that for high Ha the momentum transport is dominated by the damping of the magnetic field and the kinematic viscosity can be neglected.

The normalised Nusselt number (5.9) is already a function of the magnetic Rayleigh number $\mathrm{Ra}/\mathrm{Ha}^2 \approx (\mathrm{Ha}/\mathrm{Ha_c})^{-2}/\pi^2$. The scaling of $\mathrm{Nu_0}$ was shown in figure 4.11 to be $\mathrm{Nu_0} \simeq 0.12\,\mathrm{Ra}^{0.27}$. Since the Nusselt number in the present experiment reaches at maximum values of 15, the convective part of the Nusselt number $\mathrm{Nu_0} - 1$ cannot be readily approximated by the full Nusselt number $\mathrm{Nu_0}$. Considering, that exponent $\tilde{\gamma}_1 \approx 2$ in (5.11), combining the power laws gives

$$\mathrm{Nu} - 1 \simeq \frac{0.12\,\mathrm{Ra}^{0.27} - 1}{58}\frac{\mathrm{Ra}}{\mathrm{Ha}^2} \qquad \text{for large Ha.} \qquad (5.15)$$

Even if this result is not a pure scaling law, it illustrates that the heat transport is not exclusively dominated by magnetic effects as was the case for the momentum transport. Both the regular Rayleigh number Ra and the magnetic Rayleigh number $\mathrm{Ra}/\mathrm{Ha}^2$ contribute to the scaling.

The data for Nu and $\mathrm{Re_{global}}$ can be compared with experiments by Cioni et al. [71] and King and Aurnou [74], as well as simulations by Liu et al. [75]. Nusselt numbers are reported in all these publications. Their normalised data is plotted, together with the present results, in figure 5.20. Overall, all data show a good agreement by following a common trend. The values by Cioni et al. [71] are generally smaller than the other data and decrease more quickly when approaching $\mathrm{Ha_c}$. The fit of (5.9) to the present experiment is replotted from figure 5.18 as a solid line. For $\mathrm{Ha} > \mathrm{Ha_c}$, the data by Liu et al. [75] are about half as big as the fit. A new fit
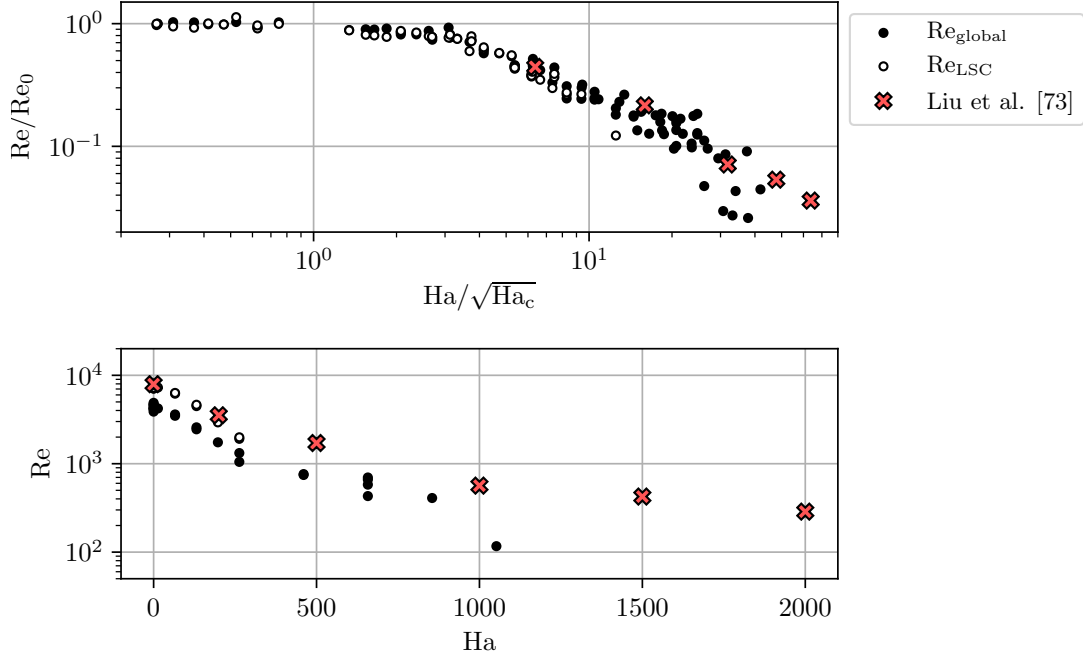
Figure 5.21.: Comparison of the present results for the global and LSC Reynolds numbers with numerical simulations by Liu et al. [75] (see also table 3.1). (a) Re/Re_0 over $Ha/\sqrt{Ha_c}$ for all available Ra. (b) Absolute Reynolds numbers Re over Hartmann number Ha for $Ra = 10^7$ with $Ha_c = 981$.

of (5.9) to the data by Liu et al. [75] result in parameter values of

$$\tilde{C}_1 = 10 \pm 2\,, \qquad\qquad \tilde{\gamma}_1 = 2.2 \pm 0.2\,. \qquad\qquad (5.16)$$

The resulting curve is plotted in figure 5.20 as dotted line. It shows a steeper decline for high Ha than the first fit but the uncertainty of the fitted exponent $\tilde{\gamma}_1$ in (5.16) is compatible with the initial results (5.11). This suggests that either not sufficient experimental data is available to properly extrapolate the model towards $Ha > Ha_c$ or that the model does not apply for $Ha > Ha_c$ because of a change in scaling due to the transition into the wall mode regime.

To the author's knowledge, so far no experimental Reynolds numbers were reported for RBC in a vertical magnetic field. Numerical data at small Pr have been published [75, 76]. Yan et al. [76] have conducted their simulations at $Ha = 1414$, which is outside the range of the present experiment. Since they also do not report corresponding values of Re at $Ha = 0$ their data can, unfortunately, not be compared with the present experiment. Liu et al. [75] calculated Re from the rms-average of the velocity magnitude over the whole fluid volume at $Ra = 10^7$ and $0 \leq Ha \leq 2000$. Their results are compared with the present experimental results in figure 5.21. The normalised Reynolds numbers in figure 5.21(a) show very good agreement. In addition to the global Reynolds number, Re_{LSC} has been plotted for measurements in the LSC regime. This confirms that not only Re_{global} exhibits the discussed behaviour. It was shown previously that the absolute values of Re_{global} are much smaller than Re_{LSC} (see figure 5.17). This difference is
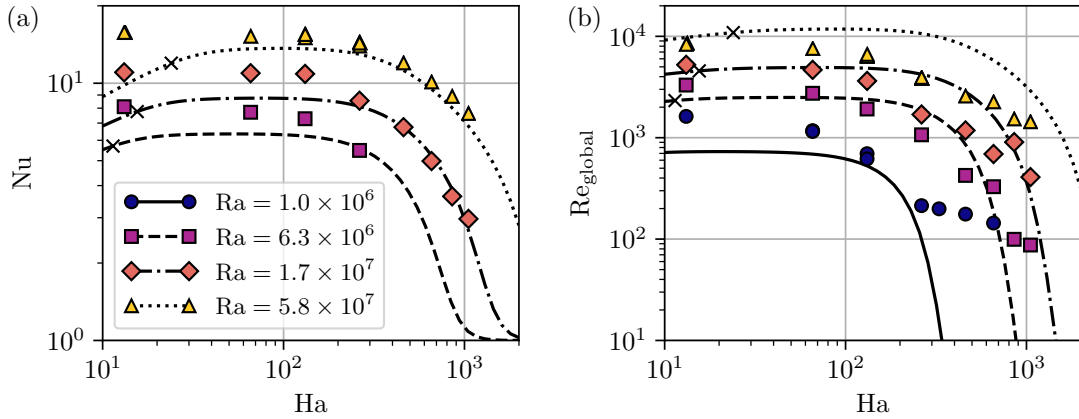
Figure 5.22.: Comparison of (a) Nu and (b) $\mathrm{Re_{global}}$ (markers) with the initial results (3.21) of the GL theory for magnetoconvection at $\mathrm{Pr} = 0.029$ (lines). The data is plotted over Ha for selected Ra. The boundary layer crossover $\delta_T = \delta_B$ in the model is marked by crosses on the lines.

cancelled out by the normalisation with their values at $\mathrm{Ha} = 0$. Figure 5.21(b) shows the absolute Re-values over Ha for $\mathrm{Ra} = 10^7$. As expected, $\mathrm{Re_{global}}$ is smaller than the Reynolds numbers from the simulations, but has a similar progression. Only one value in the wall mode regime at $\mathrm{Ha} > \mathrm{Ha_c} = 981$ shows a much smaller value than expected. This is caused by the very small velocities in the centre of the cell once wall modes are established. $\mathrm{Re_{LSC}}$ only reaches up to $\mathrm{Ha} \sim 250$, but for this short range it matches the simulations much better than $\mathrm{Re_{global}}$.

In conclusion, the dependence of Nu and Re on Ra and Ha could be described well by the model functions (5.9) and (5.10). A clear explanation for the exponents of the asymptotic scalings (5.15) and (5.14) for large Ha has not yet been found. To test the robustness of these scaling exponents, more experimental and numerical data are necessary.

5.4. Grossmann-Lohse theory for magnetoconvection

Using the new results for the heat and momentum transfer of the previous section, the theoretical model from chapter 3 can be validate and revised. This will be done in the following section. Afterwards, the revised model will be re-fitted and re-evaluated using all currently available experimental data (section 5.4.2).

5.4.1. Revision of the theoretical model

The Nusselt number Nu and global Reynolds number $\mathrm{Re_{global}}$ from the present experiment are compared with the results of the theoretical model with the initial parameters (3.21). Figure 5.22 shows the data over Ha for selected Ra. For the Nusselt number (figure 5.22(a)), a good agreement can be seen for $\mathrm{Ha} > 200$. For smaller Ha, the model under-predicts the experimental data and towards $\mathrm{Ha} = 0$ it drops off again. This is in stark contrast to the real data, which

saturates for $Ha \to 0$ at the value Nu_0. The drop-off at low Ha is caused by the boundary layer (BL) crossover $\delta_T = \delta_B$ of the model introduced in section 3.1.1 using the transition function $f(2Nu/Ha)$. The position of $\delta_T = \delta_B$ (i.e. $2Nu/Ha = 1$) along the model lines are marked by crosses. The Reynolds number in figure 5.22(b) shows a similar decrease towards $Ha = 0$, albeit being less pronounced. The model reproduces the Reynolds number less well than the Nusselt number. The initial slow decrease of Re_{global} during the LSC regime seen in figure 5.19 is not reproduced and the following drop for $Ha \to Ha_c$ is much steeper than in the experimental data, since the existence of wall modes is not incorporated into the model. The magnitude of Re is over-predicted for high $Ra \sim 6 \times 10^7$ and under-predicted for small $Ra \sim 10^6$.

The effect of the BL transition requires a more detailed discussion. As was seen in the results of the initial model fit to the data by Cioni et al. [71] and Liu et al. [75], the crossover line $\delta_T = \delta_B$ is situated below $Ha = 100$ for most of the Ra range shown. Only at $Ra \sim 6 \times 10^9$ does it cross to values $Ha > 100$. The model was said to be valid for $Ha \gg 1$, so that the viscous boundary layer is a Hartmann layer δ_B. The physically wrong effect of the BL transition suggests that in reality no crossover is taking place at these values of Ra and Ha. This is also reflected by the results of the classical GL theory for $Ha = 0$ [26]. There, the BL transition is predicted to occur at $Ra \sim 10^{12}$ for the Prandtl number of the initial model fit ($Pr = 0.025$). Below this Rayleigh number, the thermal BL is larger than the viscous BL, i.e. $\delta_T > \delta_v$, which is also confirmed by numerical simulations [18, 98]. Turning again to magnetoconvection, the magnetic field decreases the viscous BL thickness, eventually turning it into a Hartmann layer ($\delta_B \propto 1/Ha$). In contrast, the thermal BL with $\delta_T \propto 1/Nu$ is increasing since the convective heat transfer is inhibited by the magnetic field, i.e. Nu decreases. It is thus justified to assume that at low Prandtl numbers $\delta_T > \delta_B$ for the entire (Ra, Ha) phase space currently accessible by experiments and simulations. In the model, this is accomplished by setting $f(2Nu/Ha) \to 1$ in the model equations (3.17) and (3.18).

The BL crossover should only become relevant for very high Ra or for larger Pr. Indeed, in numerical simulations by Lim et al. [77] at $Pr = 8$ it is seen that the thermal BL is smaller than the momentum BL δ_p for low Ha and that a BL crossover happens for increasing Ha. δ_p is defined as the wall-near peak of $(\partial_x v_x)^2 + (\partial_y v_y)^2 + (\partial_z v_z)^2$, which measures the overall magnitude of the normal stress. A viscous BL thickness δ_v is also reported and gives similar results. The transition point $\delta_T = \delta_p$ is associated with an increase of the Nusselt number for a short range of Ha, which is similar to the behaviour created by the BL transition in the initial model. Such an increase in the Nusselt number is not visible in the present experimental data for $Pr = 0.029$ which may be traced back to the lack of a BL crossover.

Another issue of the initial model fit (3.21) were the negative values of c_2 and c_4. These pre-factors describe average dissipation rates, which are always positive. This was explained in section 3.2 and figure 3.2 by the limited range of Hartmann numbers in the experimental data used for fitting the model. To prevent this non-physical behaviour, the model parameters are restricted to the interval $(0, +\infty)$ in the fitting routine.

In conclusion, the following changes are applied to the model of heat and momentum transfer in magnetoconvection at low Pr:

1. The BL transition is removed, i.e. $f(2Nu/Ha) \to 1$.
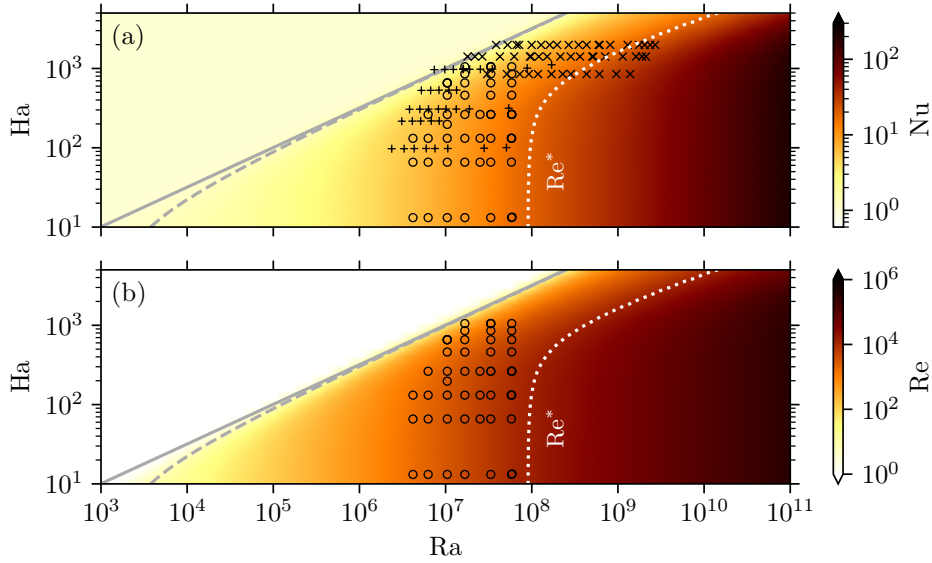2. All model parameters c_1 to c_6, and Re^* are restricted to the interval $(0, +\infty)$.

Figure 5.23.: Results of the theoretical model for parameters (5.17) and $Pr = 0.025$. (a) Nusselt number. (b) Reynolds number. Both diagrams show the Chandrasekhar limit Ha_{Ch} (solid line) used in the model and for comparison the real solution for the onset of convection Ha_c (dashed line). The dotted lines shows $Re = Re^*$. The positions of the fitting data from the present experiment, Cioni et al. [71], and King and Aurnou [74] are marked by circles, crosses, and pluses, respectively.

5.4.2. Revised theoretical results

The present experiment together with experimental data by Cioni et al. [71] and King and Aurnou [74] provide measurements of Nu over a much larger range of Ra and Ha than were used in the initial fit of the model. Additionally, experimental values of Re_{global} can now be used to fit the model, instead of numerical data. Together with the adjustments of the model discussed in the previous section, a new fit using these data results in the optimal model parameters

$$Re^* = 1.3 \times 10^4 \,, \quad c_1 = 1.0 \,, \qquad\qquad c_2 = 6.0 \,, \qquad c_3 = 0.034 \,,$$
$$c_4 = 1.2 \times 10^{-5} \,, \quad c_5 = 0.018 \,, \quad c_6 = 0.68 \,. \tag{5.17}$$

In comparison to the initial model parameters (3.21), the revised c_i vary less in their order of magnitude and are overall closer to 1. The previously negative c_2 is now of the order ~ 1, which can be attributed to the additional data for low Ha, as discussed in section 3.2. Only c_4 is much smaller than the other parameters, though even then it can become relevant at high Ha, since it appears in the term $c_4 Ha^3$ of (3.18). Like for c_2, it is expected that the value of c_4 can be better determined once data for very high $Ha \gtrsim 5 \times 10^4$ are available for the fitting procedure (see figure 3.2). The relative uncertainties of the parameters remain high, exceeding 100% except for c_6 and Re^*.

The values for Nu and Re resulting from the revised parameters (5.17) for $Pr = 0.025$ are plotted over the (Ra, Ha) phase space in figure 5.23. The general shape of the functions
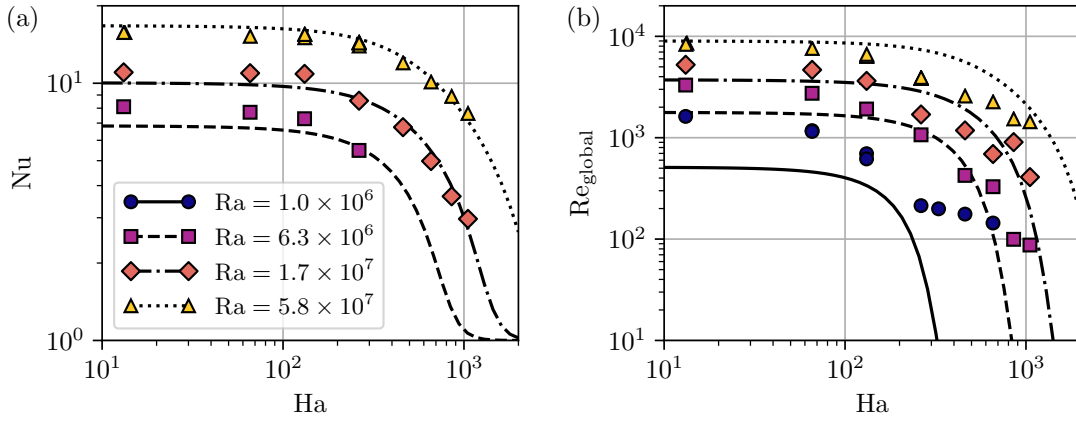
Figure 5.24.: Comparison of (a) Nu and (b) $\mathrm{Re_{global}}$ (markers) with the revised model (5.17) (lines). The values are plotted over Ha for selected Ra.

$\mathrm{Nu(Ra, Ha)}$ and $\mathrm{Re(Ra, Ha)}$ are similar to the initial results in figure 3.1. The largest difference is caused by the omission of the BL crossover. The Nusselt and Reynolds numbers do not show the increase at low Ha that was present in the initial results, but monotonically decrease for increasing Ha. This can be seen more clearly in figure 5.24(a), where the calculated Nusselt number is compared with the present experimental values. Similar to the initial fit (figure 5.22(a)), the model closely matches the Nusselt number for $\mathrm{Ha} > 200$. With the revised model, the range $\mathrm{Ha} < 200$ is better represented than previously. The model now approaches constant values for $\mathrm{Ha} \to 0$ which are close to their corresponding experimental results. The Reynolds numbers of the model (figure 5.24(b)) now match the experimental results better in magnitude for $\mathrm{Ra} \gtrsim 10^7$ but show a trend to increasingly underestimate the real values for decreasing Ra. The shape of the curves $\mathrm{Re(Ha)}$ still do not sufficiently reproduce the experimental trend. The model generates a much slower descend of Re for small Ha and a much steeper decline once Ha approaches the Chandrasekhar limit.

The experimental data of the other two experimental publications used in the model fit are compared to the theoretical results in figure 5.25. Plotted are Nusselt numbers over the Ra for selected Ha. The model agrees very well the experiments by King and Aurnou [74] except for the lowest and highest Ha (figure 5.25(a)). At $\mathrm{Ha} = 98$ the experimental data decay more slowly with respect to Ra than the model and coincide only at the highest $\mathrm{Ra} \sim 5 \times 10^7$. For $\mathrm{Ha} = 994$, the model fits the experiment well for $\mathrm{Ra} > 2 \times 10^7$. At the onset of convection $\mathrm{Ra_c} = 10^7$, the experimental values of $\mathrm{Nu} \sim 2$. Since the transition towards $\mathrm{Nu} = 1$ in the model is fixed at $\mathrm{Ra_c}$ this kind of result cannot be reproduced.

The data of Cioni et al. [71] are well fitted by the model for $\mathrm{Ra} \gtrsim 2 \times 10^8$ (figure 5.25(b)). The data at $\mathrm{Ha} = 850$ are slightly overestimated. However, the results by King and Aurnou [74] at nearly the same $\mathrm{Ha} = 994$ are matched very well for these Ra. Consequently this deviation can be attributed to experimental uncertainties. While the data at $\mathrm{Ha} = 994$ by King and Aurnou [74] suggests that the convection onset should shift to smaller Ra, the results for $\mathrm{Ha} = 1414$ and 1982 by Cioni et al. [71] imply that the transition in the model should happen at higher Ra.
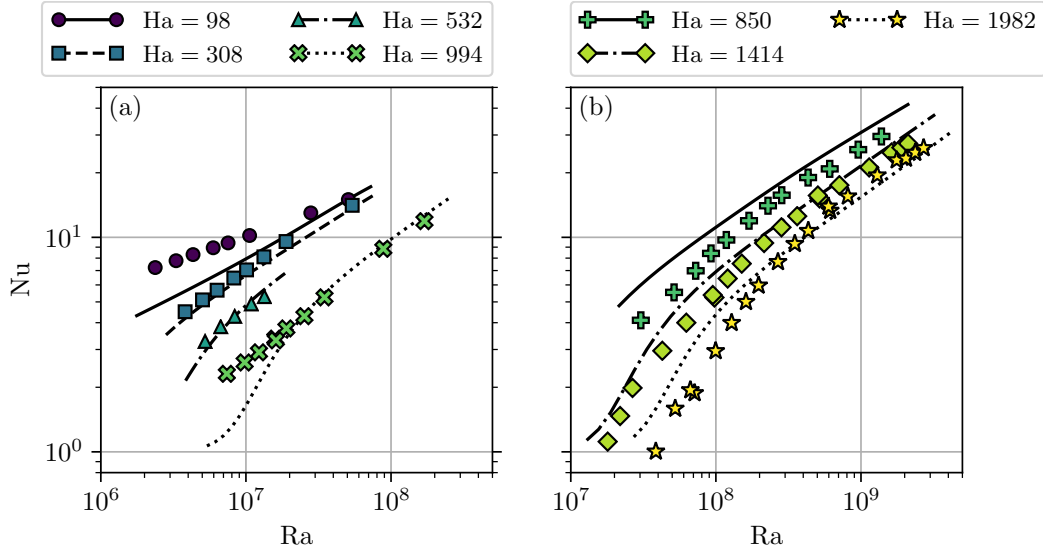
Figure 5.25.: Comparison of the revised model (5.17) (lines) with the data by (a) King and Aurnou [74] and (b) Cioni et al. [71] (markers). Shown are Nu over Ra for selected Ha.

Again, such inconsistencies in the data indicate that these deviations of the model are within the experimental accuracy.

Overall, the model reproduces the relation of the Nusselt number with Ra and Ha. The shape of the $\mathrm{Re}(\mathrm{Ra}, \mathrm{Ha})$ function matches the experiments less accurately. The following section reviews possible adjustments which could improve the performance of the model in future revisions.

5.4.3. Outlook

The above revisions of the model have improved the theoretical results and the addition of further experimental data allowed for more accurate determination of the model parameters. A number of improvements are still possible.

The assumptions and estimates made in the model can be validated using numerical simulations [75–77]. Similar to how the BL crossover was removed for small Pr due to the comparison with experimental and numerical results, other parts of the model could be revised and adjusted to better represent the actual physical mechanisms in magnetoconvection. For example, the onset of convection is so far enforced by a static transition function whose shape is not physically motivated. As such, the scaling of the model close to the critical Hartmann or Rayleigh number will always lack physical meaning.

The currently largest issue of the model is the inadequate reproduction of the Reynolds number scaling. On the one hand, this could indicate that some mechanisms of RBC magnetoconvection are not yet accurately represented in the model. One such mechanism could be the Nusselt number staying at a nearly constant level for the whole LSC regime while the flow slows down overall due to the suppression of turbulent fluctuations (see section 5.3). On the other hand, it might point towards a bias within the fitting procedure. In the current approach, data sets of $(\mathrm{Nu}, \mathrm{Ra}, \mathrm{Ha}, \mathrm{Pr})$

alone determine the shape of the resulting functions and the Reynolds number data is only used to adjusts a correction factor (see section 3.1.2). This has its basis in the more abundant availability of experimental data of the Nusselt number. The current experiment, however, provides data for both Nu and Re. This opens the possibility to fit both model equations (3.18) and (3.17) to a full data set $(\mathrm{Nu}, \mathrm{Re}, \mathrm{Ra}, \mathrm{Ha}, \mathrm{Pr})$ simultaneously. Instead of being reduced to a single factor, the Reynolds number data could then fully contribute to finding model parameters that fit both Nu and Re best.

Besides reviewing and improving the current model, extensions to other parameter spaces can be considered as well. Lim et al. [77] proposed a model for the viscous boundary layer that interpolates between the case of $\mathrm{Ha} = 0$ (a Prandtl–Blasius type BL in the GL theory) and the case of $\mathrm{Ha} \gg 1$ (a Hartmann layer in the present model). Including such an approach could extend the applicability of the present model towards smaller Ha or even fully bridge the gap to the GL theory at $\mathrm{Ha} = 0$. Another possible extension of the model concerns the Prandtl number. With recently published simulations at $\mathrm{Pr} = 1$ [76] and $\mathrm{Pr} = 8$ [77] the differences of low- and intermediate Pr could be investigated and potentially included in the model. A first example of such an extension was discussed in section 5.4.1, where the BL crossover was excluded from the low-Pr model. Its effect of increasing the Nusselt number at low Ha could become relevant for higher-Pr cases.

6. Summary and outlook

In this study, the interaction of thermal convection flows in liquid metals with magnetic fields was investigated. Two opposing aspects – unaffected flows for inductive measurement techniques and strongly altered flows in magnetoconvection – were considered.

It was shown that local Lorentz force velocimetry can be applied to convective flows for the example of a vertical convection system. The small force magnitudes of the order of µN could be measured using a high precision interference optical force sensor. These small forces are the result of slow velocities $\lesssim 10\,\mathrm{mm\,s^{-1}}$ and the small fluid volume penetrated by the magnetic field. The latter is not well defined and depends on the distribution of the magnetic field, the container geometry, and the (generally unknown) velocity field of the flow. To rectify this issue, an analytical solution for the total Lorentz force induced in the flow was derived. Based on this solution, a model for the penetration depth of the local Lorentz force velocimeter was developed which is independent of the flow field under consideration. The simplifying assumptions made in these calculation allow the model to be applied to a wide variety of set-ups. An extension to specific flow fields is easily possible. These theoretical results were used to calculate the interaction parameter N of the system. The well known threshold of $N = 1$ predicts the transition from the regime of an unaffected flow towards the regime of an altered flow. This result is of importance for the design of not just Lorentz force velocimetry, but all inductive measurement systems that use localised magnetic fields.

The case of strong magnetic fields, which changes the flow structure of thermal convection significantly, was investigated for the system of Rayleigh-Bénard magnetoconvection in a vertical magnetic field. An experimental set-up was constructed which allowed the observation and reconstruction of the large-scale flow by employing a combination of temperature measurements and ultrasound Doppler velocimetry. The reference case of turbulent Rayleigh-Bénard convection without an applied magnetic field revealed the presence of a large-scale circulation, which is well known from experiments in water. The short-term dynamics of the sloshing and torsion mode were found to be much more intense for liquid metals in terms of their frequency and amplitude. An in depth investigation of the flow progression in the convection cell revealed a consistent asymmetry of the flow structure over the whole accessible parameter range. The measured heat transport was found to be consistent with previous experimental, numerical and theoretical results. The calculations of multiple Reynolds numbers illustrated the crucial dependence of the momentum transport on the specific flow area probed by measurements, as well as the measurement method itself.

By addition of a vertical magnetic field, the above system was extended by another dimension in its parameter space which introduced a rich variety of different flow regimes. At low magnetic field strengths, the initial large-scale circulation persisted, but the turbulent fluctuations and oscillations were continually suppressed until the one-roll structure had become nearly two-dimensional. The decrease in velocity magnitude finally leads to the breakdown of the turbulent

flow structure and the transition into a cellular flow state that displays various numbers of convection cells. The destabilising effect of the electrically insulating side walls was demonstrated when the magnetic field strength was increased beyond the theoretical onset of convection for a horizontally infinite fluid layer. While the flow in the centre of the cell was nearly completely inhibited, fluid motion could be detected near the side walls, confirming the results of previous numerical simulations and theoretical predictions. Heat and momentum transfer were found to follow a distinct scaling law with increasing magnetic field. The Reynolds number slowly decreased over the one-roll regime and transition into a quicker descent once the cellular regime was reached. There, the flow strength was found to be dominated by the damping effect of Joule dissipation while the kinematic viscosity could be neglected. Contrary to the Reynolds number, the Nusselt number stayed at a nearly constant value while the one-roll structure of the flow persisted. This was attributed to the increased coherence of the flow by the suppression of turbulent fluctuations. Only once the onset of the cellular regime was reached did the heat transport start to decrease rapidly.

To predict the above behaviour of heat and momentum transport in magnetoconvection, a theoretical model based on concepts of Grossmann-Lohse theory was developed for the low-Prandtl-number regime. Comparisons between theory and experiments allowed the identification of relevant physical mechanisms. Specifically, it was found that a crossing of the thermal and viscous boundary layers is of no importance in liquid metals, but may become significant for fluids of intermediate or high Prandtl numbers. These revisions to the model displayed significant improvements which were further enhanced by the extended range of experimental data used to fit the free model parameters. Still, a number of propositions were made that could advance the accuracy of the theory. The joint measurement of heat and momentum transport in the present experiments may allow a revision of the fitting process to better capitalise on the full range of data available. Recent numerical simulations [75–77] opened the possibility to directly verify the assumptions and approximations made in the theory. These simulations also provide data for magnetoconvection at higher Prandtl numbers, granting the possibility of extending the model towards other fluids than liquid metals. Another promising extension concerns the low-Hartmann number regime. Bridging the gap between the current model for magnetoconvection and the classic Grossmann-Lohse theory would increase the range of applicability considerably.

The present experiments gave a broad overview of the richness of flow structures caused by a vertical magnetic field applied to Rayleigh-Bénard convection. These measurements can be seen as a starting point for future investigations into specific details of the flow regimes. Due to its large extend, the sampling of the parameter space had to be relatively coarse. The transitions between different flow states could be located much more accurately in future experiments and critical parameters determining their position may be derived accordingly. Another aspect not explored in the present experiments is the influence of pattern selection due to the history of the flow. The way the experiment is conducted may have a profound influence on the resulting flow structure at the same parameters this implying the existence of hysteresis effects. Examples are the approach of a measurement point from low or high Rayleigh or Hartmann numbers, or the speed at which control parameters are changed.

Overall, the present study provided a large number of insightful results on the topic of magnetoconvection. Still, many questions remain to be answered and several new ones have been raised during the course of this thesis, prompting the possibility of interesting future investigations.

Appendix

A. The onset of magnetoconvection

The onset of magnetoconvection is considered for an Rayleigh-Bénard system with infinite horizontal extent ($\Gamma \to \infty$) and a uniform vertical magnetic field. The top and bottom boundaries are assumed to be rigid and electrically insulating. The linear stability analysis for stationary convection was solved by Chandrasekhar [5]. The result is presented here.

The thermal driving is characterised by the Rayleigh number Ra (1.2) and the strength of the magnetic field is represented by the Chandrasekhar number

$$\mathrm{Q} = B^2 H^2 \frac{\sigma}{\rho \nu} = \mathrm{Ha}^2 \,. \tag{A.1}$$

The Prandtl number Pr of the fluid does not play into the calculation. The horizontal wavenumber k of the first unstable velocity mode is normalised by the layer height $\tilde{k} = kH$. A characteristic equation $\mathrm{Ra}(\tilde{k}, \mathrm{Q})$ is calculated from the vanishing determinant

$$\det\left(A_{mn}\right) = \det\left(\frac{1}{2}\left[\frac{c_{2m+1}}{\tilde{k}^2 \mathrm{Ra}} - \gamma_{2m+1}\right]\delta_{mn} - (m|n)\right) = 0\,, \quad m, n \in \mathbb{N}_0\,. \tag{A.2}$$

The matrix elements A_{mn} are determined from the following quantities:

$$c_i = i^2 \pi^2 + \tilde{k}^2\,, \tag{A.3}$$

$$\gamma_i = \left[c_i^2 + i^2 \pi^2 \mathrm{Q}\right]^{-1}\,, \tag{A.4}$$

$$(m|n) = -2\pi^2 \lambda_m \lambda_n \frac{\sqrt{\mathrm{Q}(\mathrm{Q} + 4\tilde{k}^2)}}{q_+ \tanh(q_+/2) - q_- \tanh(q_-/2)}\,, \tag{A.5}$$

$$\lambda_m = (-1)^m (2m+1)\gamma_{2m+1}\,, \tag{A.6}$$

$$q_\pm = \frac{1}{2}\left(\sqrt{\mathrm{Q} + 4\tilde{k}^2} \pm \sqrt{\mathrm{Q}}\right)\,. \tag{A.7}$$

δ_{mn} is the Kronecker-delta. To calculate $\mathrm{Ra}(\tilde{k}, \mathrm{Q})$, (A.2) has to be solved numerically for Ra with a limited number of rows and columns, i.e. $m, n = 0, \dots, p$. The higher $p \in \mathbb{N}$, the more precise the result will be. For a given Q the characteristic equation has to be minimized in terms of $\tilde{k}$. The resulting minimal value is the critical Rayleigh number $\mathrm{Ra_c}(\mathrm{Q})$ at a critical wavenumber $\tilde{k}_c$.

If a fixed value of Ra is given, the corresponding critical Chandrasekhar number $\mathrm{Q_c}$ is calculated by numerically solving

$$\mathrm{Ra_c}(\mathrm{Q}) - \mathrm{Ra} = 0\,. \tag{A.8}$$

The value of Q satisfying this equation is $\mathrm{Q_c}(\mathrm{Ra})$.

The solutions $\mathrm{Ra_c}(\mathrm{Q})$ and $\mathrm{Q_c}(\mathrm{Ra})$ approach the Chandrasekhar limit (1.42) and (1.43) for large $\mathrm{Q} \gtrsim 10^4$ and $\mathrm{Ra} \gtrsim 2 \times 10^5$, respectively.

B. Calculation of the Lorentz force

Lorentz force velocimetry (LFV) heavily relies on the linear scaling of the induced forces with the fluid velocity. This dependence is easily derived from dimensional arguments (see section 1.4.1). An exact calculation of the Lorentz force is much more complicated and has to take into account the vessel geometry, the magnetic field distribution and the shape of the velocity field. Most often, this is achieved by numerical simulations, which solve the induction equations for a given velocity field. In the following section B.1, a closed analytical solution for the Lorentz force will be derived. Afterwards, in section B.2, the result is applied to a simplified problem and used to estimate the penetration depth of local LFV (LLFV).

The following calculations assume that the quasistatic approximation applies, i.e. the magnetic field and the flow field do not influence each other. This is the limit of low interaction parameters $N \ll 1$ and magnetic Reynolds numbers $\mathrm{Rm} \ll 1$.

B.1. General case

As described in section 1.4.1, the force on the magnet system of the LLFV can be calculated from the induced eddy currents $\boldsymbol{j}$ in the fluid. Combining equations (1.45), (1.31), and (1.38) gives

$$\boldsymbol{F}_{\mathrm{L}} = \sigma \int_V \left[\boldsymbol{v}(\boldsymbol{r}) \times \boldsymbol{B}(\boldsymbol{r}) - \boldsymbol{\nabla}\varphi(\boldsymbol{r}) \right] \times \boldsymbol{B} \, \mathrm{d}V \,. \tag{B.1}$$

The integral is taken over the fluid volume V. $\boldsymbol{B}$ is the externally applied magnetic field, i.e. its source is outside of V. $\boldsymbol{v}$ is the velocity field and σ the electrical conductivity of the fluid. φ is the electric scalar potential. The second term of the integrand in (B.1) can be transformed into a surface integral over the closed surface S of V using $\boldsymbol{\nabla} \times (\varphi\boldsymbol{B}) = (\boldsymbol{\nabla}\varphi) \times \boldsymbol{B}$ inside V and applying Stokes' theorem

$$\boldsymbol{F}_{\mathrm{L}} = \sigma \int_V \left(\boldsymbol{v}(\boldsymbol{r}) \times \boldsymbol{B}(\boldsymbol{r}) \right) \times \boldsymbol{B}(\boldsymbol{r}) \, \mathrm{d}V - \sigma \oint_S \varphi(\boldsymbol{s}) \left(\boldsymbol{n}(\boldsymbol{s}) \times \boldsymbol{B}(\boldsymbol{s}) \right) \mathrm{d}S \,. \tag{B.2}$$

Here, $\boldsymbol{n}(\boldsymbol{s})$ is the surface normal vector at a point $\boldsymbol{s} \in S$.

The scalar potential φ is calculated from the Poisson equation (1.39). This partial differential equation can be transformed into an integral equation by applying Green's second theorem, which states for two scalar fields Ψ and Θ [109]

$$\int_V \left[\Psi \boldsymbol{\nabla}^2 \Theta - \Theta \boldsymbol{\nabla}^2 \Psi \right] \mathrm{d}V = \oint_S \left[\Psi \boldsymbol{n} \cdot \boldsymbol{\nabla}\Theta - \Theta \boldsymbol{n} \cdot \boldsymbol{\nabla}\Psi \right] \mathrm{d}S \,. \tag{B.3}$$

B. Calculation of the Lorentz force

Ψ is now identified with φ and Θ with the Green's function G of the Laplace operator. $G \equiv G(\boldsymbol{r}, \boldsymbol{r}')$ is defined as the solution of $\boldsymbol{\nabla}'^2 G(\boldsymbol{r}, \boldsymbol{r}') = \delta(\boldsymbol{r} - \boldsymbol{r}')$ for two spatial vectors $\boldsymbol{r}$ and $\boldsymbol{r}'$. $\boldsymbol{\nabla}'$ denotes the nabla operator with respect to $\boldsymbol{r}'$ and δ is the Dirac delta function. G is given by

$$G(\boldsymbol{r}, \boldsymbol{r}') = -\frac{1}{4\pi|\boldsymbol{r} - \boldsymbol{r}'|}. \tag{B.4}$$

Inserting $\Psi = \varphi$, $\Theta = G$, and (B.4) into (B.3) results in

$$\varphi(\boldsymbol{r}) = -\int_V \frac{\boldsymbol{\nabla}'^2 \varphi(\boldsymbol{r}')}{4\pi|\boldsymbol{r} - \boldsymbol{r}'|}\,\mathrm{d}V' - \oint_S \left[\varphi(\boldsymbol{s}')\frac{\boldsymbol{n}(\boldsymbol{s}') \cdot (\boldsymbol{r} - \boldsymbol{s}')}{4\pi|\boldsymbol{r} - \boldsymbol{s}'|^3} - \frac{\boldsymbol{n}(\boldsymbol{s}') \cdot \boldsymbol{\nabla}'\varphi(\boldsymbol{s}')}{4\pi|\boldsymbol{r} - \boldsymbol{s}'|}\right]\mathrm{d}S'. \tag{B.5}$$

With the Poisson equation (1.39) for φ and its boundary condition (1.40) this becomes

$$\varphi(\boldsymbol{r}) = \int_V \frac{(\boldsymbol{v}(\boldsymbol{r}') \times \boldsymbol{B}(\boldsymbol{r}')) \cdot (\boldsymbol{r} - \boldsymbol{r}')}{4\pi|\boldsymbol{r} - \boldsymbol{r}'|^3}\,\mathrm{d}V' - \oint_S \varphi(\boldsymbol{s}')\frac{\boldsymbol{n}(\boldsymbol{s}') \cdot (\boldsymbol{r} - \boldsymbol{s}')}{4\pi|\boldsymbol{r} - \boldsymbol{s}'|^3}\,\mathrm{d}S'. \tag{B.6}$$

Equation (B.2) shows, that φ only has to be known on the fluid surface. As a result, the surface integral in (B.6) exhibits a singularity for $\boldsymbol{r} = \boldsymbol{s}'$. This can be circumvented by considering the limit $\boldsymbol{s}' \to \boldsymbol{r}$ [110, 111], which results in

$$\varphi(\boldsymbol{s}) = \int_V \frac{(\boldsymbol{v}(\boldsymbol{r}') \times \boldsymbol{B}(\boldsymbol{r}')) \cdot (\boldsymbol{s} - \boldsymbol{r}')}{2\pi|\boldsymbol{s} - \boldsymbol{r}'|^3}\,\mathrm{d}V' - {}^*\!\!\oint_S \varphi(\boldsymbol{s}')\frac{\boldsymbol{n}(\boldsymbol{s}') \cdot (\boldsymbol{s} - \boldsymbol{s}')}{2\pi|\boldsymbol{s} - \boldsymbol{s}'|^3}\,\mathrm{d}S'. \tag{B.7}$$

${}^*\!\!\int$ stands for the Cauchy principal value of an integral. (B.7) is an implicit integral equation, since φ itself appears in the surface integral on the right-hand side. Solving the equation for arbitrary shapes of V poses a complex problem. One approach is to apply an iterative scheme [110]

$$\varphi(\boldsymbol{s}) = \sum_{i=0}^{\infty} \varphi^{(i)}(\boldsymbol{s}), \tag{B.8}$$

where

$$i = 0: \qquad \varphi^{(0)}(\boldsymbol{s}) = \frac{1}{2\pi}\int_V \frac{(\boldsymbol{v}(\boldsymbol{r}') \times \boldsymbol{B}(\boldsymbol{r}')) \cdot (\boldsymbol{s} - \boldsymbol{r}')}{|\boldsymbol{s} - \boldsymbol{r}'|^3}\,\mathrm{d}V', \tag{B.9}$$

$$i \geq 1: \qquad \varphi^{(i)}(\boldsymbol{s}) = -\frac{1}{2\pi}{}^*\!\!\oint_S \varphi^{(i-1)}(\boldsymbol{s}^{(i)})\frac{\boldsymbol{n}(\boldsymbol{s}^{(i)}) \cdot (\boldsymbol{s} - \boldsymbol{s}^{(i)})}{|\boldsymbol{s} - \boldsymbol{s}^{(i)}|^3}\,\mathrm{d}S^{(i)}. \tag{B.10}$$

The first term $\varphi^{(0)}$ in (B.8) is simply the volume integral from (B.7). The additional retroaction of φ onto itself is then successively added by the following terms $\varphi^{(i \geq 1)}$.

$\varphi^{(i-1)}$ in (B.10) can be expanded by applying (B.10) $i - 1$ times and (B.9) once. The volume integral from (B.9) is then interchanged with the surface integrals from (B.10). This gives $\varphi^{(i)}$ as

$$\varphi^{(i)}(\boldsymbol{s}) = \int_V \left(\boldsymbol{v}(\boldsymbol{r}') \times \boldsymbol{B}(\boldsymbol{r}')\right) \cdot \boldsymbol{\Phi}^{(i)}(\boldsymbol{s}, \boldsymbol{r}')\,\mathrm{d}V', \tag{B.11}$$

where

$$i = 0 : \qquad \mathbf{\Phi}^{(0)}(\boldsymbol{s}, \boldsymbol{r}') = \frac{1}{2\pi} \frac{(\boldsymbol{s} - \boldsymbol{r}')}{|\boldsymbol{s} - \boldsymbol{r}'|^3} \,, \tag{B.12}$$

$$i \geq 1 : \qquad \mathbf{\Phi}^{(i)}(\boldsymbol{s}, \boldsymbol{r}') = -\frac{1}{2\pi} \overset{*}{\oint_S} \mathbf{\Phi}^{(i-1)}(\boldsymbol{s}^{(i)}, \boldsymbol{r}') \frac{\boldsymbol{n}(\boldsymbol{s}^{(i)}) \cdot (\boldsymbol{s} - \boldsymbol{s}^{(i)})}{|\boldsymbol{s} - \boldsymbol{s}^{(i)}|^3} \, \mathrm{d}S^{(i)} \,. \tag{B.13}$$

By applying (B.11) to (B.8), the electric potential can now be written as

$$\varphi(\boldsymbol{s}) = \int_V \left(\boldsymbol{v}(\boldsymbol{r}') \times \boldsymbol{B}(\boldsymbol{r}') \right) \cdot \mathbf{\Phi}(\boldsymbol{s}, \boldsymbol{r}') \, \mathrm{d}V' \,, \tag{B.14}$$

$$\mathbf{\Phi}(\boldsymbol{s}, \boldsymbol{r}') = \sum_{i=0}^{\infty} \mathbf{\Phi}^{(i)}(\boldsymbol{s}, \boldsymbol{r}') \,. \tag{B.15}$$

The vector field $\mathbf{\Phi}$ has the unit m^{-2} and is purely geometry-dependent. This means it is a constant for any given set-up, without regard to the magnetic system or the flow field present in the fluid.

This solution of φ can now be inserted into (B.2). By renaming the integration variables $\boldsymbol{r}' \to \boldsymbol{r}$ in (B.14) and $\boldsymbol{s} \to \boldsymbol{s}'$ in the surface integral of (B.2) and interchanging the volume and surface integrals, one finally reaches

$$\boldsymbol{F}_{\mathrm{L}} = \sigma \int_V \left[\left(\boldsymbol{v}(\boldsymbol{r}) \times \boldsymbol{B}(\boldsymbol{r}) \right) \times \boldsymbol{B}(\boldsymbol{r}) - \left(\boldsymbol{v}(\boldsymbol{r}) \times \boldsymbol{B}(\boldsymbol{r}) \right) \underline{\mathbf{K}}(\boldsymbol{r}) \right] \mathrm{d}V \,. \tag{B.16}$$

$\underline{\mathbf{K}}$ is a matrix, which only depends on the geometry and the magnetic field of the present problem:

$$\underline{\mathbf{K}}(\boldsymbol{r}) = \oint_S \mathbf{\Phi}(\boldsymbol{s}', \boldsymbol{r}) \otimes \left(\boldsymbol{n}(\boldsymbol{s}') \times \boldsymbol{B}(\boldsymbol{s}') \right) \mathrm{d}S' \,. \tag{B.17}$$

The operator $\otimes$ denotes the tensor product or dyadic product of two vectors.

Equations (B.16) to (B.17) give a closed solution for the cumulative Lorentz force acting on the fluid. Formula (B.16) can be further condensed by writing the integrand in Einstein summation convention and transforming it into a product of the velocity vector and a sensitivity matrix $\underline{\mathbf{W}}$

$$\boldsymbol{F}_{\mathrm{L}} = \int_V \underline{\mathbf{W}}(\boldsymbol{r}) \boldsymbol{v}(\boldsymbol{r}) \, \mathrm{d}V \,, \tag{B.18}$$

$$\left(\underline{\mathbf{W}}(\boldsymbol{r}) \right)_{ij} \equiv W_{ij} = \sigma \left(B_i(\boldsymbol{r}) B_j(\boldsymbol{r}) - \delta_{ij} B_k(\boldsymbol{r})^2 - \varepsilon_{jkl} B_k(\boldsymbol{r}) K_{li}(\boldsymbol{r}) \right) \,. \tag{B.19}$$

δ_{ij} is the Kronecker delta, ε_{jkl} the Levi-Civita symbol and K_{li} are the elements of $\underline{\mathbf{K}}$. (B.18) clearly shows the linear dependency of the Lorentz force on the flow velocity, since the matrix $\underline{\mathbf{W}}$ is only dependent on the shape of the fluid surface S, the electrical conductivity σ and the magnetic field $\boldsymbol{B}$. This makes $\underline{\mathbf{W}}$ a characteristic constant of a given set-up which only has to be calculated once and is valid for any kind of flow field. It represents the contribution of a velocity component at any point in the fluid to a final force component. In practice, the calculation of $\boldsymbol{F}_{\mathrm{L}}$ with equation (B.18) is often analytically impossible and numerically difficult, since it contains a volume integral and $m + 1$ surface integrals, where m is the cut-off value of the infinite sum in (B.15). For fine grid resolutions in more complex geometries this would lead to an excessive increase of computation time compared to other common numerical methods. However, for certain simple problems, the effort in calculating $\boldsymbol{F}_{\mathrm{L}}$ can be strongly reduced. This is demonstrated in the next section.

B.2. The penetration depth of LLFV

An important information for the usage of LLFV is which part of the fluid flow has the largest influence on the final measurement signal. The full answer to this question depends on the investigating magnetic field, the fluid properties, the geometry of the experiment and the velocity field of the liquid. While the first three properties of the set-up are generally known, the last one is an unknown quantity, as it is supposed to be measured by the LLFV.

In the previous section the Lorentz force was separated into the flow field and a sensitivity matrix, which is characteristic for the experimental set-up. In the following, this sensitivity matrix will be used to calculate a characteristic penetration depth down to which the LLFV can investigate the fluid. In order to reduce the complexity of the calculations, approximations are made for the geometry and velocity field of the problem. The magnetic field will be required to exhibit certain symmetries, but can otherwise be of arbitrary shape.

The considered fluid volume covers the lower infinite half space $V = \{ \boldsymbol{r} \in \mathbb{R}^3 : z \leq 0 \}$. This is a suitable approximation for any experiment, where the magnet system of the LLFV is much smaller than the fluid volume and is positioned above a plane surface. It is assumed that $\varphi(\boldsymbol{s})$ goes to zero for $|\boldsymbol{s}| \to \infty$. The surface S is the x-y-plane at $z = 0$ with a normal vector $\boldsymbol{n} = \boldsymbol{e}_z$. As a result, the surface integral in (B.13) vanishes for all $i \geq 1$ since $\boldsymbol{s}, \boldsymbol{s}^{(i)} \in S$ do not have a z-component, and thus $\boldsymbol{n} \cdot (\boldsymbol{s} - \boldsymbol{s}^{(i)}) = 0$. This reduces the infinite sum in (B.15) to only the first element: $\boldsymbol{\Phi} = \boldsymbol{\Phi}^{(0)}$. Consequently, the elements of $\underline{\mathbf{K}}$ become

$$K_{li} = \frac{1}{2\pi} \int_S \frac{s'_l - r_l}{|\boldsymbol{s}' - \boldsymbol{r}|^3} \left[-\delta_{ix} B_y(\boldsymbol{s}') + \delta_{iy} B_x(\boldsymbol{s}') \right] \mathrm{d}S' \, . \tag{B.20}$$

In the next step, the velocity field is simplified. The investigated flow is assumed to be stationary, to move only in x-direction and to depends only on the depth z

$$\boldsymbol{v}(\boldsymbol{r}) = v_x(z) \boldsymbol{e}_x \, . \tag{B.21}$$

This is an appropriate approximation for most forced convection cases, such as channel flow, or if the magnet system is sufficiently small compared to the large-scale flow structures. The product $\underline{\mathbf{W}} \boldsymbol{v}$ becomes

$$\underline{\mathbf{W}}(\boldsymbol{r}) \boldsymbol{v}(\boldsymbol{r}) = \boldsymbol{e}_i W_{ix}(\boldsymbol{r}) v_x(z) \equiv v_x(z) \boldsymbol{w}(\boldsymbol{r}) \, , \tag{B.22}$$

$$(\boldsymbol{w})_i \equiv w_i = W_{ix} = \sigma \left(B_x B_i - \delta_{ix} B_k^2 - B_y K_{zi} + B_z K_{yi} \right) \, . \tag{B.23}$$

Since the velocity profile is independent of x and y, the respective integrations of the volume integral in (B.18) only apply to $\boldsymbol{w}$. This gives the equation

$$\boldsymbol{F}_{\mathrm{L}} = \int_{-\infty}^{0} v_x(z) \tilde{\boldsymbol{w}}(z) \, \mathrm{d}z \, , \tag{B.24}$$

with

$$\tilde{\boldsymbol{w}}(z) = \int_{-\infty}^{\infty} \int_{-\infty}^{\infty} \boldsymbol{w}(\boldsymbol{r}) \, \mathrm{d}x \, \mathrm{d}y = \tilde{w}_x(z)\boldsymbol{e}_x + \tilde{w}_y(z)\boldsymbol{e}_y + \tilde{w}_z(z)\boldsymbol{e}_z \,, \tag{B.25}$$

$$\tilde{w}_x(z) = -\sigma \int_{-\infty}^{\infty} \int_{-\infty}^{\infty} \left[B_y(\boldsymbol{r})^2 + B_z(\boldsymbol{r})^2 + \int_S \frac{B_y(\boldsymbol{r})z + B_z(\boldsymbol{r})(y'-y)}{2\pi|\boldsymbol{s}'-\boldsymbol{r}|^3} B_y(\boldsymbol{s}') \, \mathrm{d}S' \right] \mathrm{d}x \, \mathrm{d}y \,,$$

$$\tilde{w}_y(z) = \sigma \int_{-\infty}^{\infty} \int_{-\infty}^{\infty} \left[B_x(\boldsymbol{r})B_y(\boldsymbol{r}) + \int_S \frac{B_y(\boldsymbol{r})z + B_z(\boldsymbol{r})(y'-y)}{2\pi|\boldsymbol{s}'-\boldsymbol{r}|^3} B_x(\boldsymbol{s}') \, \mathrm{d}S' \right] \mathrm{d}x \, \mathrm{d}y \,,$$

$$\tilde{w}_z(z) = \sigma \int_{-\infty}^{\infty} \int_{-\infty}^{\infty} B_x(\boldsymbol{r})B_z(\boldsymbol{r}) \, \mathrm{d}x \, \mathrm{d}y \,.$$

Next, a cubic permanent magnet is chosen for the magnetic system. It has a side length of $2l$ and a homogeneous magnetisation $\boldsymbol{M} = M\boldsymbol{e}_z$. Its edges are aligned with the coordinate system and its centre is positioned at $\boldsymbol{r}_\mathrm{m} = (0,0,h)$, with $h > l$. The magnetic field outside of the magnet is [112]

$$\boldsymbol{B}(\boldsymbol{r}) = -\frac{\mu_0 M}{4\pi} \hat{\boldsymbol{B}}(\boldsymbol{r} - \boldsymbol{r}_\mathrm{m}, \boldsymbol{r}') \Bigg|_{x',\,y',\,z'=-l}^{l} \,, \tag{B.26}$$

$$\hat{\boldsymbol{B}}(\boldsymbol{r}, \boldsymbol{r}') = \begin{pmatrix} \mathrm{Artanh}\left(\frac{y-y'}{|\boldsymbol{r}-\boldsymbol{r}'|}\right) \\ \mathrm{Artanh}\left(\frac{x-x'}{|\boldsymbol{r}-\boldsymbol{r}'|}\right) \\ -\arctan\left(\frac{(x-x')(y-y')}{(z-z')|\boldsymbol{r}-\boldsymbol{r}'|}\right) \end{pmatrix} \,.$$

This magnetic field exhibits the symmetries

$$B_x(-x,y,z) = -B_x(x,y,z) \,, \tag{B.27}$$

$$B_y(-x,y,z) = B_y(x,y,z) \,, \qquad B_z(-x,y,z) = B_z(x,y,z) \,. \tag{B.28}$$

With this, the terms B_xB_y and B_xB_z in (B.25) are antisymmetric with respect to the x-integration and vanish. The integrand of the surface integral of $\tilde{w}_y$ also vanishes under x- and x'-integration, when these symmetries are applied. Thus, $\tilde{w}_y = \tilde{w}_z = 0$ and the resulting Lorentz force $\boldsymbol{F}_L$ has only the x-component $F_{\mathrm{L},x}$ remaining. This last component can be further simplified by applying the symmetry

$$B_y(x,-y,z) = -B_y(x,y,z) \tag{B.29}$$

of the magnetic field with respect to the y-coordinate. It eliminates the first term of the surface integral in $\tilde{w}_x$ containing $B_y(\boldsymbol{r})z$, which vanishes under y- and y'-integration, analogous to the

$2l$	5		10		15	
h	d_{90}	d_{95}	d_{90}	d_{95}	d_{90}	d_{95}
7.5	7.0	10.6	–	–	–	–
10.0	9.6	14.5	9.3	14.0	–	–
12.5	12.1	18.1	12.2	18.2	11.4	17.5
15.0	14.5	22.0	14.7	22.2	14.0	21.7
17.5	17.2	25.8	17.3	26.0	17.1	25.7
20.0	19.7	29.3	19.7	29.3	19.7	29.3
25.0	24.6	36.0	24.3	35.8	24.6	36.1
30.0	28.9	41.7	28.6	41.5	28.9	41.8
35.0	33.2	47.0	32.8	46.5	32.9	46.7
40.0	40.6	54.5	36.6	50.7	36.8	51.4
45.0	44.2	58.7	39.8	54.3	40.1	55.1

Table B.1.: LLFV penetration depths d for different magnet sizes $2l$, vertical magnet positions h and contribution percentages 90 % (d_{90}) and 95 % (d_{95}). All values are given in mm.

surface integral of the $\tilde{w}_y$-component. The final solution for the total Lorentz force is

$$F_{\mathrm{L},x} = \int_{-\infty}^{0} v_x(z)\tilde{w}_x(z)\,\mathrm{d}z\,, \tag{B.30a}$$

$$\tilde{w}_x(z) = -\sigma \int_{-\infty}^{\infty}\int_{-\infty}^{\infty}\left[B_y(\boldsymbol{r})^2 + B_z(\boldsymbol{r})^2 + \int_S \frac{B_z(\boldsymbol{r})(y'-y)}{2\pi|\boldsymbol{s}'-\boldsymbol{r}|^3}B_y(\boldsymbol{s}')\,\mathrm{d}S' \right]\mathrm{d}x\,\mathrm{d}y\,. \tag{B.30b}$$

Since the velocity profile in an experiment is generally unknown, the sensitivity function $\tilde{w}_x$ can be used to characterize the penetration depth d of the flow measurement. The approach has been outlined in section 2.3: A relative contribution $\tilde{P}(z)$ towards the total Lorentz Force of the flow up to a depth z is calculated from $\tilde{w}_x$ (2.2). The penetration depth d is then defined by the depth, at which a certain percentage of the total Lorentz force is reached. Table B.1 lists the penetration depths d_{90} and d_{95} for the threshold percentages $\tilde{P}(-d_{90}) = 90\,\%$ and $\tilde{P}(-d_{95}) = 95\,\%$, respectively.

C. Power law fitting and error estimation

In thermal convection and a number of other branches of fluid mechanics, the determination of scaling laws of a quantity on one or multiple input variables is a common occurrence. Very often, power laws of the form

$$A \simeq c \, B^{\gamma} \tag{C.1}$$

are used to describe the dependence of a quantity A on a variable B. The pre-factor or amplitude c and the scaling exponent γ are either determined from theory or by fitting (C.1) to experimental or numerical data. The most common fitting procedures are least-squares approaches, which calculate the residuals between the data points A and the values of the fit A_{fit}, and minimise the sum of its squares $(A - A_{\text{fit}})^2$. The uncertainty of A, given by its standard deviation ΔA, can be incorporated into this fit method by e.g. normalising the residuals $((A - A_{\text{fit}})/\Delta A)^2$. Thus, measurement points of high uncertainty have a lower impact on the overall fit result. Any uncertainty of the input variable B, however, cannot be included.

Another fit algorithm is orthogonal distance regression (ODR) [113]. Here, the smallest distances between the fit function and the data points are minimised. This also includes the residuals of B in the minimisation calculation. A and B can potentially have very different magnitudes or even different units. In the former case, the larger quantity would dominate the fit calculation. In the latter case, the calculation would be impossible, since addition of different physical dimensions is not possible. One way to resolve both issues, is to use the standard deviations of A and B to normalise the data. This means, that ODR can only be applied, if the standard deviations for both quantities are known. If only one or neither of the uncertainties are known, a standard least-squares algorithm can be used.

Figure C.1 show the ODR power law fit (solid line) to the experimental data set $\mathrm{Re}_{\text{LSC}}(\mathrm{Ra})$ from section 4.3.2, i.e. $A = \mathrm{Re}_{\text{LSC}}$ and $B = \mathrm{Ra}$. The data is replotted from figure 4.13 and the fit gives values of $c = 9.66$ for the amplitude and $\gamma = 0.410$ for the exponent. Additionally, the ODR algorithm supplies standard deviations of the fit parameters $\Delta_{\text{ODR}}c = 0.40$ and $\Delta_{\text{ODR}}\gamma = 0.003$. Since the uncertainties of Ra are relatively small, a least-squares fit (which considers the Re_{LSC} uncertainties only) produces the same parameter values and uncertainties for this data set. Plotting power laws with exponents $\gamma + \Delta_{\text{ODR}}\gamma$ and $\gamma - \Delta_{\text{ODR}}\gamma$ in figure C.1 (dotted lines) indicates the variation of the exponent allowed by the ODR uncertainties. They show no visible deviation from the original fit line. However, from the error bars of the data it is clear, that power laws with much higher or lower exponents could be feasible. The ODR uncertainties are consequently not a good indicator of the possible ranges of exponents that are viable for the data.

In this thesis, a different approach is taken to estimate the uncertainty of the power law exponent and amplitude. The uncertainties $\Delta \mathrm{Re}_{\text{LSC}}$ and $\Delta \mathrm{Ra}$ are given by the standard deviation of the respective quantity and are assumed to be normally distributed. That means, the probability

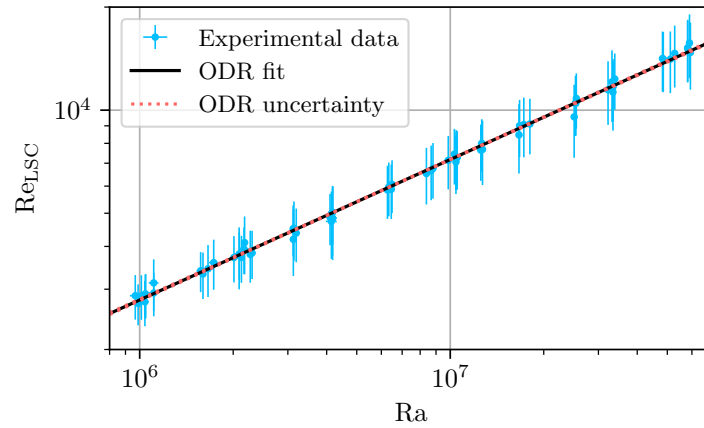Figure C.1.: ODR power law fit to the experimental data $\mathrm{Re}_{\mathrm{LSC}}(\mathrm{Ra})$ from figure 4.13. The uncertainty of the fitted exponent γ is shown as two dashed lines with fixed exponents $\gamma + \Delta_{\mathrm{ODR}}\gamma$ and $\gamma - \Delta_{\mathrm{ODR}}\gamma$.
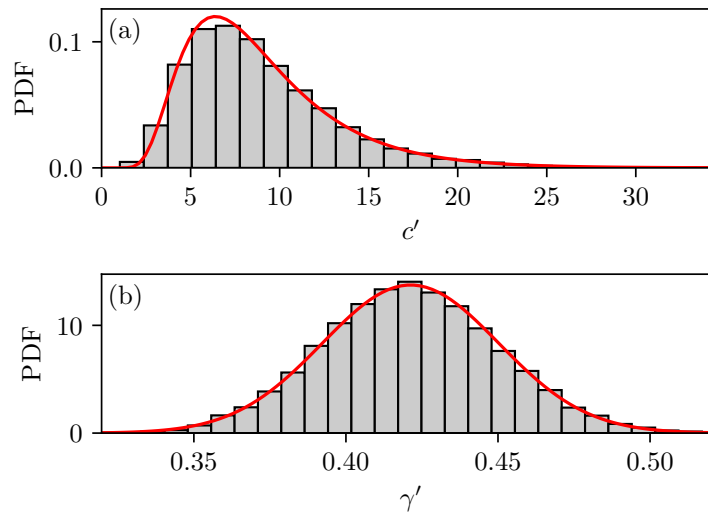

Figure C.2.: Probability density functions of (a) the amplitude c' and (b) the exponent γ' for 25 000 randomly generated data sets $(\mathrm{Ra}', \mathrm{Re}'_{\mathrm{LSC}})$. The red lines display (a) an inverse Gaussian distribution and (b) a Gaussian distribution with mean and standard deviation of the respective data.
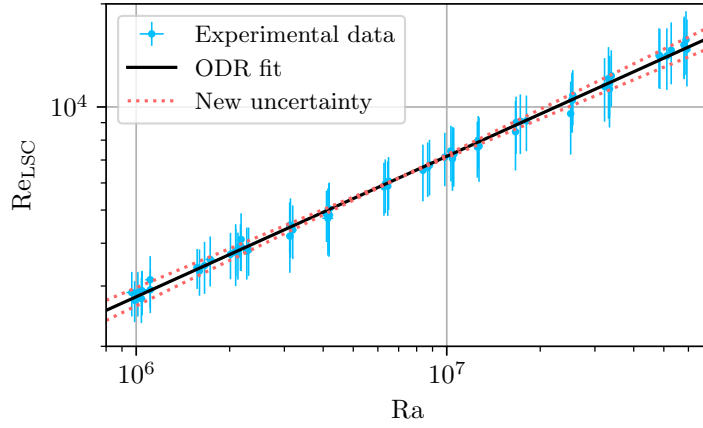
Figure C.3.: ODR power law fit to the experimental data $Re_{LSC}(Ra)$ from figure 4.13 with the alternative uncertainty calculation. The new uncertainty (C.2) of the fitted exponent γ is shown as two dashed lines with fixed exponents $\gamma + \Delta\gamma$ and $\gamma - \Delta\gamma$.

density function (PDF) of the quantities are Gaussian distributions with mean Re_{LSC} and Ra, and standard deviations ΔRe_{LSC} and ΔRa, respectively. Each measurement point is now varied by drawing a random value Re'_{LSC} and Ra' from their respective distribution. Fitting a power law to this new data using a least-squares fit gives new values for c' and γ'. Repeatedly fitting power laws to new randomly generated data Re'_{LSC} and Ra', gives sets of values for c' and γ'. The PDF of each set converges into a distinctive distribution, shown in figure C.2. For the exponent γ' (figure C.2(b)), the PDF is a Gaussian distribution. Since the amplitude c' has to always be positive, its PDF cannot be purely Gaussian. Instead, it converges towards an inverse Gaussian distribution [114] (figure C.2(a)). The new uncertainties of the power law amplitude and exponent are now computed as the standard deviation of these distributions with respect to the ODR fit results c and γ

$$\Delta c = \sqrt{\frac{\sum_{i=1}^{N}(c'_i - c)^2}{N}}, \qquad \Delta\gamma = \sqrt{\frac{\sum_{i=1}^{N}(\gamma'_i - \gamma)^2}{N}}. \qquad (C.2)$$

c'_i and γ'_i are the individual fit results from N realisations of Re'_{LSC} and Ra'. The standard deviations are normalised by N instead of the more commonly used $N-1$, since the mean values of the distributions are not calculated and instead the already known results from the ODR fits are used. For the present example of $Re_{LSC}(Ra)$, these standard deviations are calculated from 25 000 realisations of c' and γ' to be $\Delta c = 4.4$ and $\Delta\gamma = 0.03$. These values are one order of magnitude larger than the standard deviations provided by the ODR algorithm.

Figure C.3 re-plots the experimental data and the ODR fit from figure C.1. The dotted lines, however, now represent the new standard deviation $\Delta\gamma$ from (C.2). The new uncertainty of the exponent represents the data uncertainty much better than the ODR uncertainty.

The standard deviation Δc for the amplitude is very much dependent on how close the fit value c is to zero with respect to its variation due to the data uncertainty. As can be seen for the data $Re_{centre}(Ra)$ in figure 4.13, Δc can even exceed the value of c. This does not imply,

that c may become negative. Since the amplitude follows an inverse Gaussian distribution, this describes a PDF with a peak close to zero and with a long positive tail.

The standard deviations Δc and $\Delta\gamma$ are used as uncertainties for all power law fits in the present thesis. If different fit functions are used to model a set of data and the uncertainty of both the input variables and output quantity are available, the regular standard deviations provided by the ODR algorithm are used. If the uncertainty is unknown for either the input variable or the output quantity (or for both) a least-squares fit is applied and the standard deviation calculated by that algorithm is given as the fit parameter uncertainty.

Bibliography

List of Publications

Percentages of contribution: [Z1] – 85 %,   [Z2] – 80 %,   [Z3] – 75 %

[Z1] T. Zürner, W. Liu, D. Krasnov, and J. Schumacher, "Heat and momentum transfer for magnetoconvection in a vertical external magnetic field", Phys. Rev. E **94**, 043108 (2016).

[Z2] T. Zürner, T. Vogt, C. Resagk, S. Eckert, and J. Schumacher, "Local Lorentz force and ultrasound Doppler velocimetry in a vertical convection liquid metal flow", Exp. Fluids **59**, 3 (2018).

[Z3] T. Zürner, F. Schindler, T. Vogt, S. Eckert, and J. Schumacher, "Combined measurement of velocity and temperature in liquid metal convection", J. Fluid Mech. **876**, 1108–1128 (2019).

References

[1] P. K. Kundu, I. M. Cohen, and D. R. Dowling, *Fluid Mechanics*, 6th ed. (Academic Press, Waltham, MA, 2015).

[2] H. Bénard, "Étude expérimentale du mouvement des liquides propageant la chaleur par convection. Régime permanent: tourbillons cellulaires", C. R. Hebd. Séances Acad. Sci. **130**, 1004–1007 (1900).

[3] S. Fauve, "Henri Bénard and pattern-forming instabilities", C. R. Phys. **18**, 531–543 (2017).

[4] J. W. S. Lord Rayleigh, "On convection currents in a horizontal layer of fluid, when the higher temperature is on the under side", Philos. Mag. **32**, 529–546 (1916).

[5] S. Chandrasekhar, *Hydrodynamic and Hydromagnetic Stability*, 3rd ed. (Dover Publications, Inc., New York, 1961).

[6] H. Jeffreys, "The stability of a layer of fluid heated below", Philos. Mag. **2**, 833–844 (1926).

[7] A. Pellew and R. V. Southwell, "On maintained convective motion in a fluid heated from below", Proc. R. Soc. London, Ser. A **176**, 312–343 (1940).

[8] I. Catton and D. K. Edwards, "Effect of side walls on natural convection between horizontal plates heated from below", J. Heat Transfer **89**, 295–299 (1967).

[9] S. H. Davis, "Convection in a box: linear theory", J. Fluid Mech. **30**, 465–478 (1967).

Bibliography

[10] G. S. Charlson and R. L. Sani, "Thermoconvective instability in a bounded cylindrical fluid layer", Int. J. Heat Mass Transf. **13**, 1479–1496 (1970).

[11] F. H. Busse, "Non-linear properties of thermal convection", Rep. Prog. Phys. **41**, 1929–1967 (1978).

[12] F. H. Busse and R. M. Clever, "Instabilities of convection rolls in a fluid of moderate Prandtl number", J. Fluid Mech. **91**, 319–335 (1979).

[13] G. Ahlers, S. Grossmann, and D. Lohse, "Heat transfer and large scale dynamics in turbulent Rayleigh-Bénard convection", Rev. Mod. Phys. **81**, 503–537 (2009).

[14] F. Chillà and J. Schumacher, "New perspectives in turbulent Rayleigh-Bénard convection", Eur. Phys. J. E **35**, 58 (2012).

[15] A. Pandey, J. D. Scheel, and J. Schumacher, "Turbulent superstructures in Rayleigh-Bénard convection", Nat. Commun. **9**, 2118 (2018).

[16] R. J. A. M. Stevens, A. Blass, X. Zhu, R. Verzicco, and D. Lohse, "Turbulent thermal superstructures in Rayleigh-Bénard convection", Phys. Rev. Fluids **3**, 041501 (2018).

[17] E. Fonda, A. Pandey, J. Schumacher, and K. R. Sreenivasan, "Deep learning in turbulent convection networks", Proc. Natl. Acad. Sci. USA, 201900358 (2019).

[18] J. D. Scheel and J. Schumacher, "Global and local statistics in turbulent convection at low Prandtl numbers", J. Fluid Mech. **802**, 147–173 (2016).

[19] H. T. Rossby, "A study of Bénard convection with and without rotation", J. Fluid Mech. **36**, 309–335 (1969).

[20] W. v. R. Malkus, "The heat transport and spectrum of thermal turbulence", Proc. R. Soc. Lond. A **225**, 196–212 (1954).

[21] B. I. Shraiman and E. D. Siggia, "Heat transport in high-Rayleigh-number convection", Phys. Rev. A **42**, 3650–3653 (1990).

[22] R. H. Kraichnan, "Turbulent thermal convection at arbitrary Prandtl number", Phys. Fluids **5**, 1374–1389 (1962).

[23] F. H. Busse and R. M. Clever, "An asymptotic model of two-dimensional convection in the limit of low Prandtl number", J. Fluid Mech. **102**, 75–83 (1981).

[24] S. Grossmann and D. Lohse, "Scaling in thermal convection: a unifying theory", J. Fluid Mech. **407**, 27–56 (2000).

[25] S. Grossmann and D. Lohse, "Thermal convection for large Prandtl numbers", Phys. Rev. Lett. **86**, 3316–3319 (2001).

[26] R. J. A. M. Stevens, E. P. van der Poel, S. Grossmann, and D. Lohse, "The unifying theory of scaling in thermal convection: the updated prefactors", J. Fluid Mech. **730**, 295–308 (2013).

[27] S. Grossmann and D. Lohse, "Prandtl and Rayleigh number dependence of the Reynolds number in turbulent thermal convection", Phys. Rev. E **66**, 016305 (2002).

[28] E. D. Siggia, "High Rayleigh number convection", Annu. Rev. Fluid Mech. **26**, 137–168 (1994).

[29] S. Grossmann and D. Lohse, "Thermal convection in small Prandtl number liquids: strong but ineffective", AIP Conf. Proc. **1076**, 68–75 (2008).

[30] L. D. Landau and E. M. Lifshitz, *Fluid Mechanics*, 3rd ed., Vol. 6, Course of Theoretical Physics (Pergamon Press, Oxford, 1966).

[31] P. A. Davidson, *An Introduction to Magnetohydrodynamics*, 1st ed., Vol. 25, Cambridge Texts in Applied Mathematics (Cambridge University Press, Cambridge, United Kingdom, 2001).

[32] R. Moreau, *Magnetohydrodynamics*, Vol. 3, Fluid Mechanics and Its Applications (Kluwer Academic Publishers, Dordrecht, 1990).

[33] W. Thompson, "Thermal convection in a magnetic field", Philos. Mag. **42**, 1417–1432 (1951).

[34] S. Chandrasekhar, "On the inhibition of convection by a magnetic field", Philos. Mag. **43**, 501–532 (1952).

[35] S. Chandrasekhar, "On the inhibition of convection by a magnetic field: II", Philos. Mag. **45**, 1177–1191 (1954).

[36] R. J. Adrian and J. Westerweel, *Particle Image Velocimetry*, Cambridge Aerospace Series (Cambridge University Press, 2011).

[37] H.-E. Albrecht, N. Damaschke, M. Borys, and C. Tropea, *Laser Doppler and Phase Doppler Measurement Techniques*, Experimental Fluid Mechanics (Springer-Verlag, Berlin Heidelberg, 2003).

[38] F. Toschi and E. Bodenschatz, "Lagrangian properties of particles in turbulence", Annu. Rev. Fluid Mech. **41**, 375–404 (2009).

[39] S. Eckert, A. Cramer, and G. Gerbeth, "Velocity measurement techniques for liquid metal flows", in *Magnetohydrodynamics*, Vol. 80, Fluid Mechanics And Its Applications (Springer, Dordrecht, 2007), pp. 275–294.

[40] P. H. Dauby, "Continuous casting: make better steel and more of it!", Rev. Metall. **109**, 113–136 (2012).

[41] N. Shevchenko, S. Boden, S. Eckert, D. Borin, M. Heinze, and S. Odenbach, "Application of X-ray radioscopic methods for characterization of two-phase phenomena and solidification processes in metallic melts", Eur. Phys. J. Spec. Top. **220**, 63–77 (2013).

[42] M. Ščepanskis, M. Sarma, P. Vontobel, P. Trtik, K. Thomsen, A. Jakovičs, and T. Beinerts, "Assessment of electromagnetic stirrer agitated liquid metal flows by dynamic neutron radiography", Metall. Mater. Trans. B **48**, 1045–1054 (2017).

[43] G. Morgenschweis, *Hydrometrie: Theorie und Praxis der Durchflussmessung in offenen Gerinnen*, 2nd ed., VDI-Buch (Springer Vieweg, Berlin, 2018).

[44] R. Ricou and C. N. Vivès, "Local velocity and mass transfer measurements in molten metals using an incorporated magnet probe", Int. J. Heat Mass Transf. **25**, 1579–1588 (1982).

[45] N. T. Baker, A. Pothérat, L. Davoust, F. Debray, and R. Klein, "Controlling the dimensionality of low-Rm MHD turbulence experimentally", Exp. Fluids **58** (2017).

[46] N. Krauter and F. Stefani, "Immersed transient eddy current flow metering: a calibration-free velocity measurement technique for liquid metals", Meas. Sci. Technol. **28**, 105301 (2017).

[47] M. Ratajczak, T. Gundrum, F. Stefani, and T. Wondrak, "Contactless inductive flow tomography: Brief history and recent developments in its application to continuous casting", J. Sens. **2014** (2014).

[48] A. Thess, E. V. Votyakov, and Y. Kolesnikov, "Lorentz force velocimetry", Phys. Rev. Lett. **96**, 164501 (2006).

[49] A. Thess, E. V. Votyakov, B. Knaepen, and O. Zikanov, "Theory of the Lorentz force flowmeter", New J. Phys. **9**, 299 (2007).

[50] J. A. Shercliff, *The Theory of Electromagnetic Flow-Measurement* (Cambridge University Press, Cambridge, 1962).

[51] J. Priede, D. Buchenau, and G. Gerbeth, "Single-magnet rotary flowmeter for liquid metals", J. Appl. Phys. **110**, 034512 (2011).

[52] J. Schleichert, I. Rahneberg, and T. Fröhlich, "Calibration of a novel six-degree-of-freedom force/torque measurement system", Int. J. Mod. Phys. Conf. Ser. **24**, 1360017 (2013).

[53] Y. Kolesnikov, C. Karcher, and A. Thess, "Lorentz force flowmeter for liquid aluminum: Laboratory experiments and plant tests", Metall. Mater. Trans. B **42**, 441–450 (2011).

[54] X. D. Wang, R. Klein, Y. Kolesnikov, and A. Thess, "Application of Lorentz force velocimetry to open channel flow", Mater. Sci. Forum **690**, 99–102 (2011).

[55] S. Vasilyan and T. Fröhlich, "Direct Lorentz force compensation flowmeter for electrolytes", Appl. Phys. Lett. **105**, 223510 (2014).

[56] S. Vasilyan, R. Ebert, M. Weidner, M. Rivero, B. Halbedel, C. Resagk, and T. Fröhlich, "Towards metering tap water by Lorentz force velocimetry", Meas. Sci. Technol. **26**, 115302 (2015).

[57] R. P. Uhlig, M. Zec, M. Ziolkowski, H. Brauer, and A. Thess, "Lorentz force sigmometry: A contactless method for electrical conductivity measurements", J. Appl. Phys. **111**, 094914 (2012).

[58] A. Viré, B. Knaepen, and A. Thess, "Lorentz force velocimetry based on time-of-flight measurements", Phys. Fluids **22**, 125101 (2010).

[59] N. Dubovikova, C. Resagk, C. Karcher, and Y. Kolesnikov, "Contactless flow measurement in liquid metal using electromagnetic time-of-flight method", Meas. Sci. Technol. **27**, 055102 (2016).

[60] C. Heinicke, S. Tympel, G. Pulugundla, I. Rahneberg, T. Boeck, and A. Thess, "Interaction of a small permanent magnet with a liquid metal duct flow", J. Appl. Phys. **112**, 124914 (2012).

[61] C. Heinicke and T. Wondrak, "Spatial and temporal resolution of a local Lorentz force flowmeter", Meas. Sci. Technol. **25**, 055302 (2014).

[62] D. Hernández, J. Schleichert, C. Karcher, T. Fröhlich, T. Wondrak, and K. Timmel, "Local Lorentz force flowmeter at a continuous caster model using a new generation multicomponent force and torque sensor", Meas. Sci. Technol. **27**, 065302 (2016).

[63] I. Sokolov, V. I. Noskov, A. M. Pavlinov, and Y. Kolesnikov, "Lorentz force velocimetry for high speed liquid sodium flow", Magnetohydrodynamics **52**, 481–493 (2016).

[64] Y. Takeda, "Velocity profile measurement by ultrasound Doppler shift method", Int. J. Heat Fluid Fl. **7**, 313–318 (1986).

[65] Y. Takeda, "Measurement of velocity profile of mercury flow by ultrasound Doppler shift method", Nucl. Technol. **79**, 120–124 (1987).

[66] Y. Plevachuk, V. Sklyarchuk, S. Eckert, G. Gerbeth, and R. Novakovic, "Thermophysical properties of the liquid Ga–In–Sn eutectic alloy", J. Chem. Eng. Data **59**, 757–763 (2014).

[67] U. Müller and L. Bühler, *Magnetofluiddynamics in Channels and Containers* (Springer Verlag, Berlin, 2001).

[68] C. Heinicke, "Local Lorentz force velocimetry for liquid metal duct flows", PhD thesis (Technischen Universität Ilmenau, Ilmenau, 2013).

[69] I. Sokolov, "Lorentz force velocimetry at high magnetic reynolds numbers", PhD thesis (Technischen Universität Ilmenau, Ilmenau, 2016).

[70] S. Chakraborty, "On scaling laws in turbulent magnetohydrodynamic Rayleigh-Benard convection", Physica D **237**, 3233–3236 (2008).

[71] S. Cioni, S. Chaumat, and J. Sommeria, "Effect of a vertical magnetic field on turbulent Rayleigh-Bénard convection", Phys. Rev. E **62**, R4520–R4523 (2000).

[72] J. M. Aurnou and P. L. Olson, "Experiments on Rayleigh–Bénard convection, magnetoconvection and rotating magnetoconvection in liquid gallium", J. Fluid Mech. **430**, 283–307 (2001).

[73] U. Burr and U. Müller, "Rayleigh–Bénard convection in liquid metal layers under the influence of a vertical magnetic field", Phys. Fluids **13**, 3247 (2001).

[74] E. M. King and J. M. Aurnou, "Magnetostrophic balance as the optimal state for turbulent magnetoconvection", Proc. Natl. Acad. Sci. USA **112**, 990–994 (2015).

[75] W. Liu, D. Krasnov, and J. Schumacher, "Wall modes in magnetoconvection at high Hartmann numbers", J. Fluid Mech. **849**, R2 (2018).

[76] M. Yan, M. A. Calkins, S. Maffei, K. Julien, S. M. Tobias, and P. Marti, "Heat transfer and flow regimes in quasi-static magnetoconvection with a vertical magnetic field", J. Fluid Mech. **877**, 1186–1206 (2019).

[77] Z. L. Lim, K. L. Chong, G.-Y. Ding, and K.-Q. Xia, "Quasistatic magnetoconvection: heat transport enhancement and boundary layer crossing", J. Fluid Mech. **870**, 519–542 (2019).

[78] T. Vogt, S. Horn, A. M. Grannan, and J. M. Aurnou, "Jump rope vortex in liquid metal convection", Proc. Natl. Acad. Sci. USA **115**, 12674–12679 (2018).

[79] Y. A. Çengel, *Introduction to Thermodynamics and Heat Transfer*, 2nd ed. (McGraw-Hill Primis, 2008).

[80] X.-L. Qiu, X.-D. Shang, P. Tong, and K.-Q. Xia, "Velocity oscillations in turbulent Rayleigh–Bénard convection", Phys. Fluids **16**, 412–423 (2004).

[81] C. Sun, K.-Q. Xia, and P. Tong, "Three-dimensional flow structures and dynamics of turbulent thermal convection in a cylindrical cell", Phys. Rev. E **72**, 026302 (2005).

[82] E. Brown and G. Ahlers, "Rotations and cessations of the large-scale circulation in turbulent Rayleigh–Bénard convection", J. Fluid Mech. **568**, 351–386 (2006).

[83] H.-D. Xi and K.-Q. Xia, "Cessations and reversals of the large-scale circulation in turbulent thermal convection", Phys. Rev. E **75**, 066307 (2007).

[84] E. Brown and G. Ahlers, "The origin of oscillations of the large-scale circulation of turbulent Rayleigh–Bénard convection", J. Fluid Mech. **638**, 383–400 (2009).

[85] H.-D. Xi, S.-Q. Zhou, Q. Zhou, T.-S. Chan, and K.-Q. Xia, "Origin of the temperature oscillation in turbulent thermal convection", Phys. Rev. Lett. **102**, 044503 (2009).

[86] D. Funfschilling and G. Ahlers, "Plume motion and large-scale circulation in a cylindrical Rayleigh-Bénard cell", Phys. Rev. Lett. **92**, 194502 (2004).

[87] Y. Tsuji, T. Mizuno, T. Mashiko, and M. Sano, "Mean wind in convective turbulence of mercury", Phys. Rev. Lett. **94**, 034501 (2005).

[88] Q. Zhou, H.-D. Xi, S.-Q. Zhou, C. Sun, and K.-Q. Xia, "Oscillations of the large-scale circulation in turbulent Rayleigh–Bénard convection: the sloshing mode and its relationship with the torsional mode", J. Fluid Mech. **630**, 367–390 (2009).

[89] R. Khalilov, I. Kolesnichenko, A. Pavlinov, A. Mamykin, A. Shestakov, and P. Frick, "Thermal convection of liquid sodium in inclined cylinders", Phys. Rev. Fluids **3**, 043503 (2018).

[90] R. J. A. M. Stevens, H. J. H. Clercx, and D. Lohse, "Effect of plumes on measuring the large scale circulation in turbulent Rayleigh-Bénard convection", Phys. Fluids **23**, 095110 (2011).

[91] Y.-C. Xie, P. Wei, and K.-Q. Xia, "Dynamics of the large-scale circulation in high-Prandtl-number turbulent thermal convection", J. Fluid Mech. **717**, 322–346 (2013).

[92] J. Schumacher, V. Bandaru, A. Pandey, and J. D. Scheel, "Transitional boundary layers in low-Prandtl-number convection", Phys. Rev. Fluids **1**, 084402 (2016).

[93] X.-L. Qiu and P. Tong, "Onset of coherent oscillations in turbulent Rayleigh-Bénard convection", Phys. Rev. Lett. **87**, 094501 (2001).

[94]   S. Cioni, S. Ciliberto, and J. Sommeria, "Temperature structure functions in turbulent convection at low Prandtl number", Europhys. Lett. **32**, 413–418 (1995).

[95]   M. Breuer, S. Wessling, J. Schmalzl, and U. Hansen, "Effect of inertia in Rayleigh-Bénard convection", Phys. Rev. E **69**, 026302 (2004).

[96]   J. Schumacher, P. Götzfried, and J. D. Scheel, "Enhanced enstrophy generation for turbulent convection in low-Prandtl-number fluids", Proc. Natl. Acad. Sci. USA **112**, 9530–9535 (2015).

[97]   S. Cioni, S. Ciliberto, and J. Sommeria, "Strongly turbulent Rayleigh–Bénard convection in mercury: comparison with results at moderate Prandtl number", J. Fluid Mech. **335**, 111–140 (1997).

[98]   J. D. Scheel and J. Schumacher, "Predicting transition ranges to fully turbulent viscous boundary layers in low Prandtl number convection flows", Phys. Rev. Fluids **2**, 123501 (2017).

[99]   E. M. King and J. M. Aurnou, "Turbulent convection in liquid metal with and without rotation", Proc. Natl. Acad. Sci. USA **110**, 6688–6693 (2013).

[100] T. Takeshita, T. Segawa, J. A. Glazier, and M. Sano, "Thermal turbulence in mercury", Phys. Rev. Lett. **76**, 1465 (1996).

[101] J. A. Glazier, T. Segawa, A. Naert, and M. Sano, "Evidence against 'ultrahard' thermal turbulence at very high Rayleigh numbers", Nature **398**, 307–310 (1999).

[102] V. Kek and U. Müller, "Low Prandtl number convection in layers heated from below", Int. J. Heat Mass Transf. **36**, 2795–2804 (1993).

[103] J. Pal, A. Cramer, T. Gundrum, and G. Gerbeth, "MULTIMAG–A MULTIpurpose MAGnetic system for physical modelling in magnetohydrodynamics", Flow Meas. Instrum. **20**, 241–251 (2009).

[104] R. Touihri, H. Ben Hadid, and D. Henry, "On the onset of convective instabilities in cylindrical cavities heated from below. I. Pure thermal case", Phys. Fluids **11**, 2078–2088 (1999).

[105] B. C. Houchens, L. M. Witkowski, and J. S. Walker, "Rayleigh–Bénard instability in a vertical cylinder with a vertical magnetic field", J. Fluid Mech. **469**, 189–207 (2002).

[106] J. A. Shercliff, "Steady motion of conducting fluids in pipes under transverse magnetic fields", Math. Proc. Cambridge Philos. Soc. **49**, 136–144 (1953).

[107] F. Zhong, R. Ecke, and V. Steinberg, "Asymmetric modes and the transition to vortex structures in rotating Rayleigh-Bénard convection", Phys. Rev. Lett. **67**, 2473–2476 (1991).

[108] K. L. Chong, Y. Yang, S.-D. Huang, J.-Q. Zhong, R. J. A. M. Stevens, R. Verzicco, D. Lohse, and K.-Q. Xia, "Confined Rayleigh-Bénard, rotating Rayleigh-Bénard, and double diffusive convection: A unifying view on turbulent transport enhancement through coherent structure manipulation", Phys. Rev. Lett. **119**, 064501 (2017).

Bibliography

[109]   I. N. Bronstein, K. A. Semendjajew, G. Musiol, and H. Mühlig, *Taschenbuch der Mathematik*, 8th ed. (Verlag Harri Deutsch, Frankfurt am Main, 2012).

[110]   F. Stefani and G. Gerbeth, "Velocity reconstruction in conducting fluids from magnetic field and electric potential measurements", Inverse Probl. **15**, 771 (1999).

[111]   V. S. Vladimirov, *Equations of Mathematical Physics* (Marcel Dekker, Inc., New York, 1971).

[112]   E. P. Furlani, *Permanent Magnet and Electromechanical Devices: Materials, Analysis, and Applications*, Electromagnetism (Academic Press, Inc., San Diego, 2001).

[113]   P. T. Boggs and J. E. Rogers, "Orthogonal distance regression", in *Statistical Analysis of Measurement Error Models and Applications*, Vol. 112, Contemporary Mathematics (American Mathematical Society, Providence, Rhode Island, 1990), pp. 183–194.

[114]   J. L. Folks and R. S. Chhikara, "The inverse Gaussian distribution and its statistical application–A review", J. R. Statist. Soc. B **40**, 263–289 (1978).

Acknowledgements